UNIVERSITY OF SOUTHAMPTON

Faculty of Engineering, Science and Mathematics
Zepler Institute For Photonics and Nanoelectronics

MIR Photodetection Using Intrinsic Monolithic Integrated Germanium Photodiodes

DOI: 10.5258/SOTON/D2430

by

Lauren Reid
MPhys (Hons)
ORCiD: 0000-0002-1599-6862

A thesis for the degree of
Doctor of Philosophy

December 2022

University of Southampton

Abstract

Faculty of Engineering, Science and Mathematics
Zepler Institute For Photonics and Nanoelectronics

Doctor of Philosophy

MIR Photodetection Using Intrinsic Monolithic Integrated Germanium Photodiodes

by Lauren Reid

Silicon (Si) photonics as a field is about photonic integrated circuits (PIC) using group IV materials as a substrate, mainly Si. Creating PICs from Si allows circuitry to be small and inexpensive; enabled by the use of mature fabrication techniques, existing recipes and foundries. The small size of PICs is useful for applications such as free-space telecommunication and chemical sensing where many devices are needed or are made as consumables. An infrared photodetector that is responsive in the 3-4 μm is needed to create PICs for these applications (1). To keep the cost low, a detector should be monolithically grown or deposited on Si. Si defect mediated detectors have been shown to be responsive, up to wavelengths of 2.5 μm (2), and able to operate at high speeds (up to 35 GHz) (3), but have not yet demonstrated a spectral response in the 3-4 μm region. Defect mediated germanium (Ge) detectors are potential candidates for detecting 3-4 μm light. Ge can be epitaxially grown on Si and using it for defect mediated absorption currently is relatively unexplored.

In this thesis, Ge PIN photodiodes were created and implanted with boron ions to create defects within a rib waveguide. The responsivity versus the length of the photodiode implanted with defeccts was investigated, at fluences of $1x10^{10}$, $1x10^{12}$ and $1x10^{14}$ ions/cm^2, using no reverse bias. These measurements showed that the boron implantation had a negative effect on the responsivity, although, the unimplanted detectors had an unexpectedly high responsivity of approximately 0.1 A/W. This prompted investigation into the responsivity with an increasing reverse bias using 2 μm and 3.8 μm light, which resulted in a maximum responsivity of 1.04 A/W at -10 V using 2 μm light and 0.1 A/W at -7 V using 3.8 μm light at room temperature. A 12.5 Gb/s pseudorandom pattern was used to modulate 2 μm light, the detection of this light resulted in an open eye diagram. Measurements were performed to find the photodetection method, the linearity of the devices suggested that there was no two photon absorption, there was minimal difference in transmission between waveguides and photodiodes suggesting that photoactive defects were not created in the PIN junction formation. Finally, Raman spectroscopy was performed and found a 0.22 % strain which may be responsible for most of the absorption at 2 μm. The absorption at 3.8 μm may be caused from threading dislocations at the Ge Si boundary as similar wafers showed a high density of defects at the boundary. These

results show Ge-on-SOI as a practical detection material in an extended wavelength range. More research is needed to understand the source of infrared absorption.

Contents

List of Figures

List of Tables

Declaration of Authorship

I declare that this thesis and the work presented in it is my own and has been generated by me as the result of my own original research.

I confirm that:

1. This work was done wholly or mainly while in candidature for a research degree at this University;
2. Where any part of this thesis has previously been submitted for a degree or any other qualification at this University or any other institution, this has been clearly stated;
3. Where I have consulted the published work of others, this is always clearly attributed;
4. Where I have quoted from the work of others, the source is always given. With the exception of such quotations, this thesis is entirely my own work;
5. I have acknowledged all main sources of help;
6. Where the thesis is based on work done by myself jointly with others, I have made clear exactly what was done by others and what I have contributed myself;
7. None of this work has been published before submission

Signed:..... Date:.....

Acknowledgements

I would like to thank Dr Miloš Nedeljković, Professor Radan Slavík and Professor Goran Mashanovich who I have worked most closely with, they have all provided unconditional help and support. Goran, you have consistently been supportive of letting us learn in a way that suits us. Radan, you have been a fantastic, knowledgeable teacher, I appreciate you for giving me so much of your time. Miloš, you have always answered any questions quickly and helped guide my PhD, I am also grateful for how much time you have given me.

I would like to thank Dr Li Ke, Dr Weiwei Zhang and Professor Dave Thompson. They are all incredibly smart and helpful people who all never told me that they were tired of me asking questions about how to measure my photodiodes at high speeds. I'm still sorry for breaking your probes Dave. I would also like to thank Stephan Ilie and Dr Callum Stirling for so generously performing tests and fabrication processes for me.

Thank you to members of the Silicon Photonics Group, Coherent Optical Signals Group and ORC who helped with all aspects of my PhD, technical and administrative work, and most importantly as friends; Meng Ding, Bo Shi, Xuhao Wei, Zitong Feng, Dr Dave Rowe, Dr Lorenzo Mastronardi, Dr Milan Milošević, Dr Ahmed Osman, Dr Yanli Qi, Paula Smith, Bharat Pant, Dr Kasia Grabska, Dr Wei Cao, Dr Jordi Soler Penadés and Dr Andrei Donko

I would like to separately thank those who supported me when I struggled emotionally through my PhD. Thank you Radan for being so understanding. You supported me beyond research and on a personal level, even. Your ability to incorporate my hardships into your supervision of me is a shining example of how to support those struggling with their mental health. Dr Maggie Agnew, you were empathetic and helpful. Thank you for listening and sacrificing your evenings to help improve the grammar and readability of my thesis. Thank you Dr Jonathan Leach, who is not my supervisor anymore but continued to serve as a mentor in academia. Thank you to my friends for their support; Dr Katrina Morgan, Grant McDonald, Jamie Rose, Neasa NiBhrian, Connor Denton, Amy Phillips and Alejandro Pinto.

Finally, thank you to my family, their support allowed me to get to a PhD level. My Dad, who helped nurture a real love of science. My Mum and Nicholas Pickerill who kept me humble, saying despite my doing research don't have common sense.

Chapter 1

Introduction

1.1 Motivation

1.1.1 Silicon Photonics

All facets of our lives are becoming increasingly reliant on creating more computing power in order to drive the internet of things, produce higher quality movies, and design more complex video games. To increase available computing power, we look to computer chips. Within a computer chip there are billions of transistors made from silicon, which are electrical switches responsible for performing calculations. Moore's law predicted that the density of transistors would increase every two years, although with transistor sizes reaching 3 nm in size, there is not room to keep shrinking them when the size of a silicon atom is 0.2 nm.

As the density of transistors increases, the interconnects that allow communication across the chip also become more dense and compact. The shrinking of interconnects introduces parasitic capacitance that increases the delay of communication across the chip. Eventually this delay becomes comparable to the computing speed of the transistors and the interconnects become the limiting factor in processing speed. This problem is known as the interconnect bottleneck. Silicon photonics as a field aims to solve this by introducing nanoscale, integrated photonic circuitry as interconnects, using light rather than electricity as a medium for information as it avoids the problem of parasitic capacitance (4).

Photonic circuits are made up of waveguides, light sources, modulators and photodetectors which are analogous to electronic wires, batteries, transistors and ammeters. An example of a photonic circuit is shown below in Figure 1.1.

Silicon photonics is an especially powerful and efficient solution to the bottleneck problem, because as the name suggests, it can be created on the same platform (i.e., silicon) as the electrical circuitry, as well as using the same fabrication techniques. By making use of

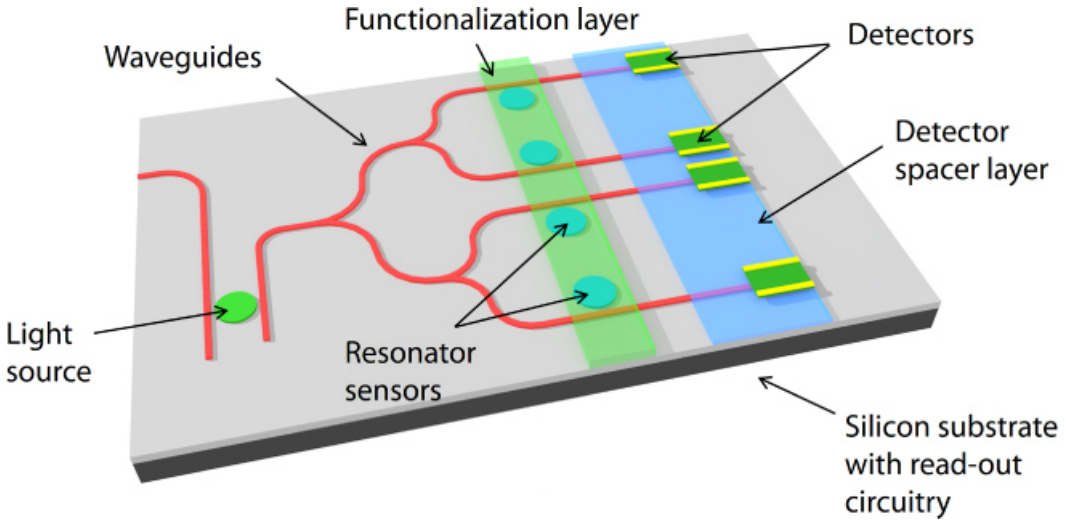

FIGURE 1.1: Illustration of a sensing circuit. The image shows how a series of components like waveguides, light sources and detectors can be put together to create a functional circuit (5).

foundries and mature techniques already used for fabrication of integrated electronic circuits, inexpensive photonic integrated circuits (PICs) can be realised.

By creating PICs, the properties of light can be capitalised on for other applications to provide cheaper, smaller solutions. Currently silicon photonics has a wealth of devices and components that are optimised to operate at the telecommunication wavelength bands between 1310 - 1550 nm, where successful interconnects have already been commercialised (6). However, by extending the wavelength that the components can operate in further into the infrared, new innovations can be applied to applications that could only be uniquely solved by silicon photonics, like LIDAR, environmental/health/security sensing, freespace telecommunication and more.

1.1.2 Sensing

While in the 1550 nm region PICs can be used to help increase the speed of information transfer the Mid-Infrared (MIR) wavelength region, quoted here as 2 - 16 μm, can be used to identify molecules. As chemical compounds have absorption spectra that are unique and identifiable within this region, see Figure 1.2. The process of this spectroscopy is known as sensing.

In response to the concern of global warming, gas detection and monitoring is needed and in volume. By creating MIR circuits on chip, chemical sensing can be performed through absorption spectroscopy. Creating sensing circuits on a silicon platform hopes to provide fast, real time detection that is inexpensive and of a small footprint, allowing for more monitoring to take place.

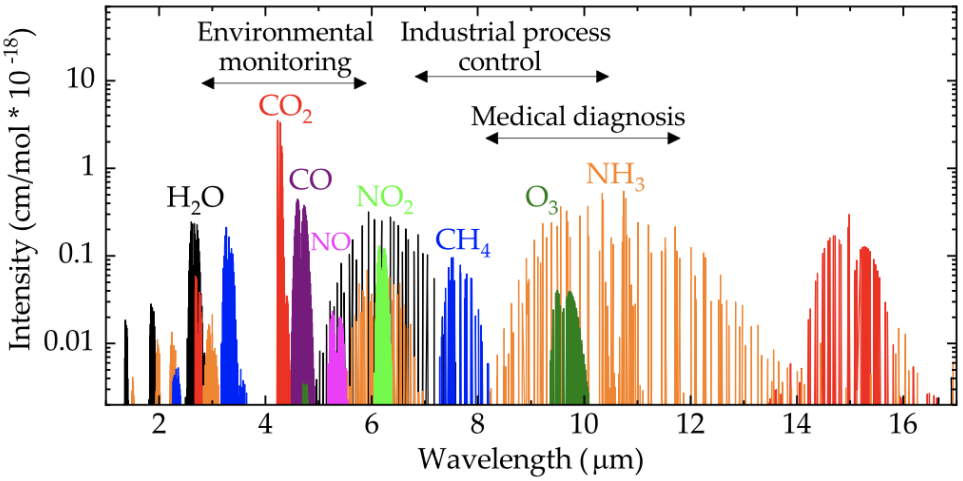

FIGURE 1.2: An example of absorption spectra across the MIR. The absorption peaks of some chemicals can be seen. (7).

Sensing circuits on chip require a MIR light source and can operate by splitting the light down two arms, one where the evanescent field of the light interacts with the chemical, gas, protein or molecule of interest on the top surface of the waveguide and one where it does not; the light at the end of each path is measured and compared to look for absorption at the peak corresponding to the chemical of interest. An example of a sensing circuit is shown in Figure 1.1.

1.1.3 Free-Space Telecommunication

With the increasing number of technology connected through the internet of things, higher quality video and games being downloaded on mobile devices, more wireless internet bandwidth is needed. Cisco calculates by 2023 that there will be 1.6 networked devices and connections per person globally, up from 1.2 in 2018 (8). Future wireless network upgrades will require light communications, ideally using all parts of the visible and invisible spectrum, as there are several trade offs when it comes to the choice of the light wavelength. For example, visible and Near-Infrared (NIR) communications are readily available, but do not operate in the eye safe region (limiting powers that could be used) and are sensitive to weather (fog, rain). The possibility of using MIR light for wireless communications is under investigation. MIR is a prime candidate for several factors: the earth's atmosphere has low attenuation in 3.8 μm, 5 μm and 10 μm MIR spectral regions, see Figure 1.3; MIR is eyesafe even at high powers; and it is not as weather sensitive as visible/NIR (9).

A large number of transmitters and receivers will be needed to implement MIR communications, as MIR light is easily blocked by trees and walls. Therefore, they need to be small and low-cost. This is where PICs can be a solution.

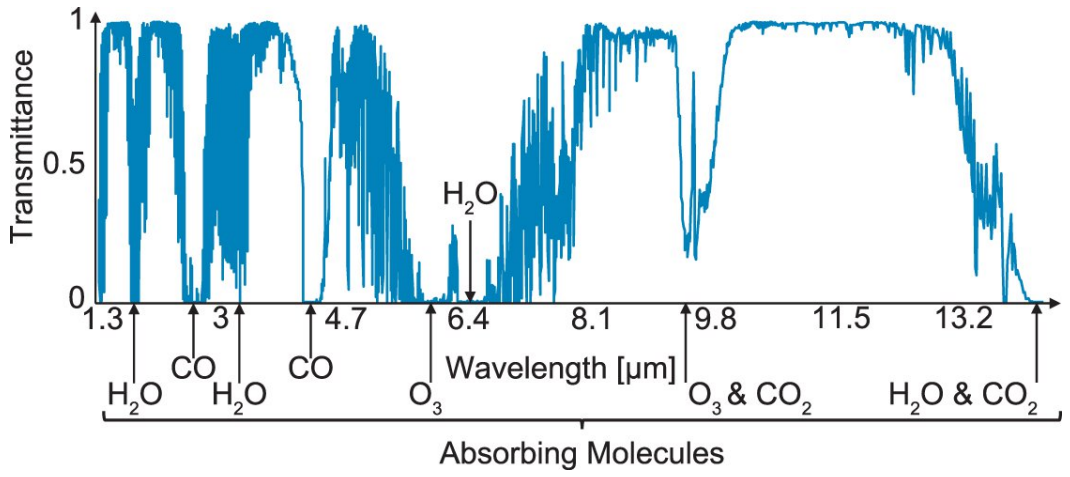

FIGURE 1.3: Diagram of the infrared atmospheric window. Showing areas of high transmission and chemicals responsible for regions of low transmission (10).

1.1.4 Solution

If a PIC device is to be a solution for both sensing and free-space telecommunication, a small, inexpensive form of MIR photodetection is needed. Integrated detection in the MIR is made on different material platforms depending on the needs of application because of the different strengths and weaknesses of each platform. Materials such as graphene and devices like bolometers are potentially useful for their broadband operation, although when using graphene the fabrication can be more difficult because of the need for manual exfoliation and the signal from bolometers is small and requires amplification. Materials such as III-V and black phosphorus can operate in the 3-4 μm region and have a high responsivity in the 0.1 A/W range but again require extra fabrication steps such as flip chip bonding (11) (12). Group IV materials such as Ge/Sn alloys and extrinsic silicon are monolithic but on waveguide integrated detectors the spectral range has not yet been shown to extend past 3 μm for either material.

The photodetectors created in this thesis are based on the design of extrinsic silicon detectors by using germanium instead to extend the absorption further into the MIR. This is preferable than working to improve the spectral response of Ge/Sn as an extended spectral range requires large Sn ratios which makes the growth of a quality Ge/Sn crystal difficult. This provides a solution in the development of future free-space telecommunication and chemical sensing by providing a CMOS compatible photodiode. A MIR germanium platform is practical because of its transparency up to 15 μm and has already been used in the creation of low loss waveguides up to 7 μm (13).

1.2 Thesis Structure

This thesis is comprised of 8 chapters. To explain the background knowledge to the thesis's project, defect mediated Ge detectors, chapter 2 will cover: the fundamental physics of PN junctions, how sub-band absorption differs from regular absorption of photons and the characteristics of detectors relevant to this thesis. Chapter 3 covers the fabrication techniques used to create the devices and gives short descriptions how each of the techniques and equipment work.

Chapter 4 is a literature review of integrated photodetection. It gives context of the field to the reader and also to show what guided the vision of the detectors created. In that photodiodes were created by looking for a platform that would allow CMOS compatible MIR absorption, and then designed to optimise responsivity and bandwidth. It is finished by giving a brief overview of the thesis objective and how it was chosen.

Chapter 5 details the simulations performed to find, the waveguide width, grating coupler etch depth, duty cycle and pitch and the parameters used for implanting ions. The final design for the detectors is described and the chip layout and mask design for fabrication is explained. It continues to Chapter 6 to cover the process of the fabricating all devices.

Chapter 6 presents the findings of characterising the detectors by responsivity and bandwidth at both 2 and 3.8 μm wavelength regions. It also describes in terms of key specifications of the equipment used, describing in details the setups used for characterisation and describing the passive and normalisation measurements performed.

Once all the experiments performed have been discussed, the thesis will conclude in chapter 7 with a summary of the results found, how the experiments could have been improved and explain plans for future work.

Chapter 2

Photodetectors

To preface the rest of the thesis, this chapter will provide a basic understanding of a semiconductor, explain how and why they are used to create PN/PIN photodiodes, describe the metrics used to grade a detector that are mentioned in this thesis including noise in detectors.

Photodetectors are devices that convert light into an electrical current. There are many types of photodetection absorbtion methods such as photoelectric, thermal and semiconductor. Throughout this thesis photodetectors will refer to photodiodes unless stated otherwise.

2.1 Operation of Photodiodes

2.1.1 Semiconductors

The ability of semiconductors to conduct is explained through a theory called "Band Theory of Semiconductors". The Pauli exclusion principle states that no two fermions can occupy identical quantum state within the same quantum system. Let us look at the semiconducting nature of silicon as an example, in Fig. 2.1.

In an individual silicon atom (Fig. 2.1(a)), energy levels are discrete, meaning they are separate and each level requires a certain energy to reach. As silicon atoms are brought together to form a bulk material (Fig. 2.1(b)), the electrons begin to overlap in space. As electrons are fermions, Pauli's principle must be satisfied here. Part of their quantum state is the energy of the electron. So that the electrons do not occupy the same energy level, the energy levels split causing a small shift. In a bulk material, splitting occurs many times due to the large amount of energy levels, this results in broad ranges of almost continuous energy levels (14).

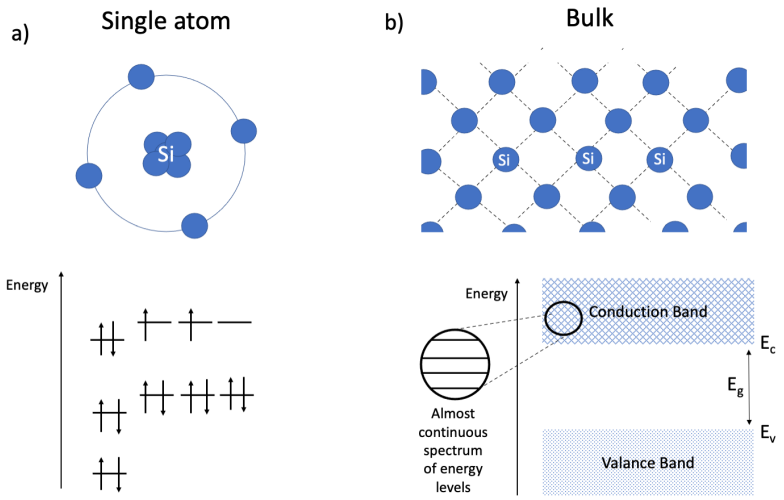

FIGURE 2.1: Diagram showing an example of the single atom and bulk material energy level structure.

In bulk silicon, electrons can occupy the valence band and conduction band. These bands are separated in energy, which is known as the bandgap. If energy is provided the electrons (i.e., energy from a photon), they have the possibility to be excited from the valence band into the conduction band. In the conduction band there are far fewer electrons and this allows them to flow freely. This is the how a current is created in a semiconductor.

2.1.2 Fermi-Dirac Distribution

The electrons promoted from valence to conduction band are fermions and are subject to the Pauli exclusion principle. This quantised restraint means electrons are dealt with statistically. Therefore when in a state of energy at a given temperature, they have a probability of being in a specified energy level. This probability is described by the fermi function which is an equation of the form,

$$f(E) = \frac{1}{e^{(E-E_F)/KT} + 1} \tag{2.1}$$

where f(E) is the probability of being in an energy state E at a given temperature T in kelvin, E_F is the Fermi level and K is the boltzmann constant (15).

The fermi level is the maximum energy that electrons can have at 0k. In both a semiconductor and insulator the fermi level lies within the bandgap, meaning all electrons occupy the valence band when temperature is at absolute zero. In a metal, there is no gap and the fermi level lies within an energy band, see Fig. 2.2.

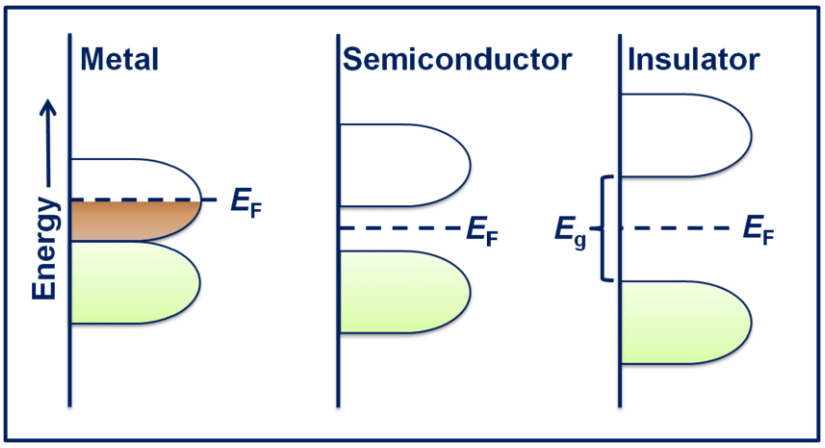

FIGURE 2.2: Shows where the fermi level lies in a metal, semiconductor and metal (16).

As the temperature of a system increases, the probability of electrons existing at higher energies increases and electrons can be promoted to the conduction band, see Fig. 2.3. This is the basis of thermal noise in a detector, discussed later in this chapter.

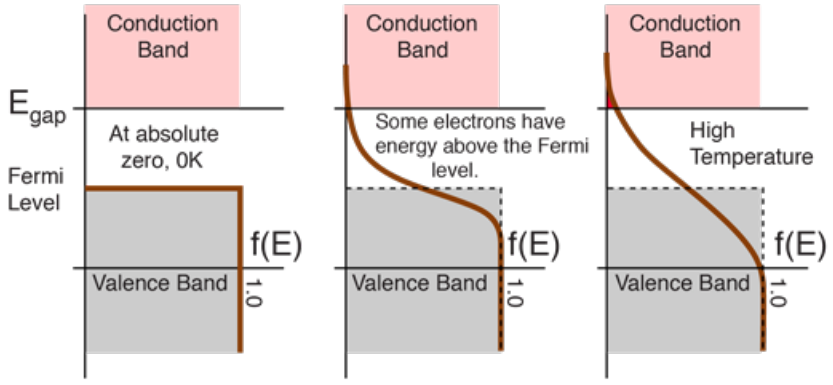

FIGURE 2.3: From left to right shows a semiconductor bandgap with an overlay plot of f(E) with increasing temperature (17).

2.1.3 PN Junctions

PN junctions are the basis of transistors, detectors and light sources. To create a PN junction, the semiconductor material of choice first requires doping. Doping is an established method involving the addition or removal of electrons to change the electrical properties of a semiconductor; this is usually accomplished by introducing foreign atoms, dopants, into the crystal lattice via ion implantation or diffusion.

In the example case of silicon, boron and phosphorus are common dopants. Phosphorus's outer most shell of electrons contains one more electron than silicon. So when introduced to a silicon crystal, phosphorus provides an extra electron. Region of semiconductors that have been doped with more electrons are called "N-type" and the atoms used to provide the extra electrons are called donors. While regions that have electrons removed are called

"P-type" and the atoms providing holes are called acceptors. The removal of electrons can also be seen as the introduction of a 'hole' which is treated similarly to an electron but with the opposite charge sign. The effect of doping is illustrated in Fig. 2.4.

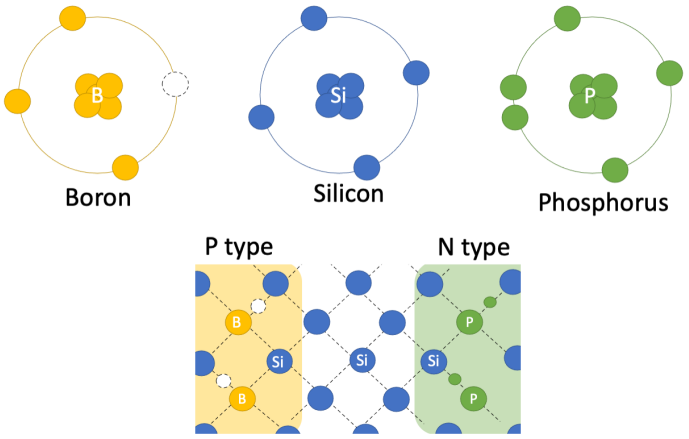

FIGURE 2.4: Diagram of a doped lattice of silicon, showing the addition of phosphorus would add electrons and the addition of boron would add 'holes'.

When the boundaries between P-type and N-type materials are brought together, they form a PN junction. When this happens, electrons from the N-type region will diffuse to recombine with the holes in the P-type region. The recombination of holes and electrons leaves behind positively and negatively charged ions in the N and P type regions respectively. The opposing charges of these ions create an electric field, which oppose the diffusion of any more carriers. The area containing these ions is called the depletion region (18).

2.1.4 PN Junctions and Light Detection

Detection of light occurs in a PN junction when a photon is incident upon the depletion region. If the energy of the photon is greater than the energy that separates the valence and conduction band, an electron can be excited from the valence to the conduction band. This action of electron excitation leaves a hole in the valence band; this is the creation of an electron-hole pair.

The photon energy E is given by equation (2.2) and is calculated using its wavelength λ, c the speed of light in vacuum and h Planck's constant.

$$E = \frac{hc}{\lambda} \tag{2.2}$$

The electron-hole pairs are then swept to either side of the junction due to the electric field within the depletion zone, and then drawn out to the external circuit. This process creates a detectable current that can be attributed to the absorption of light.

The bandgap of a semiconductor is responsible for limiting the wavelengths of light that can be absorbed. For example in silicon, wavelengths with an energy larger than the bandgap such as visible light can be detected while photons with a smaller energy than the bandgap, such as mid-infrared (MIR) light, cannot be detected because the energy transferred to the electrons is not enough to excite it beyond the bandgap.

An electrical bias can be applied to a PN junction to alter the difference in potential between the P and N type regions. To apply a reverse bias, the N-type region is connected to an anode (positive terminal) and the P-type region to a cathode (negative terminal) of a voltage source. When applied, carriers in the PN junction are further drawn to their respective terminals, increasing the width of the depletion zone and subsequently the electric field within. This increased electric field causes the electron-hole pairs to drift faster across the depletion zone; resulting in the detector operating faster. If the carrier's drift time is shorter than it is recombination time, it results in most of the carriers being collected and increasing the current created (19).

2.1.5 PIN and PN Junctions

A PIN junction is similar to a PN junction although the P and N doped regions are not in direct contact. Instead, they are separated by a small area of undoped/intrinsic material, which acts as the depletion region.

By adding an intrinsic region, the width of the depletion regions is increased, which increases the distance between the doped regions and thus lowers the capacitance between them. Which will increase the frequency response. This is explained in more detail in 2.3.3.1

A PIN junction that is integrated into waveguides has the benefits of allowing light to travel in the intrinsic region without overlapping with the doped regions, as light overlapping with doped regions can result in free carrier absorption. This absorption of light does not result in a photo generated current, reducing the quantum efficiency.

2.2 Defect-Mediated Principles

As an extension to the description of absorption of light in a PN junction, this section will describe the basic principles of defect-mediated absorption, a detection method referred to throughout this thesis.

The principle of defect-mediated absorption refers to the absorption of photons via levels within the bandgap of a semiconductor that are created by defects in the crystal lattice. Defects from a perfect crystal lattice are associated with an energy levels in the bandgap and different types of defects will have an associated levels (20). Defects can be classified in groups of point, line, planar and bulk defects; in this chapter we will look at point defects as they are most relevant to defect-mediated photodetectors.

A point defect can be classified as vacancy, interstitial, substitutional, or topological. A vacancy is a missing atom from the crystal. An interstitial is a defect where an atom (of any kind) occupies a space in the lattice not normally occupied. A substitutional atom is where a foreign atom will occupy the space of the atom within the crystal lattice. Finally a topological defect is one where the bonding between atoms is different from the rest of the lattice (i.e single bonds instead of double bonds). Each of the defects is visualised in Fig. 2.5.

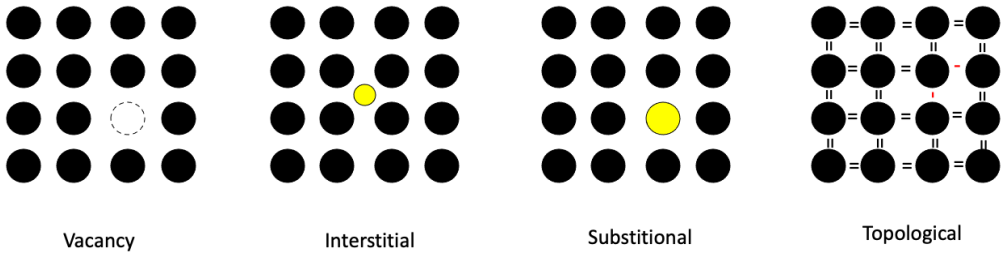

FIGURE 2.5: Illustration of types of point defects (21).

These defects that create levels within the bandgap are utilised by photodetectors to extend a material's spectral response to longer wavelengths of light. This can be seen by looking at the relationship between a photon's energy and it is wavelength as given by Eq. 2.2. The relationship between E and λ is inversely proportional, so when introducing levels via defects it allows photons of lower energy to be absorbed, in other words, a longer wavelength. The process is shown visually in Fig. 2.6. Electrons can be excited to the sub-band levels using a lower photon energy than the whole bandgap, then thermal energy will excite that electron into the conduction band (20).

2.3 Performance Metrics

This section covers the key characteristics that will be referred to throughout the thesis and when characterising manufactured detectors. As the literature discussed in this thesis is relevant to telecommunications and chemical sensing, the characteristics discussed revolve around the efficiency of detection, speed of signals and their relation to the noise. The chacteristics can be grouped into two categories: optical response (characterising the detector's response to light) and frequency response (characterising the detector's response to optical modulation). Each characteristic is listed below with a short description.

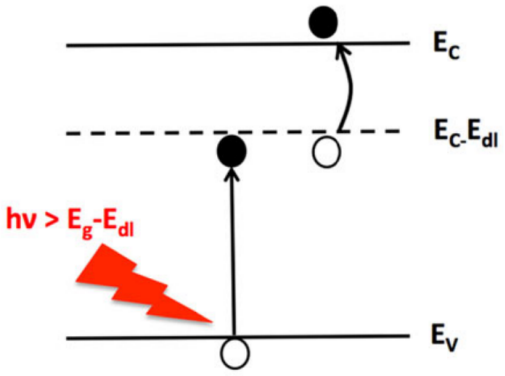

FIGURE 2.6: Diagram of defect mediated absorption. This example shows a photon exciting the electron to the sub-band level and it being thermally excited to the conduction band (20).

2.3.1 Sources of Noise

In a photodiode, the detection of light is identified by a measurable current signal. Additional current not formed by the absorption of light might interfere with how clearly a signal measurement can be made. Understanding the possible sources of noise makes it easier to avoid them. The sources of noise possible in a detector are listed below.

- Shot noise: An inherent noise limitation for all detectors. Shot noise is the noise caused by the Poisson distribution of a photons in a light signal. Photons will not arrive at the detector evenly spaced or timed but will average to a Poisson distribution.

$$I_{shot} = \sqrt{2eI_D\Delta\lambda}, \tag{2.3}$$

  where I_{shot} is the shot current, e is the charge of an electron, I_D is the average DC current and $\Delta\lambda$ is the bandwidth over which the noise is being calculated (22).

- Thermal noise (Johnson Noise): The electronic noise caused by the energy flucations of carriers, defined as

$$I_{th} = \sqrt{\frac{4K_BT\Delta\lambda}{R_L}}, \tag{2.4}$$

  where I_{th} is the thermal noise, K_B is Boltzmann constant, T is the temperature (Kelvin), R_L is the resistance of the load resistor and $\Delta\lambda$ is the bandwidth considered (22).

- Generation-Recombination (GR) noise: This form of noise is caused by the statistical fluctuations in the number of charge carriers.

- 1/f (flicker noise) - A source of noise that is inversely proportional to the frequency, therefore more significant at lower frequencies. It is not generally well understood. It shows up in other areas such as geography and astrophysics and still under discussion (23) (24).

2.3.2 Optical Response

The optical response refers to the detector's response to incident light. Several metrics come under this category, including responsivity, spectral range, noise equivalent power and dark current.

2.3.2.1 Noise Equivalent Power

Noise equivalent power (NEP) is a characteristic that describes the sensitivity of the detector with respect to noise. NEP is defined as the power of light required to create a signal-to-noise ratio of 1, over a 1 Hz bandwidth, i.e., how much power is needed to create a signal equal to the noise floor (all noise present before any signal is received). It is usually described in units of W/Hz. The smaller the NEP of a detector, the smaller the signal it can detect.

2.3.2.2 Dark Current

This is the current created from the detector in the absence of light. It is often created by the thermal generation of carriers from valence to conduction band via defects or impurities. Therefore higher temperatures and smaller bandgaps would increase the dark current of a detector. For example silicon inherently has less dark current than germanium at the same temperature. For MIR detectors this is where cooling becomes useful to reduce thermally generated noise.

2.3.2.3 Quantum Efficiency

The quantum efficiency (QE) is a measure of the efficiency of a photodetector and refers to the ratio of photons in a detector that are converted to useful electrons measured as a percentage. The quantum efficiency can refer to either the internal QE or the external QE.

External QE is defined as the number of photogenerated carriers that come from the device whereas internal QE refers to the percentage of incident photons on the diode that are converted to electron hole pairs. Internal QE is often larger than the external QE. Generated electron hole pairs can lost before being collected, some examples include

reflection at ohmnic contacts, photons being absorbed and being converted to phonons (25). If each photon created 1 electron hole pair and was measured as a single electron leaving the device that would be a internal and external QE of 100 %.

2.3.2.4 Responsivity

Responsivity is the metric by which we can tell how efficiently a signal is measured by the detector. It is a useful metric to compare against other detectors, as it is only concerned with the power of incident light in and the current produced. Formally it is a measure of how much current is generated from the detector given a specific input power of light, so the units used are A/W. Responsivity, R can be calculated using the equation,

$$R = \frac{\eta q}{hf}, \tag{2.5}$$

where q is an electron charge, h is Planck's constant, f is the frequency of light and η is quantum efficiency. The equation for response can be viewed as wavelength dependant when inserting the relation,

$$f = \frac{c}{\lambda} \tag{2.6}$$

where c is the speed of light and λ is the wavelength of light, to where finally the responsivity can be described as,

$$R = \frac{\eta q \lambda}{hc}, \tag{2.7}$$

in this form the proportional relationship between responsivity and wavelength can be seen, therefore the larger the wavelength the larger the responsivity. Maximising the responsivity of a photodiode is desirable so that the signal can be easily measured above noise, to increase the responsivity the quantum efficiency of the device should be increased. Methods to increase the quantum efficiency include:

- **Increasing the interaction length of the diode**. This allows more of the light to be absorbed, although this can increase dark current, described later.
- **Increasing the reverse bias on a detector**. By increasing the reverse bias on the detector a stronger E-field is created in the depletion region, allowing more electron-pairs to be collected before recombining.

- **Maximising Carrier lifetime.** That is the average time it will take a carrier to recombine. Maximising this by using a material and processing techniques that reduce defects in the detector.
- **Decrease detector width**. Reducing the width of the detector decreases the distance a carrier will travel before being being collected. Also allowing more electron-hole pairs to be absorbed before recombining.

2.3.2.5 Spectral Response

Spectral response is a description of the responsivity to light over wavelengths. When light is incident on a photodiode, the responsivity over wavelength is rarely flat. When the quantum efficiency of a detector is 100 %, responsivity increases linearly with wavelength, see Eq. 2.7. Further, the spectral response is related to the bandgap; bandgap energies of silicon and germanium are 1.1 eV and 0.66 eV resulting in cut-off wavelengths of 1.1 μm and 1.8 μm respectively.

An example of a spectral response of a silicon solar cell that is ideal with a quantum efficiency of 1 and a measured cell is shown in Fig. 2.7.

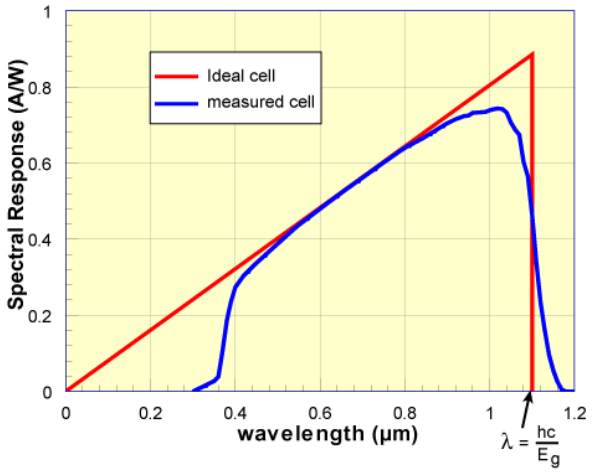

FIGURE 2.7: An example of a spectral response graph using a silicon cell (26).

Depending on the construction materials used in the detector it is also possible that absorption from another material would affect the spectral response.

2.3.3 Frequency Response

The frequency response refers to the detector's response to modulated incident light. This section covers the bandwidth and eye diagram.

2.3.3.1 Bandwidth

Bandwidth is a useful characteristic as it is a metric for the rate of data transfer a photodetector can support. Not to be confused with the wavelength bandwidth of a optical device. The definition of bandwidth is the frequency of modulated light when the power of the electrical signal is half that of when not modulated. This is the definition of bandwidth, used throughout this thesis, it is the 3 dB bandwidth and is measured in Hz. It is easier to appreciate this in a graph, see Fig. 2.8.

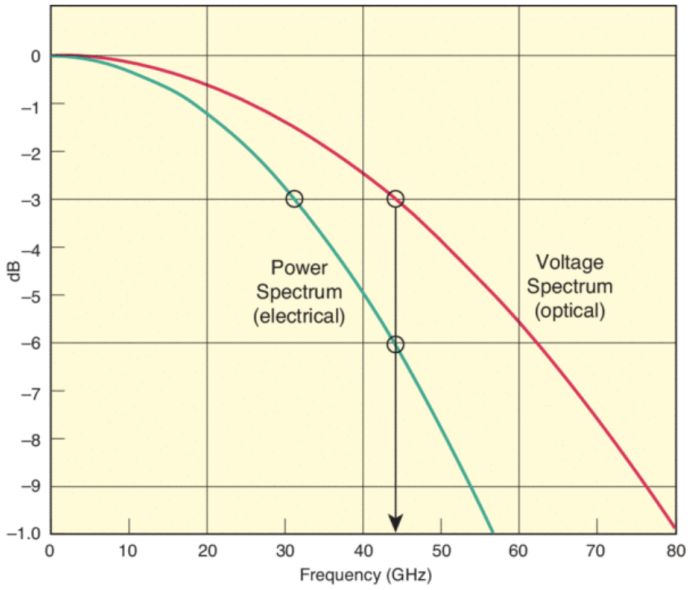

FIGURE 2.8: Example graph showing the 3 dB electrical bandwidth. The power of light is normalised to 0 dB at 0 Hz modulation. Once 3 dB of loss (half of the power) has occurred because of modulation to light, this frequency is noted as the 3 dB bandwidth. This graph also shows the optical bandwidth and how the 3 dB electrical bandwidth relates to the 6 dB optical bandwidth (27).

It can be important to know when something is referred to as the electrical or optical bandwidth of a photodetector. The optical bandwidth is the frequency of light modulation where the optical power is halved and is also measured in Hz. The electrical signal is related to the square of the optical signal, so in decibels the difference between optical bandwidth and electrical bandwidth is a ratio of two. Therefore, the 3 dB optical bandwidth is equivalent to the 6 dB point on the electrical curve.

It considers the detector simply as a capacitor, where the doped regions and the electric field between them would act as two charged plates with a field. Capacitance C is given by the equation

$$C = \frac{\epsilon A}{d}, \tag{2.8}$$

where ϵ is the permittivity of the dielectric material, A is the area of the faces of the doped areas in contact with the depletion or intrinsic zone and d is the width between the two doped regions, or the width of the depletion or intrinsic zone.

The frequency cut-off, which refers to the highest frequency of the detector or capacitor before the current flowing through it begins to reduce, this point is defined by a 3 dB of loss. The cut off is given as

$$f = \frac{1}{2\pi\tau}, \tag{2.9}$$

where $\tau = RC$ is the time constant of the circuit. By looking at the relation between frequency cutoff and RC, it is easy to see that reducing capacitance and resistance will increase the frequency response of the detector (28).

This largely speaks to the speed at which the carriers can travel. Less resistance allows carriers to travel faster through the device and less capacitance results in less capacitance to charge.

However by increasing the width of the depletion zone, the carriers then have farther to travel. In a real photodiode where there is the possibility of carrier recombination, the width of the depletion region needs to be balanced between having a longer drift distance and allowing more possibility for recombination.

The time it takes for the carriers to drift across the depletion region is affected by its internal electric field. A higher electric field, which can be created using a reverse bias, results in faster drifting and a higher bandwidth.

The RC time constant is not just affected by capacitance but also by the resistance of the contacts and load resistance. Reducing the resistance of the detector and circuit it is in increases bandwidth, this can be achieved, for example, by choosing low-resistance contact and detector material (29).

2.3.3.2 Eye Diagram

Though not a direct way of measuring the bandwidth or speed of a photodiode, an eye diagram can view the quality of a digital signal through a whole electrical system, detector included. It is an electrical measurement that looks at the rise and fall of signals.

In a binary digital sequence a signal will change between 1 - 0, on to off, high to low, etc in many combinations of sequence. An oscilloscope is used to read the high speed electrical signal being investigated. It looks at every possible combination of 2 transitions received (or 3 bit sequence), 1-0-1, 0-0-1, 1-1-1 etc., and overlays them to create an eye diagram, see Fig. 2.9. The eye diagram is displayed with time on the x axis and amplitude in voltage on

the y axis. The signal is read and the combinations are acquired from many samples. Because of this, variations in the signal are also overlayed and included in the eye diagram. This ensures that it is a representation of the system measured, which will naturally have variation and loss.

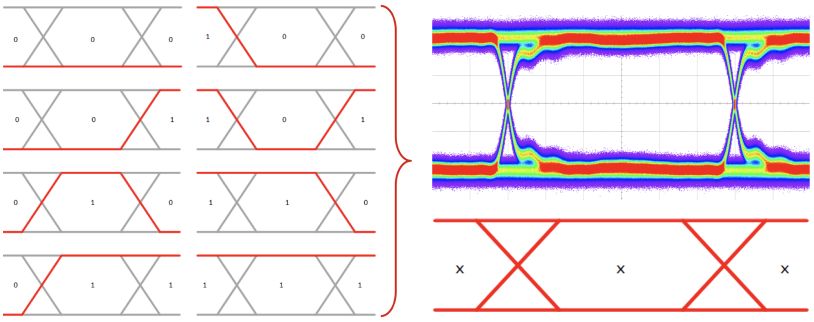

FIGURE 2.9: Diagram showing the different possible transitions that will be overlapped and a realistic example of an open eye diagram (30).

An eye diagram can be used to look at the different amplitude and time parameters of the signal, i.e., the amplitude of the signal, rise and fall time of the signal, impedance mismatches, signal to noise ratio as well as jitter effects as shown in Fig. 2.10.

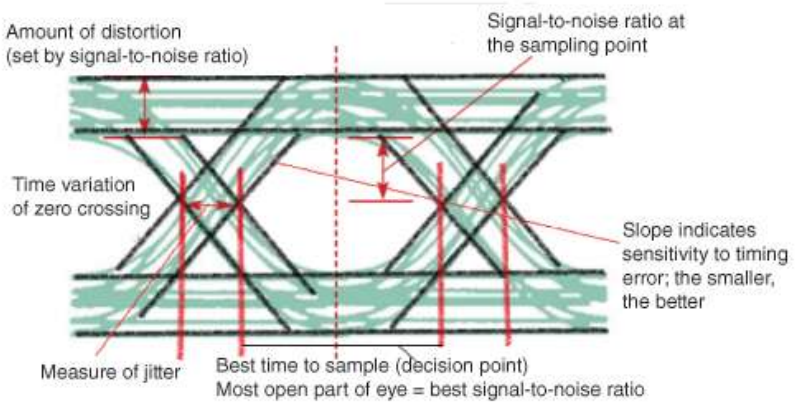

FIGURE 2.10: Diagram showing the different possible transitions that will be overlapped and a realistic example of an open eye diagram (31).

As an example, an eye diagram pattern from a microwaves photonic link is shown in Fig. 2.11. It shows that as the modulation of the light is increased the eye begins to close slightly. This closing and the widening of the top and bottom of the diagram show a decrease in the signal to noise ratio. The widening of the crossover point signifies an increase in jitter.

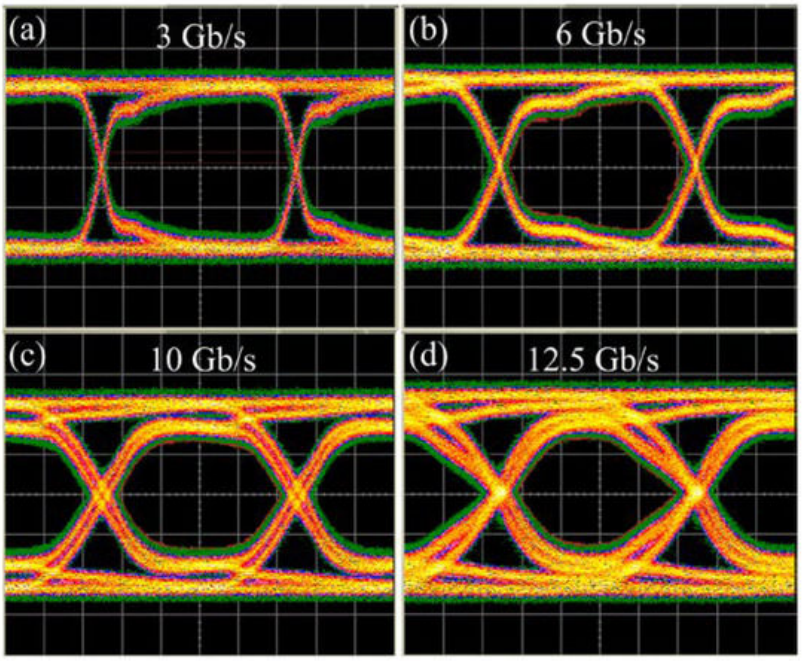

FIGURE 2.11: Example of an open eye diagram with increasing modulation of light. This is the eye diagram pattern of a microwave photonic link (32).

Chapter 3

Nanofabrication Processes

Nanofabrication is the process of creating devices and structures on the nanoscale. A large branch of this used to create integrated electronic circuits on a microprocessor chip, which can be found in smart phones, computers, gaming consoles and more. The field of nanofabrication extends beyond creating electronic chips and in the case of this thesis even photonic integrated circuits.

While the fabrication processes used are all different and have broad applications, most operate by depositing/removing layers of materials to build nanoscale devices. An example of a structure being fabricated is shown below in Figure 3.1 to show the layered process of creating a waveguide.

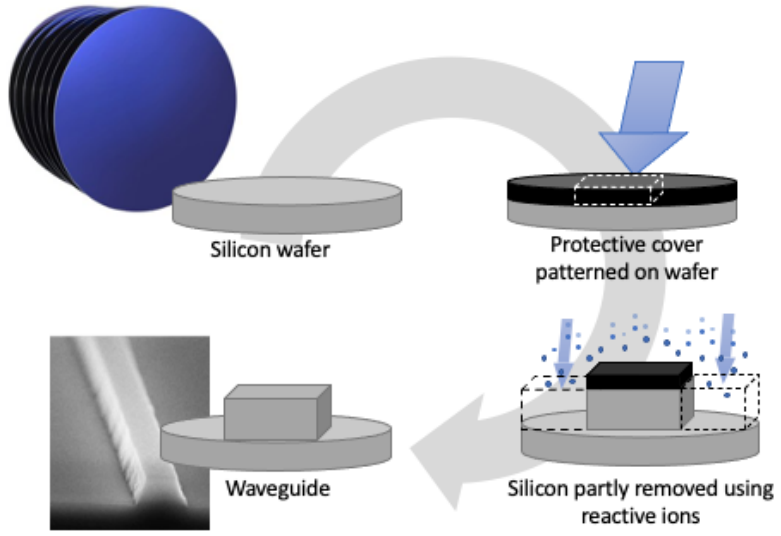

FIGURE 3.1: An illustration of a waveguide being fabricated, showing the layer by layer process. A silicon wafer is covered with patterned E-beam resist. E-beam resist is used to protect waveguide during etching process with removes selected areas of the silicon. The E-beam resist is removed after to reveal the waveguide.

This chapter will describe the fabrication methods used to create the photodetectors in this thesis. It will begin by describing the lithography process, then move onto the processes used to deposit material then finally the other remaining processes.

3.1 Lithography Process

Lithography in art began with using greasy crayons to write script on limestone slabs. Ink would soak into the limestone and the greasy crayon marked area would repel any ink. This allowed the image on the slab to be used to print the script repeatedly.

In nanofabrication, lithography is similar in that selected areas can be exposed to processes whilst others are intact through the use of a protective material. It is used to only expose some of the wafer or chip to processes, as shown in Figure 3.1. It is similar to the artistic definition, though instead of greasy crayons we use a protective material called E-beam resist and instead of ink the wafer is exposed to layered deposition or etching for example. A visual summary of the lithographic process is shown in Figure 3.2.

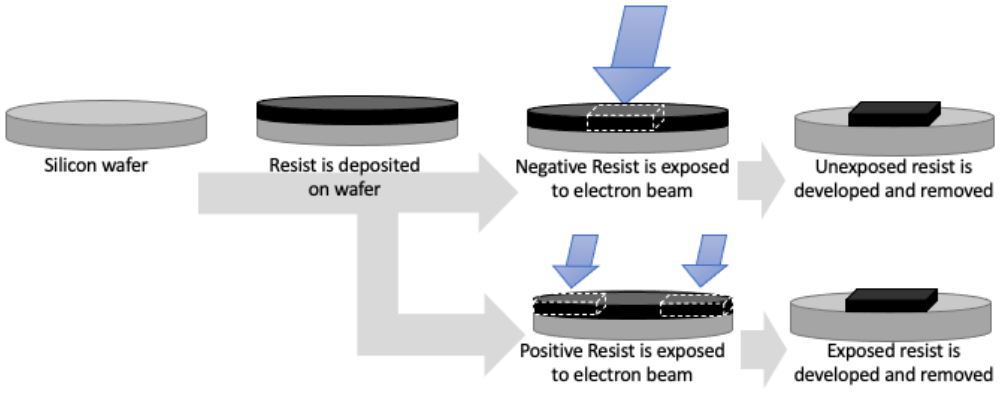

FIGURE 3.2: Diagram showing the lithographic process using both positive and negative E-beam resist.

To give an overview of the nanofabrication lithography process: It begins by depositing a material called E-beam resist on the wafer as a uniform layer. Next, when the E-beam resist is exposed to radiation, the chemistry of the material changes, to harden or soften depending on the type of E-beam resist. After being radiated, the wafer is then "developed" which means to use the appropriate liquids to remove the softer areas of the E-beam resist which reveals a pattern. Planar processes such as etching and deposition can then performed and with the E-beam resist covering only certain parts of the wafer, selected areas can be fabricated on to create nanoscale structures and devices. Once the processes are performed the E-beam resist can be removed.

The radiation is selectively exposed to the E-beam resist on the wafer through a couple of methods. Though for this thesis, only an electron beam was used. An electron beam scans across the wafer with nanoscale accuracy to radiated selected areas.

The following subsections will describe each of the electron beam lithography steps in detail, beginning with spin coating.

3.1.1 Spin Coating

Spin coating is a common way of applying a E-beam resist layer over a wafer or chip. E-beam resist is an organic material and starts in a solvent form, with particles of the solid E-beam resist suspended in alcohol.

When exposed to radiation, a positive E-beam resist will become soluble to the developer and in a negative E-beam resist, the polymers will cross-linked when exposed, becoming insoluble, meaning the soluble regions that were not exposed to the radiation will wash off in developer. The solvent E-beam resist is applied to the wafer using a pipette then is spun at high RPM to pull the liquid E-beam resist uniformly across the wafer. The faster the spinning the thinner the E-beam resist. The thickness of E-beam resists are typically anywhere between hundreds of nanometers up to one or two microns. A diagram of the process is shown in Figure 3.3.

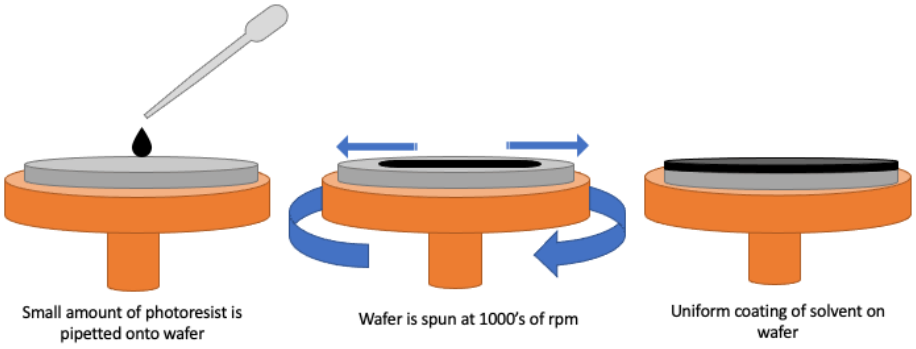

FIGURE 3.3: Diagram showing the dropping of liquid E-beam resist onto the wafer and spun.

Once the E-beam resist has been 'spun' it goes for a 'softbake', this is a fast heating process that can take place on a hotplate to a temperature of about 100 °C to remove remaining solvent in the E-beam resist, solidifying and hardening it. The softbake time needs to be carefully set to avoid defects and cracks in the E-beam resist which would expose unintentional parts of the wafer to later processes. If the solvent is left to evaporate without baking or if the softbake time is too short, bubbles may form in the E-beam resist.

Following the E-beam resist soft baking, it is exposed to radiation, which is described in the next section.

3.1.2 Electron-beam (E-beam) Lithography

Lithography uses radiation to change the chemical bonds within the E-beam resist so that, once developed after, will reveal the desired pattern. Electron beam uses a beam of focused high energy electrons to 'draw' the pattern (i.e waveguide, doping region) directly onto the E-beam resist, an illustration of which is shown in Figure 3.4.

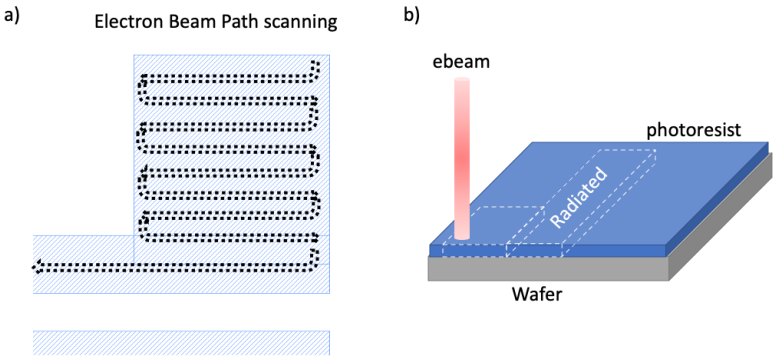

FIGURE 3.4: Diagram showing a) a top down view of a layer and how the electron beam would scan across with surface b) how the E-beam resist would be exposed to the electron beam.

Wafers will likely go through more than one round of lithography to allow different areas to be exposed to different processes. The alignment between lithography stages is maintained with the help of alignment marks. These are small identifiable crosses that are etched into the wafer; creating these marks should be part of or the first step in a lithgraphy and etching process (33).

3.1.3 E-beam resist Developing and Stripping

Developing removes the softer part of the E-beam resist after being exposed to electron beam radiation; by washing off the soluble E-beam resist with a solvent developer.

After this, subsequent processes can be performed, with the help of the patterned E-beam resist to protect layers below. When the desired processes are complete and the E-beam resist is no longer needed it is removed from the substrate; this is known as stripping the E-beam resist (33). Two stripping techniques are used in this project; oxygen plasma and acetone. The use of oxygen plasma takes place in a vacuum chamber where the highly reactive monoatom of oxygen reacts with the organic E-beam resist and is then pumped out. Acetone dissovles the E-beam resist.

It is common for there to be multiple lithography steps in the creation of a device. In that case it begins again with spinning a E-beam resist.

3.2 Thin Film Deposition Processes

Deposition of thin films allows the addition of the same or different material to a wafer and can provide a variety of functions to a device by creating metal contacts, act as insulation, build ribs for waveguides, create gain regions in lasers and more. This is only possible due to the range of materials that can be deposited as thin films. There is not a single method used for all depositions and each method comes with trade-offs. The fabrication of detectors in this thesis is concerned with two deposition methods, described below; Plasma-Enhanced Chemical Vapour Deposition (PECVD) and Electron-beam Physical Vapor Deposition; used for SiO_2 and metal deposition respectively.

3.2.1 Plasma-Enhanced Chemical Vapour Deposition

This deposition method is often favoured over regular chemical vapour deposition (CVD) because it enables lower temperatures, whilst still maintaining the same deposition rates. This is useful for example if a device already has aluminium contacts, which has a melting point of 650°C.

PECVD is performed in an enclosed chamber, a wafer is placed on a chuck within. The chuck is a platform that acts as an electrode and will also heat the wafer. The source gases, precursors for a reaction which forms the desired solid, are brought in from the showerhead shaped electrode above the chuck. The gases are pumped down below the chuck and a plasma is created in the gas by an alternating electric field between the two electrodes.

$$SiH4(g) + 2N2O(g) -> SiO2(s) + 2H2 + 2N2 \tag{3.1}$$

Variables in crafting recipes for PECVD depsotion include chamber pressure, temperature, flow rate, flow ratio between gases and the RF power (34).

3.2.2 Electron-beam Physical Vapor Deposition

Electron-beam physical vapor deposition is another process used to deposit materials, often metals, onto a wafer. The process is straightforward and best described using a figure, see Figure 3.5. Within a high vacuum chamber, a focused beam of high speed electrons bombard the target metal material. The metal which resides in a crucible is heated until it evaporates. Hot metals have a high vapor pressure, and in this gaseous state, will travel towards the wafer and get deposited when they make contact.

The wafer is usually heated to improve surface quality as it allows atoms to diffuse in the films and find favourable lattice positions, eliminating possible vacancies (34).

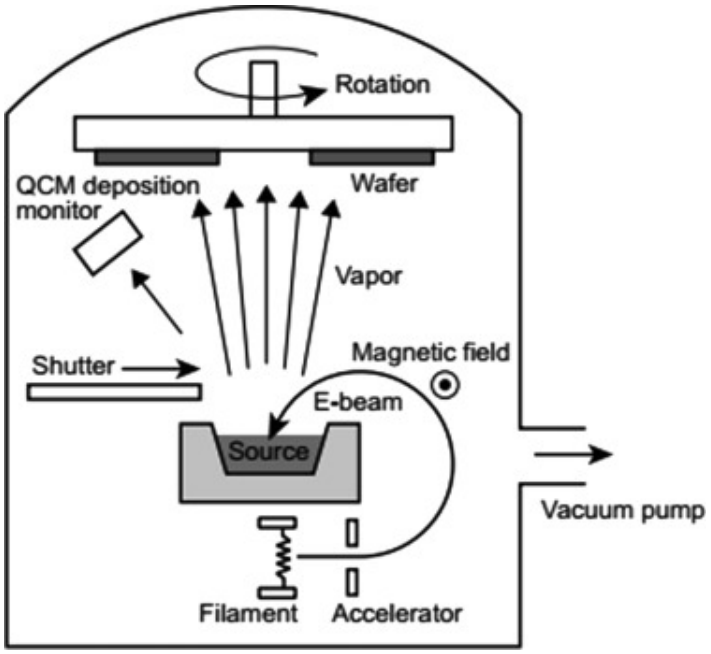

FIGURE 3.5: Diagram showing a cross-section of an electron beam physical vapour deposition. The filament creates electrons which are accelerated and directed with a magnetic field into the metal source. The metal evaporates upwards towards the wafers (35).

3.3 Other Processes

3.3.1 Inductively Coupled Plasma – Reactive Ion Etching (ICP-RIE)

Similarly to PECVD, a plasma of gas is created in the chamber from a high frequency oscillating electric field. Instead of the gaseous ions reacting to form solids, they can etch in two ways: by reacting with the surface to create volatile compounds, or physically by bombarding and removing surface ions with kinetic energy. The form of etching that occurs depends on the recipe chosen.

3.3.2 Rapid Thermal Annealing (RTA)

RTA is a process that allows the wafer to be heated to temperatures above 1000 °C) in seconds. For example the Jiplec Jetfirst 200 used in this thesis can have a ramp rate between 1 °C/s to 200 °C/s (36). This is often done to activate dopants and repair damage done to the crystal. The dopants are activated through the use of high temperatures which provide energy to the dopants sitting between lattice points and allow them to create bonds with the material around them to becoming a part of the crystal lattice. This provides the desired electronic properties from the dopants mentioned in section 2.1.3.

RTA operates in a furnace and contains a pyrometer and thermocouple to allow the temperature of the wafer to be monitored. The thermocouple is in contact with the rear of

the wafer and pyrometer uses IR light to measure temperature. Heat is created in the furance with heating lamps.

3.3.3 Ion Implantation

Ion implantation is the process of firing accelerated ions into a material. They are slowed by random collisions with the wafer material. Ion implantation is often used to dope semiconductors, also discussed later in the thesis in section 4.2, implanting ions has other benefits too. The implantation depends mainly on two variables, ion dose and implantation energy, which is the energy of acceleration. The ion concentration within the substrate follows a Gaussian distribution, peaking at a specific depth. Typical ranges for implantation doses and energies are around $10^{10} - 10^{16}$ ions/cm^2 and 10-200 keV (37). Ion implantation takes place in a machine called an implanter. In an implanter the ions are accelerated within a vacuum to a high speed then fired into the target material, the path of the ions into the target wafer is shown in Figure 3.6. The ions are produced from the ion source. They are then directed through a magnetic field and an aperture, the combination of which allows the desired ions through. As the radius of movement of an ion through the magnetic field is related to the ratio of mass to charge (m/e) and only ions of the desired ratio would pass through the aperture. They are then accelerated to high energies and directed towards the target using electromagnetic field generated with 'scan plates'.

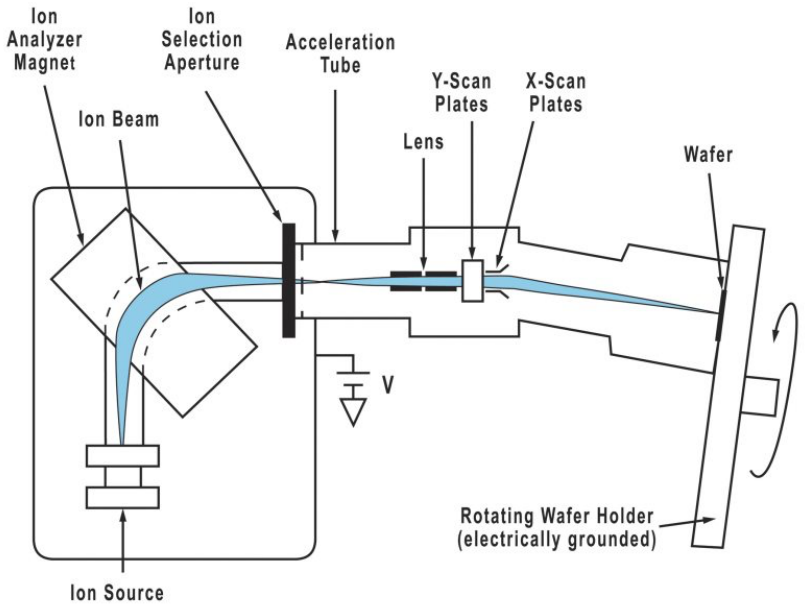

FIGURE 3.6: Diagram of an implanter - this shows the ion beam path from start to wafer (38).

Chapter 4

Mid-Infrared Photodetection State of the Art

This chapter will explore the literature of integrated MIR detectors made from different materials and compare their performance. It will discuss these detectors in terms of responsivity, bandwidth, fabrication and CMOS compatibility. In terms of materials, we cover Germanium-Tin (Ge/Sn) alloy, defect mediated detection in group 4 materials, III/V semiconductors, 2D materials and chalcogenides.

4.1 Germanium-Tin Photodetectors

Ge/Sn is an alloy that has become a forerunner for monolithic, MIR detection due to the following features:

- Operation wavelength can be tuned by altering Ge/Sn ratio.
- An indirect to direct bandgap transition that occurs at 0.06 - 0.11 ratio of Sn to Ge (depending on strain within device).
- Can be monolithically integrated on Si platforms.
- Can be created using mature fabrication technology.
- Has potential to be used for detection and laser radiation.

These features make Ge/Sn a practical option for MIR detection, although has not yet shown detection on a waveguide integrated detector in the 3-4 μm spectral region unlike other waveguide integrated photodiodes (11). Further, to reach these wavelengths the detectors require larger Ge/Sn ratios (39), making the growth of a quality crystal difficult.

First it is due the low solubility of 1%, requiring, e.g., using low non-equilibrium temperature during epitaxy. Second, with increased ratios, the strain introduced by Sn and defects in the layer will result in non radiative absorption (40). To allow large compositions of Sn the following techniques have been used: Utilizing eutectically-enhanced crystallization, Sn nanodot enhanced composition enhancement and spontaneous relaxation-enhanced Sn incorporation process. These processes have allowed Sn compositions as high as 22.3% and 26% (39) (41).

Despite these difficulties, having a material that would allow both lasing and detection in that 3-4 μm region is worth pursuing. Recent publications have shown effort to increase the bandwidth with the hopes that the material is also capable of being used for transceivers and telecommunication applications. An example of this is a Ge/Sn based multiple quantum well (MQW) with a bandwidth over 10 GHz at 2 μm, although this device is not waveguide integrated (42).

Table. 4.1 compiles the most notable detectors made from Ge/Sn alloy.

TABLE 4.1: Integrated MIR Ge/Sn Photodetectors

Ge/Sn ratio	Responsivity	Bias	Spectral Range	Band-width	Year	Ref
9 %	0.1A/W @ 2.2 μm	-5V	1 - 2.2 μm	N/A	2012	(43)
10 %	0.26 A/W @1.55 μm	-5V	1.4 - 2.4 μm	N/A	2015	(44)
9 %	0.33A/W @2003 nm	-10V	1.5 - 2.0 μm	N/A	2016	(45)
10 %	0.023A/W @2003 nm	-1V	1.5 - 2.0 μm	1.2GHz	2017	(46)
9.24 %	0.19A/W @1.6μm	-0.01V	1.6 - 2.4μm	1.78GHz	2019	(47)

4.2 Sub-Band Absorption in Group IV Photodetectors

While the instrinsic bandgap of Si allows absorption up to 1.1 μm it has been shown to extend up to 2.5 μm and even higher through the use of sub-band absorption. Sub-band absorption of light is detection through the use of deep levels created within the instrinic bandgap of a material. These levels allow for smaller energy transitions and longer wavelength of light to be absorbed than can be achieved using intrinsic material. To create these levels research groups have used ions such as Si^+ (48), B^+ (49), Se^+ (50), Au^-(51) and

Zn^+(52) to bombard and create defects in Si; an example of the implanted structure is shown in Figure 4.1. More recently this principle has also been used to create Ge photodetectors by using Au^-(53), this has shown an enhanced cut-off wavelength of up to 3 μm. As well as finding absorption at 2.0 μm in Ge PIN photodiodes which has been mediated through defects created during fabrication (54). Similarly to Ge/Sn detectors, this method lacks responsivity above 3 μm but its advantage is that fabrication is simple and only requires an additional back-end ion implantation step to create defects. Room temperature Si defect-mediated detectors have been shown to detect up to a wavelength of 2.5 μm (2), with responsivities of up to 50 A/W as well as with bandwidths of >35 GHz whilst maintaining a responsivity of up to 10 A/W in avalanche mode (55). The challenge is maintaining high responsivity and bandwidth at the same time whilst extending the spectral range further into the MIR.

A summary of recent defect-mediated detectors is given in Table. 4.2.

TABLE 4.2: Integrated MIR Sub-band Photodetectors

Type of Implant	Responsivity	Bias	Spectral Range	Band-width	Year	Ref
Si^+ in Si	up to 10 A/W	up to -20 V	1.1-1.75 μm	35 GHz	2009	(55)
B^+ in Si	0.3 A/W	-30 V	2 - 2.5 μm	15 GHz	2015	(49)
Si^+ in Si	9.9 mA/W	-5 V	2.2 - 2.35 μm	1.7 GHz	2014	(56)
Se^+ in Si	25 mA/W	-3 V	0.9 - 1.6 μm	N/A	2011	(57)
Au^- in Si	EQE 10^{-4}	-5 V	2.2 μm	N/A	2014	(58)
Zn^+ in Si	87 $\pm$ 29 mA/W	-20 V	2.2 - 2.4 μm	N/A	2014	(52)
Au^- in Ge	0.25 mA/W at 2 μm	0 V	2 - 3 μm	N/A	2020	(53)

It's historic perspective is given in more detail on sub-band absorption and how it has progressed is given in the following section.

4.2.1 History of Silicon Defect-Mediated Photodetectors

This section gives a summary of the history of integrated silicon and germaniam defect mediated waveguide integrated detectors at NIR and MIR wavelengths.

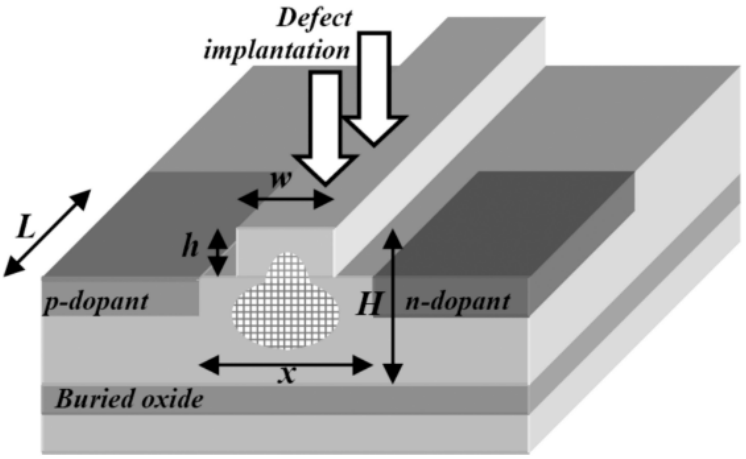

FIGURE 4.1: Diagram of implanted PN junction, shown as an example of general device structure (59).

In 1959, H. Y. Fan *et al.* irradiated silicon using electrons and deuterons and found absorption bands introduced at 1.8, 3.3, 3.9 and 5.5 μm (60). The absorption peak at 1.8 μm is now associated with the divacancy defect, used in integrated photodetectors.

Integrated detectors that used defect mediated absorption began in concept from a paper from P. G. Kik (61). In 2000, the same group found that erbium doped silicon PN junctions can be used to elicit an infrared response (62). In 2002, a paper was published showing proof of this on an integrated platform. This paper introduced the concept using erbium doping on a Si-on-Insulator (SOI) PN junction to allow the absorption of 1.5 μm light (61). It showed absorption of 1.5 μm light with a quantum efficiency of 10^{-4}. A cross section of this device is shown below, see Figure 4.2.

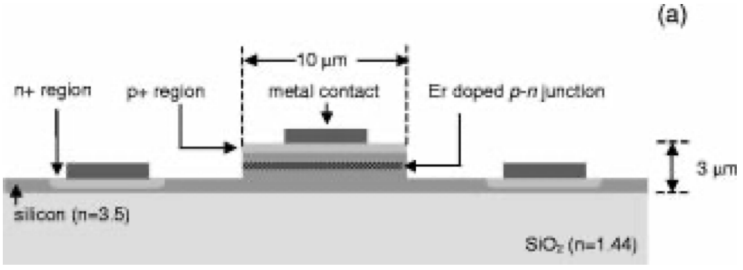

FIGURE 4.2: Early defect mediated waveguide integrated device (61).

The next development of integrated sub-band infrared (IR) photodetection came with a PIN photodiode fabricated in 2003 by Knights *et al.* which used proton bombardments to create defects (63). This novel device had a responsivity of 8 mA/W with a reverse bias of -1 V, the operation wavelength in the C and L bands, and showed an improved response compared to an equivalent unimplanted device (63). The group then published a paper in 2005 with details of a photodiode with a responsivity of 3 mA/W at 1550 nm, as well as

including graphs showing the improved response of the devices with a shorter PN junction distance from the rib design, showing the need for device design optimisation (64).

In the following year, they extended this work further, showing PIN junctions implanted using Si+ ions and an investigation into post-annealing temperature. This revealed that annealing at 300 °c for 10 minutes post implantation gives the largest response which was consistent with annealing data for the silicon divacancy. Thus absorption was assumed to be dominated by the divacancy defect (65).

The next large step in defect detectors came from Guis *et al.* (48). where they demonstrated an Si^+ implanted photodiode responsive from 1100 nm to 1750 nm, up to 50 A/W responsivity and capable of 35 GHz bandwidth. These detectors relied on the interstitial cluster defect, this was concluded because of information on defects stability under annealing again, divacancies anneal out at 300°c whereas the interstitial cluster is stable up to 600°C (48). In 2013, Souhan *et al.* published a paper showing, again, a Si^+ implanted detector, although they measured a 0.14 A/W responsivity of the device at 1.9 μm and the following year demonstrated a device capable of absorption up to 2.3 μm, showing an effort to extend spectral response further in the infrared (66). These detectors both relied on interstitial clusters.

It was around 2013 where interest in using the defect-mediated MIR detection in silicon took off. Devices were fabricated using different ions to create defects which achieved spectral responses up to 2.5 μm through implanting boron, up to 2.4 μm using substitutional zinc defects and up to 2.2 μm by using gold ions (67; 52; 58). Until 2015 the 2 - 3 μm response from these detectors was below 100 mA/W, the next significant innovation came from Ackert *et al.*, where they created a responsive, high speed detector of 0.3 A/W at 2.02 μm by operating it in the avalanche regime, with a reverse bias of up to -30 V (2).

From here the next step has been that defect mediated detectors have started to branch out into germanium by using gold ions. Detectors have beeen created showing an enhanced cut-off wavelength of up to 3 μm (53); as well as finding 2 μm absorption in Ge PIN photodiodes which has been mediated through defects created during fabrication (54).

In summary, the main defects responsible for photo absorption in silicon are the divacancy, interstitial and various substitutional defects, such as Gold and Zinc. The more responsive of which are the interstitial and divacancy. Both can be created through bombardment of protons, Si+ and B+ ions. The neutral divacancy responsible for many of the photoabsorption in the earlier photodiodes has a 1.8 μm wavelength absorption band, E = 0.4 eV. It was shown that photodiodes annealed above 200°C started repairing unwanted defects and that largest photo absorptions occured with an anneal of 300°C before the divacancy is completely removed at 350°C. The excess loss still present in a device would likely be attributable to the cluster interstitial, another stable defect that is present until annealed at 475°C. There is also still room to explore Ge as a defect mediated detector.

4.3 III-V Photodetectors

III-V semiconductors are a popular material choice for infrared detectors and these alloys are used to cover the spectral range across the wide MIR region. While III-V detectors have shown excellent performance in terms of MIR responsivity, they are not easily integrated on a silicon platform because of the lattice mismatch between materials, a graph showing the difference in lattice constant is shown on Figure **??**. Having a III-V on Si platform then leads to a more expensive fabrication and limits its use in low cost high volume applications. To integrate III-V materials there are a few methods available to bond the material to the substrate i.e., flipchip bonding, heterogeneous bonding and hetero-epitaxial growth (68).

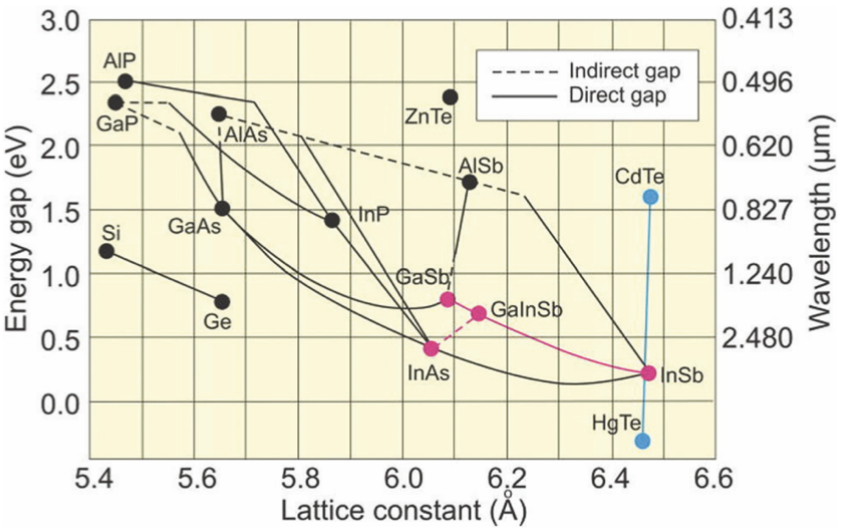

FIGURE 4.3: Table showing the bandgap energy and lattice constant difference between materials (68).

Epitaxial growth, as a monolithic method, is most preferable, as it would offer the possibility for low cost, high yield and density of III-V devices on Si. Although is made difficult to have have a defect free material growth because of lattice mismatch between the materials and a difference in thermal expansion coefficients leads to defects near the boundary between materials, introducing defects like threading dislocations and micro cracks (69; 68).

Discussed in the papers listed in Table 4.3, a type of wafer bonding using an adhesive divinylsiloxane-bis-benzocyclobutene (DVS-BCB) is often used by M. Muneeb *et al.* at Ghent University (12). It's well suited in prototype because it requires less surface preperation than other methods and does not need as low surface roughness, contamination and cleanliness (69). Although the adhesive absorbs in the 3 μm wavelength range so has to be accounted for in MIR applications (12). Most III-V waveguide integrated photodetectors can only operate up to 4 μm. There are examples of

long wavelength detectors (>4 μm) that operate at higher speeds (20 GHz) but these detectors are not integrated on a silicon substrate (70). A cross section of a InP hetrogeniously integrated detector on silicon is shown in Figure 4.4.

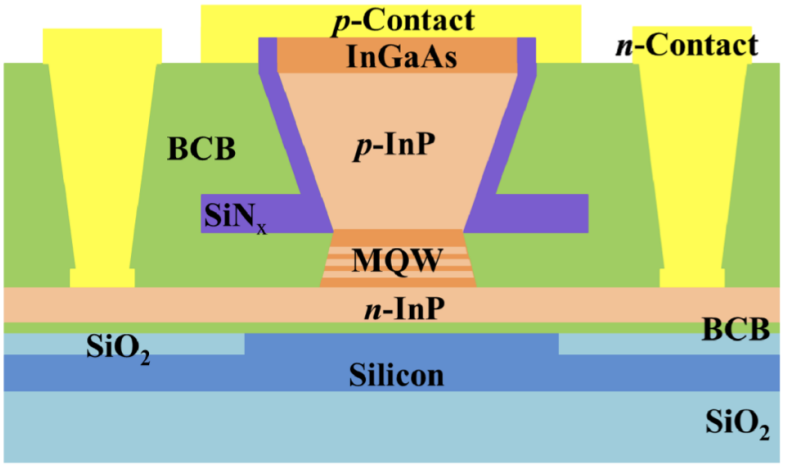

FIGURE 4.4: Cross-section diagram of InP MQW, light is coupled from the active region to the silicon via a 180 μm long InP taper (71).

Below shows a table compiling III-V integrated photodectors on a silicon platform.

TABLE 4.3: Integrated MIR III-V Photodetectors

Material	Responsivity	Wavelength	Ref
InP	1.2 A/W	2.32 μm	(71)
InAsSb on GaSb	0.3 A/W	3.8 μm	(12)
GaInAsSb	1.4 A/W	2.3 μm	(72)

4.4 NIR Germanium Photodetectors

Epitaxially growing Ge-on-SOI is difficult because of the lattice mismatch of 4.2%, although despite this there are many examples of device grade crystalline germanium (73). Growth methods used to overcome the lattice mismatch include; poly Ge films, epitaxial growth on graded SiGe buffer layer, low temperature/high temperature growth (74).

NIR Ge detectors are used to detect in the telecommunication windows and often the choice of material for detection at this wavelength region because of the mature fabrication, CMOS compatibility and good performance. Detectors have been made with high responsivity, high bandwidth and low dark currents (75). An example of this is a PIN Ge photodiode with 3 dB bandwidth of 42 GHz (76). Recent publications have also shown

optimised detectors with quantum efficiency of 90 % with an average responsivity in the C-band of up to 1.16 A/W at -3V bias (77).

4.5 Other Materials

Other materials and methods of MIR detections are possible using chalgonide materials, bolometers, and photoaccoustic sensing.

The ability of monolithic integration of PbTe makes chalcogenides a candidate for a low cost MIR detector. Limited literature exists for integrated MIR detectors. In terms of applications, Han *et al.* has demonstrated PbTe detectors capable of 1 A/W responsivity at 2250 nm hoping to be used for chemical sensing, night vision and medical diagnosis and has used the same design as part of a functional MIR methane gas sensor (78; 79)

Bolometers are useful because they can operate over a large wavelength region, do not need cooling at long wavelengths and are also CMOS compatible. Bolometers operate by absorbing the MIR radiation, which generates heat that is measured as the change in resistance on the antennas. Responsivity is not a characteristic used in bolometers but the efficiancy of these detectors are instead measured by the percentage change in resistance per kelvin. An example of this is a bolometer by Wu *et al.* who demonstrated an amorphous-Si bolometer with gold antenna (80). The measure of sensitivity is 1.13 ± 0.04% K^{-1} and a NEP of 66 $\mu W/\sqrt{Hz}$.

2D materials such as black phosphorus and graphene are both able to absorb MIR light using direct tuneable bandgaps. Graphene specifically has garnered attention for it's high electron mobility and wide tuneable spectral range. 2D materials are well suited to integrated photonics in some regards, as the VDW bonding means there is no lattice mismatch in the materials and by placing the material parallel with a waveguide can maximise overlap with the guided light, see Figure 4.5. Black phosphorus has also been a promising material for detection because of it's broadband detection, direct bandgap and depending on layer thickness the bandgap can be altered from 0.35 eV to 2 eV as a bulk and single layer material respectively; allowing absorption of visable to 4 μm (81). However currently the fabrication of these 2D materials as integrated detectors, is difficult to produce high yields. There are many fabrication techniques, both materials still relying on mechanical exfoliation, chemical vapour depostion, epitaxial growth, which has the downsides of being low yield, or presents defects (82).

4.6 Project Motivation

To create a MIR detector that can an inexpensive addition to PICs, the focus of this thesis is to extend the spectral range of group IV defect mediated detectors.

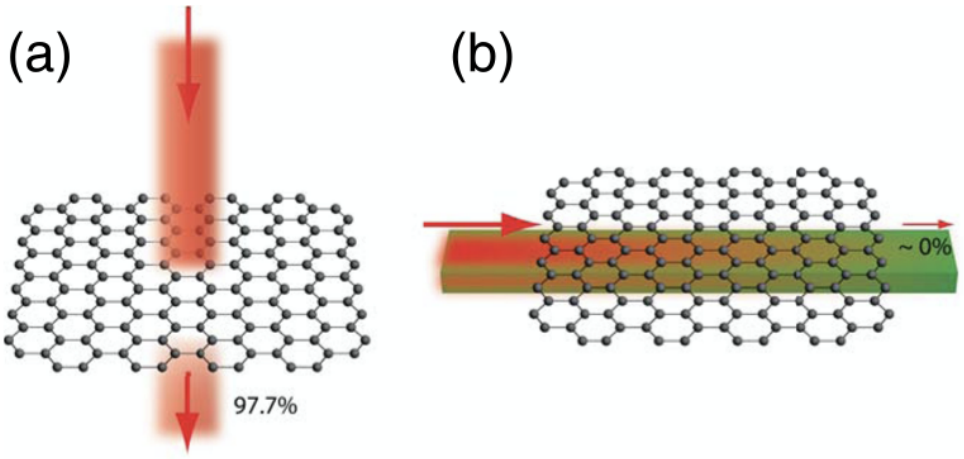

FIGURE 4.5: Diagrams two ways light can interact with graphene (a) Light is perpendicular to the graphene and only has an absorption coefficient of 2.3 %. (b) When graphene can interact with the evanescent field on a waveguide its absorption is only limited by the length of the waveguide (83).

TABLE 4.4: Integrated Photodetectors - Other Materials

Material	Responsivity	Bias	Wavelength	Bandwidth	Ref
PbTe	1 A/W		2.1 - 2.5 μm	-	(78)
Graphene	0.13 A/W		2.75 μm	-	(84)
Graphene	2.2 mA/W	-1V	3.80 μm	-	(85)
Black Phosphorus	2 A/W	-1V	4 μm	-	(11)
Black Phosphorus	0.098 A/W		3.825 μm	550 Hz	(86)

Silicon defect mediated detectors has been explored over the past two decades and some papers exist to prove the same functionality in germanium though the spectral range is still comparable to silicon, in the 2 - 3 μm region (54; 53). However, if defect mediated absorption can be used to extend the spectral range of silicon into the 2 - 3 μm region it would be interesting to further explore germanium as a defect mediated detector. Extending it's wavelength cut-off of 1.8 μm hopefully into the 3 - 4 μm range. Germanium detectors of this design also have the potential to have a larger bandwidth compared to silicon as it has a larger electron mobility. Successfully creating this would provide a CMOS compatible, inexpensive, small footprint photodetector that can detect further into the MIR and be usable in PICs of interest in free space telecommunication or sensing chemicals.

The design of this thesis's germanium defect mediated detector has been closely guided

from its silicon predecessors, so will also follow a waveguide integrated PIN junction design.

4.7 Summary

It would be useful to bring the mature detector and laser technology of III-V semiconductors to integrated photonics; however they all suffer the same downfall. They are difficult to monolithically integrate, meaning they are usually added to the silicon chip by processes such as flip-chip integration or in-plane butt-joint coupling. These methods do not work well for mass volume fabrication as the yield is low, the difficulty lies in aligning two materials together, which requires a sub-micron alignment (87).

2D materials such as black phosphorus and graphene are both able to absorb MIR light. Graphene specifically has garnered a attention for it's high electron mobility and wide tuneable spectral range. 2D materials are well suited to integrated photonics in some regards, as the Van der Waals (VDW) bonding means there is no lattice mismatch in the materials and by placing the material parallel with a waveguide can maximise overlap with the guided light. However currently the fabrication of these 2D materials as integrated detectors, is difficult to produce high yields.

MIR absorptive materials that are not limited by complex, expensive and heterogeneous fabrication restraints include using Si and Ge through sub-band means and Ge/Sn alloys. Both of which can be monotonically integrated although their spectral response is limited to the 2-3 μm region.

The PhD motivation of creating a germanium defect mediated photodiode that aims to be responsive in the 3-4 μm region is introduced.

Chapter 5

Device design

This chapter covers the final detector design in three sections. The first will describe the motivation of the detector design and the basic outline of the design along with the dimensions and parameters that need to be decided. The second section shows the process of designing the photodiodes, involving choosing a platform, performing simulations to design waveguides and grating couplers, and using literature to inform other parameters of the devices. The third section describes the final photodiode design, the layout of devices on chip and the complete wafer layout for fabrication.

5.1 Initial PIN Junction Design

5.1.1 Base Design Structure

The structure of a straight rib waveguide integrated PIN junction was used as a base to begin designing the photodetector, as it was used for silicon defect mediated detectors, and chosen for its simple design and fabrication (2).

Grating couplers were chosen to couple light into the detector as opposed to cleaved surfaces for butt coupling. A butt-coupling method is usually chosen to allow a broad spectrum of wavelengths to be coupled, but the lasers available for characterising for this project are not tuneable over more than 150 nm, a bandwidth which grating couplers can already operate over. Using grating couplers also makes characterising the detectors easier, as butt coupling is trickier to align and most of the current setups in the labs are setup for fibre to grating coupler coupling.

The devices where chosen to be fabricated on a 500 nm Ge-on-SOI wafer, as these wafers have a higher refractive index contrast compared to other options that transmit MIR such as Ge-on-Si. A high index contrast allows smaller devices to be made which in turn would create a more responsive device, see 2.7 for more details. Also, spare wafers remained that

were used for the successful fabrication of other passive MIR germanium devices from members of our group working in the same wavelength range. (13). The SiO_2 substrate wasn't expected to be an issue, as it absorbs light above 4 μm and the detectors were never expected to be responsive above this wavelength. The wafers comprised a top layer of 500 nm germanium, 60 nm silicon and finally a 3 μm silica BOX layer. With the base structure of the detector chosen, this left some parameters to be decided, which are illustrated from a cross-section and top down view in Figure 5.1 and Figure 5.2 respectively. The unknown dimensions to be decided were are as follows:

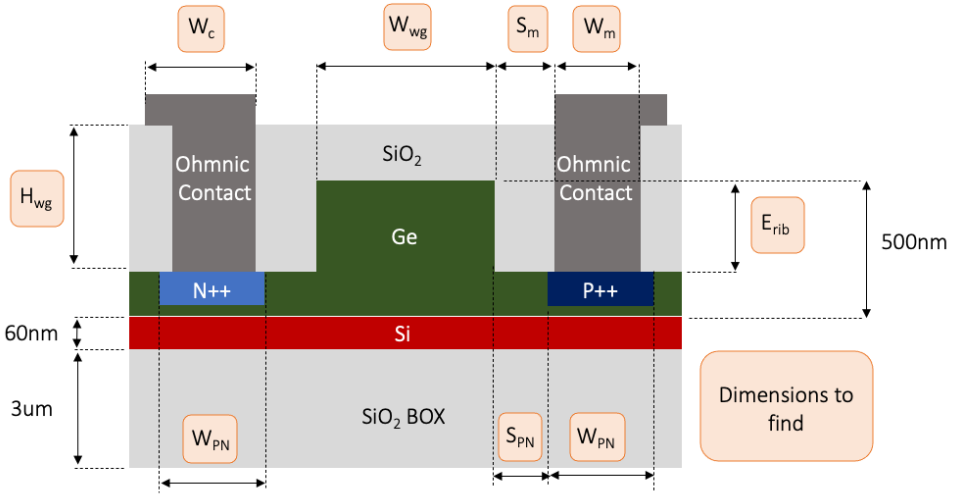

FIGURE 5.1: A cross-section view of the base rib waveguide design. Showing dimension choices that need to be made with question marks. The platform used is 500 nm Ge-on-SOI, so these values are known.

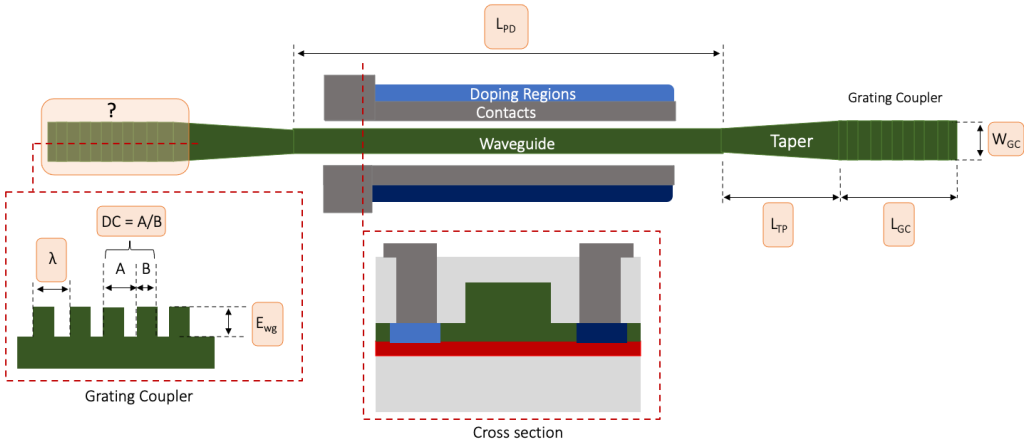

FIGURE 5.2: Diagram of the top down preliminary photodetector design. Showing dimension choices that need to be chosen for the grating coupler, waveguide and taper length. As well as showing a cross-sectional view.

- Waveguide width (W_{wg}) and etch depth (E_{rib}).

- Grating coupler length (L_{GC}) and width (W_{GC}), etch depth (E_{rib}), pitch (P_{GC}), and duty cycle (DC).
- Ohmic contacts distance from waveguide (S_m), width (W_m), material choice and contact pad width (W_c).
- Doping width (W_{PN}), depth and distance from waveguide (S_{PN}).
- Doping implantation parameters.
- Ion implantation parameters for the creation of defects.
- Length of detector (L_{PD}).

To find these parameters both simulations and literature were used, described in the next sections.

5.2 Optical Simulations

Optical simulations were performed using Lumerical software to calculate the optimal dimensions of the photodetectors waveguides and grating coupler. To investigate the spectral response of the detectors, at and beyond the bandgap of intrinsic germanium, the photodiodes would be designed to couple light for 8 wavelengths covering a span from 2 - 3.8 μm at: 1.95, 2.05, 2.3, 2.6, 2.9, 3.2, 3.5 and 3.8 μm. Therefore these simulations where performed and the optimal structure designs where found so that the photodetector could detect at each wavelength. The response at 2 and 3.8 μm are chosen as two ends of the range as 2 μm is where germanium becomes transparent so is useful to begin probing the responsivity of the photodiodes at this wavelength. The other end of the wavelength range is chosen to be 3.8 μm as a tuneable laser at this wavelength was easily accessible for characterising and is also a realistic maximum spectral range as other monolithic detectors have a measurable responsivity in the 3 - 4 μm wavelength range.

5.2.1 Lumerical Software

Lumerical software was used to simulate the propagation of light in the waveguides and grating couplers, Lumerical - Mode Solutions and Lumerical - FDTD, respectively (**?**) (88).

Lumerical FDTD uses a finite element method (FEM) for solving the propagation of light in structures, called Finite-difference time-domain (FDTD). The method works by dividing the structure into a 3D mesh composed of small cells called 'Yee Cells'. At each of these cells Maxwells Equations are solved to find the x, y and z components of the electric and magnetic fields. Lumerical Mode Solutions uses a Finite Difference Eigenmode Solver

which solves Maxwell's Equations across a cross-section of waveguide to provide the spatial profile of the mode and its frequency dependence. It includes a frequency sweep when solving so allows group delay and dispersion to be quickly found as well as the mode profile and loss. These software were used to choose the dimensions of grating couplers that would result in optimum coupling at the 8 wavelengths mentioned before as well as finding the dimensions of the waveguides that operated in single mode.

5.2.2 Grating Coupler Simulations

Light can be coupled from free-space into a waveguide using a grating coupler. The coupling efficiency of light into the waveguide depends on the pitch, duty cycle, etch depth of the grating, waveguide width and BOX thickness, properties of a grating coupler which are shown in Figure 5.3.

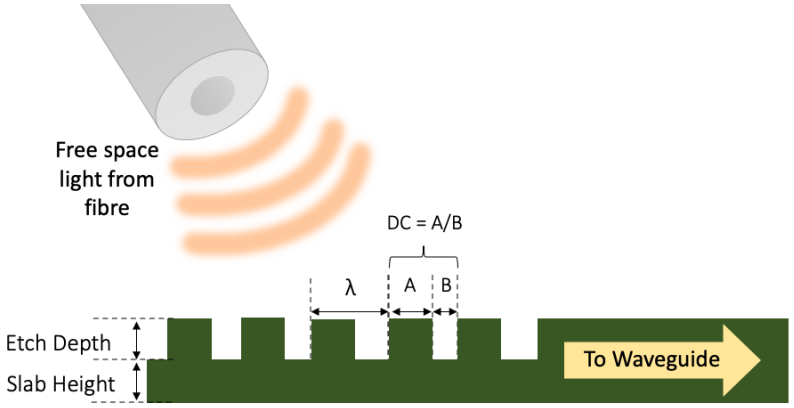

FIGURE 5.3: Light (red) is coupled from free-space into the waveguide via a grating coupler. Etch depth is how deep the grating teeth are etched down to. Duty cycle (DC) is the ratio of width of the etched to unetched areas. Pitch (λ) is the grating period.

To create functional grating couplers for the photoiodes, simulations were performed in Lumerical FDTD. Simulations were setup using a grating coupler structure with a Ge-on-SOI platform, which consists of 500 nm of germanium, 60nm of silicon, 3 μm of SiO_2 on a silicon substrate. The simulation used perfectly matched layer (PML) boundaries to absorb light once it reaches the boundaries. Transmission monitors were also placed below, above and behind the grating coupler to also monitor reflections and path of inserted light. The structure of the simulation used to design the grating couplers is shown on the top of Figure 5.5. The investigated properties (etch depth, duty cycle, pitch, optimum fibre angle and position above the grating coupler) are varied across a range of dimensions whilst monitoring the percentage of light coupled into the the waveguide, this will be referred to as the simulated coupling efficiency. Results from sweeping the DC and pitch and looking at the percentage of light coupled into the waveguide are shown in Figure 5.4.

The darker blue areas denote areas of high coupling, the efficiency is negative because of the direction of light through the monitor, as light traveling from right to left or from

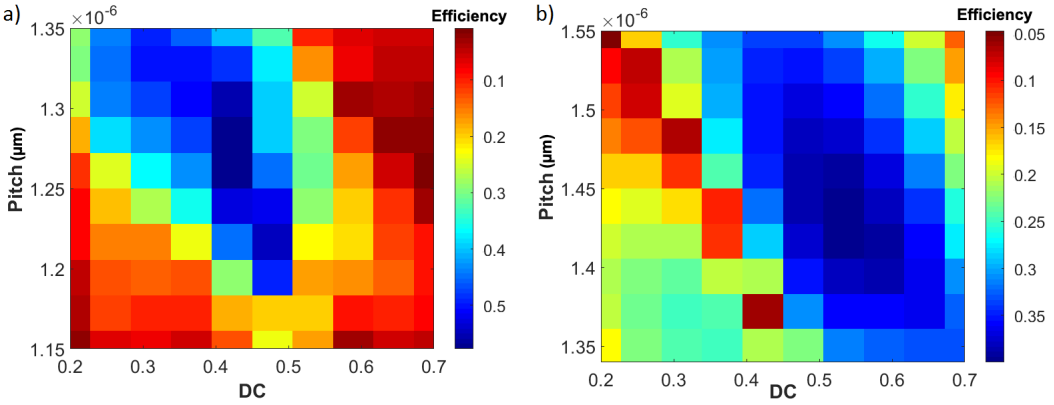

FIGURE 5.4: Results from simulations used to choose the optimum pitch and DC for coupling a) 1.95 μm light b) 3.8 μm light.

bottom to top are noted as negative. The combination of parameters that resulted in the most efficient grating coupler design are chosen, this process is repeated for the 8 wavelengths between 1.95 μm and 3.8 μm. A table of the simulated results used for designing the grating coupler are shown in Table 5.1.

Wavelength of input light (μm)	Duty cycle	Pitch (μm)	Grating coupler Width, W_{GC} (μm)	Simulated coupling efficiency (%)
3.80	0.5	1.45	20	39
3.50	0.5	1.31	18.75	43
3.20	0.5	1.18	17.5	52
2.90	0.5	1.03	16.25	47
2.60	0.5	0.885	15	38
2.30	0.5	0.755	13.75	46
2.05	0.4	1.35	12.5	51
1.95	0.4	1.25	11.25	50

TABLE 5.1: Chosen parameters for grating couplers that will couple different wavelengths of light

This simulation setup would result in functional grating couplers but not optimal. Simulations were performed after characterisations and improvements to the simulation involved using a smaller SiO_2 capping layer to correctly simulate the actual height of the fabricated capping layer, use a fibre to create the light source, using a mode expansion monitor to view the amount of light guided into the fundamental mode rather than measuring all light that passes the power monitor, a screenshot from both the old and improved simulation is shown in Figure 5.5.

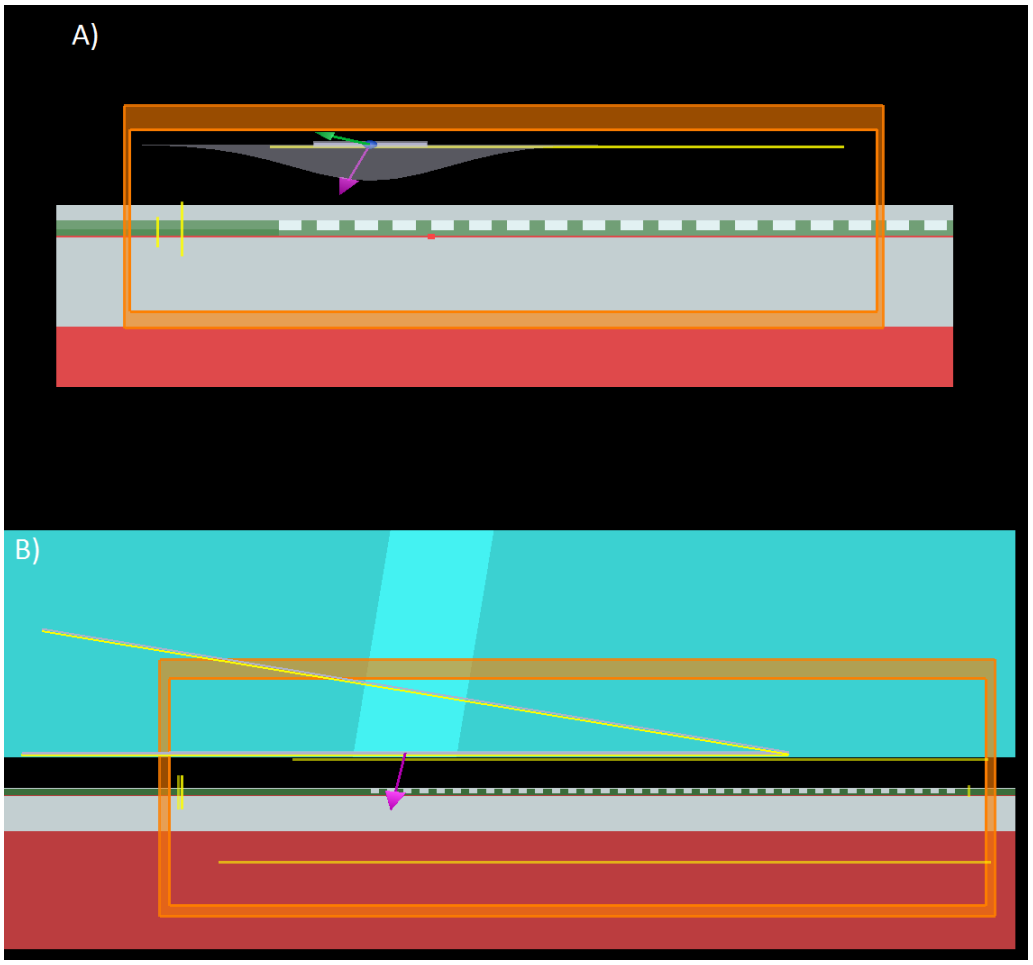

FIGURE 5.5: Screenshot from FDTD software. Blue structure shows the simulated fibre, the yellow angled line is an angled Guassian source of light. The red and grey structure is a longitudinal cross-section of the grating coupler and waveguide. Top - old simulation. Bottom - Improved simulation.

These improvements were applied to simulations of the measured dimensions of 1.95 and 3.8 μm grating couplers from microscope images in section, examples shown in Section 6.6. The pitch from the gratings was measured as designed although the DC of the devices measured was 0.45 and 0.53 for the 1.95 and 3.8 μm grating couplers respectively. This resulted in a change in peak efficiency in both couplers.

The changes in the simulation now show that the for the originally designed 1.95 μm gratin coupler, that the increase in DC but same pitch measurement resulted in the peak efficiency being shifted upwards towards 2 μm, see Figure 5.6. Other changes in the simulation also resulted in a lower simulated coupling efficiency than before, from 39 % to 25 %.

Similarly the results of using parameters from SEM images when calculating the grating coupler efficiency at 3.8 μm resulted in a change of simulated coupling efficiency from 39 % to 28 %, see Figure 5.7.

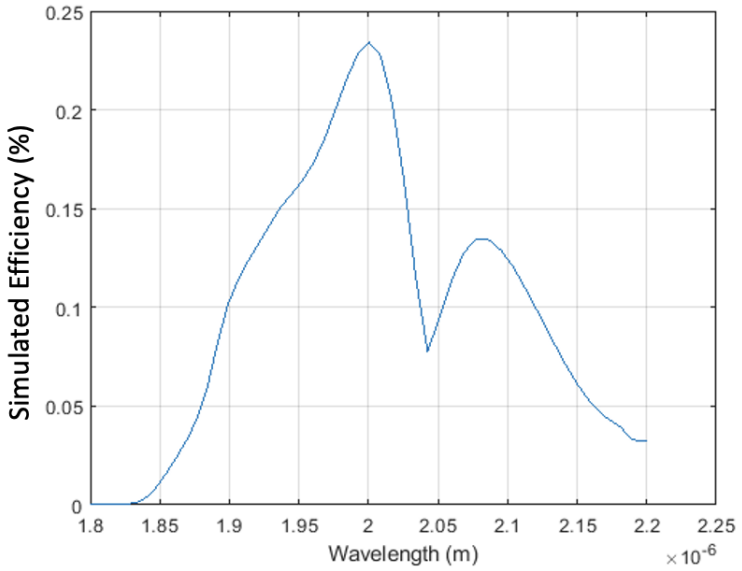

FIGURE 5.6: Simulation of grating coupler coupling efficiency of the grating coupler that was originally designed to optimally couple 1.95 μm light. Now couples less light and at a different peak wavelength than originally planned.

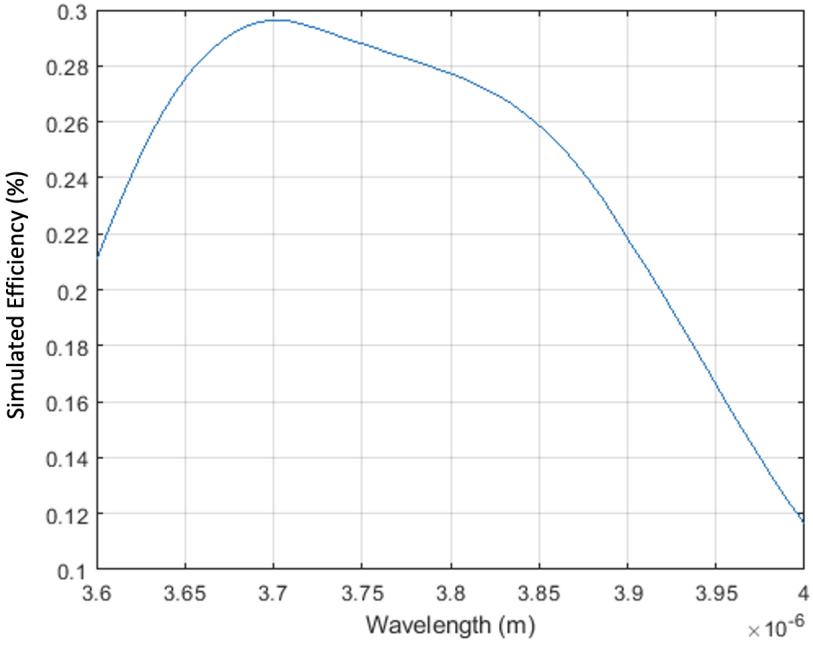

FIGURE 5.7: Simulation of grating coupler coupling efficiency of the grating coupler that was originally designed to optimally couple 3.8 μm light.

5.2.3 Waveguides

Simulations of the waveguide are performed using Lumerical Mode Solutions to find single mode operation at each of the wavelengths mentioned above, as well as the distance of the doping from the rib waveguide. While single mode operation is not necessary for a

photodiode, having only a single mode propagate allows the designs to be easily incorporated into an integrated photonic circuit as light is often guided in a single mode, so avoiding higher orders eliminates mode-mismatching loss.

As the detectors are fabricated on 500 nm of Ge-on-SOI, investigation of single mode operation began with 500 nm tall waveguides and an etch depth to match the grating couplers. If the height of the germanium could remain unaltered at 500 nm and the etch depth the same as the grating couplers of 330 nm it would benefit fabrication because it would require less fabrication steps, meaning less room for errors. This leaves the width of the waveguide as the only variable, a parameter which can strongly affect the number of modes that propagate through the waveguide.

To begin simulating, a rib waveguide structure of a 500 nm rib and 170 nm tall slab was created with a 60 nm Si layer, 3 μm 1 oxide layer and a silicon substrate added at the bottom, a 1 μm SiO_2 cladding layer is placed on the waveguide. The width of the rib is swept over a range of widths and simulated to look for modes present and their effective refractive indexes. When designing the waveguides, the simulation was setup with the metal boundaries and the size of the boundary was increased until it no longer affected the effective index of the simulated mode. Single mode operation is found by sweeping the waveguide width and plotting it against the effective index of modes present. When the width was just small enough to support one mode, meaning only one TE and TM mode have an effective index larger than the effective refractive index (N_{eff}) of slab, this was deemed single moded.

When checking the simulations post fabrication and characterisation, improvements to the simulation were made which changed the resulting guided modes. Improvements to the simulation included: matching the SiO_2 cladding to the waveguide geometery, changing the SiO_2 cladding to match the fabricated thickness and increasing the amount of modes searched for. A comparison of the old and new simulation setup is shown in Figure 5.8.

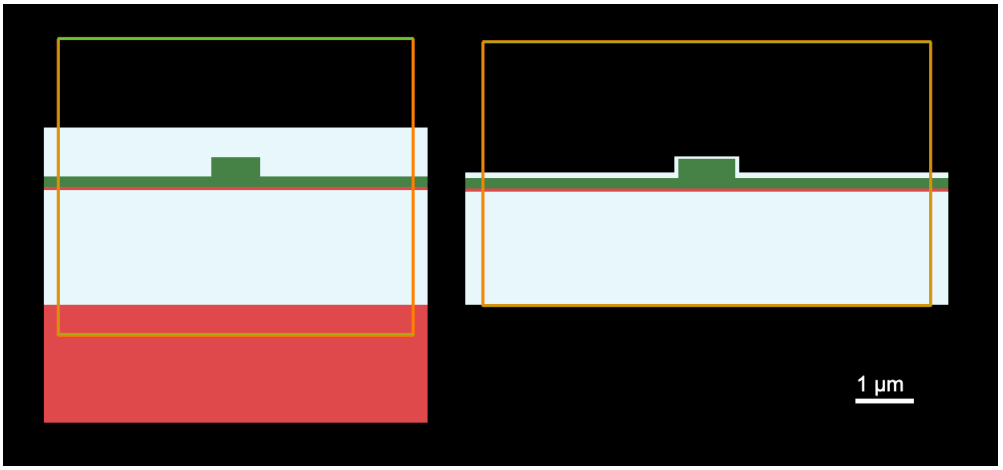

FIGURE 5.8: Left - the first design simulation structure. Right - improved design simulation structure.

A graph showing the swept waveguide width from both the old and new design is shown in Figure 5.10. These improvements resulted in a guided TE mode being found that was not before as the simulation only looked for 4 modes and would prioritise the fundamental in the waveguide and modes in the silicon substrate, an image of the two TE modes is shown in Figure 5.9. This can be seen as the N_{eff} of the slab and silicon substrate at this wavelength is 2.405 and 2.938 respectively.

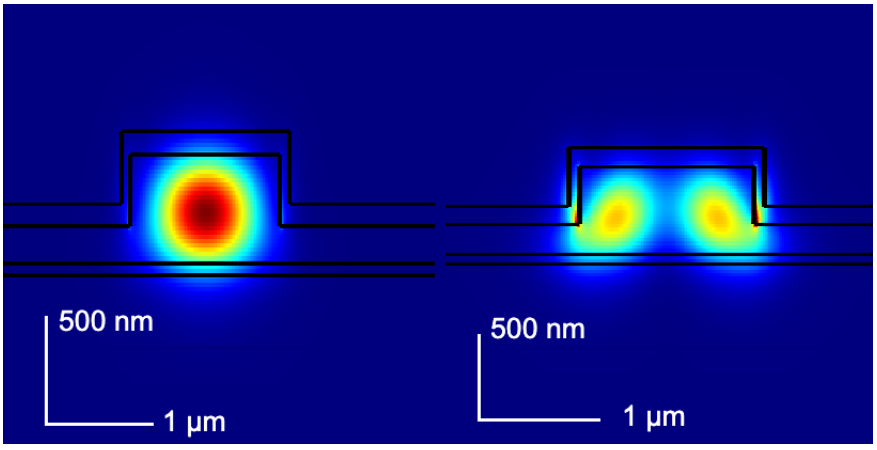

FIGURE 5.9: Screenshot from Mode Solutions Software showing two TE modes both of 3.8 μm light in a 1.4 μm wide waveguide. Left is the fundemental TE mode and the right is the second TE mode.

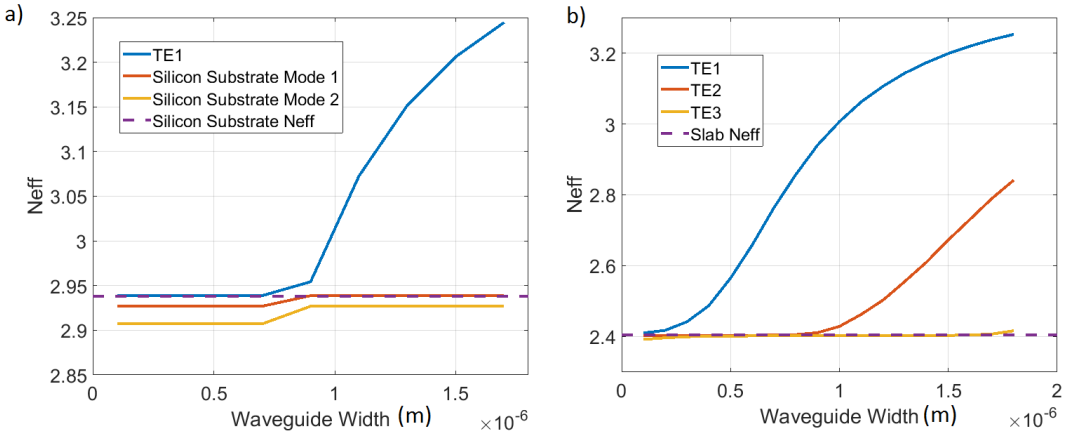

FIGURE 5.10: Sweeping the wavequide width and plotting the N_{eff} of modes at a wavelength of 3.8 μm.

The fabricated waveguide widths with the old design which was used to create the photodetectors and improved simulated single mode widths are compiled in the Table 5.2. A compilation of the N_{eff} versus waveguide widths for different wavelengths of input light is shown in Figure 5.11

To prevent free-carrier absorption the doping regions are kept at a distance to minimise overlap whilst also staying close enough to keep bandwidth high and reduce the recombination of carriers before reaching the doped region. The distance of the N and P doping was chosen by looking at the distance chosen in silicon defect mediated detectors

Single mode conditions			
Wavelength (μm)	Waveguide width (μm)	Improved Waveguide Width (μm)	Junction distance from rib edge (μm)
3.80	1.4	0.8	1.4
3.50	1.3	0.7	1.3
3.20	1.2	0.5	1.2
2.90	1.1	0.5	1.1
2.60	1.0	0.4	1.0
2.30	0.8	0.3	0.8
2.05	0.7	0.3	0.7
1.95	0.7	0.3	0.7

TABLE 5.2: All waveguides above have a height and etch depth of 500 nm and 330 nm respectively

which was often comparable to the waveguide width. For each photodiode designed in this thesis the chosen seperation distance between rib waveguide and doped regions was the width of the waveguide.

5.3 Implantation Simulations

5.3.1 P++ and N++ Implantation Simulation

The implantation simulations performed, involved the simulation of physically implanting the ions and getting information of implantation depth and concentration. Electrical simulations were not performed as defect characteristics are unknown and the creation of a PN junction in germanium is standard.

The doping concentration of operational waveguide integrated germanium photodiodes were noted from literature at $1x10^{20}$ ions/cm^3 (29). Therefore simulations were performed using this detectors dimensions to target this same level of doping concentration at the surface of germanium. This high concentration of dopants reduces the resistance between the Ohmic contact and doped region, which is desirable for high speed operation. Simulations were performed in a software called TRIM (the Transport of Ions in Matter) and Silvaco (89) (90).

TRIM, where the stopping range of implanted elements is found is a Monte Carlo simulation. A target material can be made up of defined layers of elemental or compound materials. With the implantation of an element chosen and tilt and energy defined, the

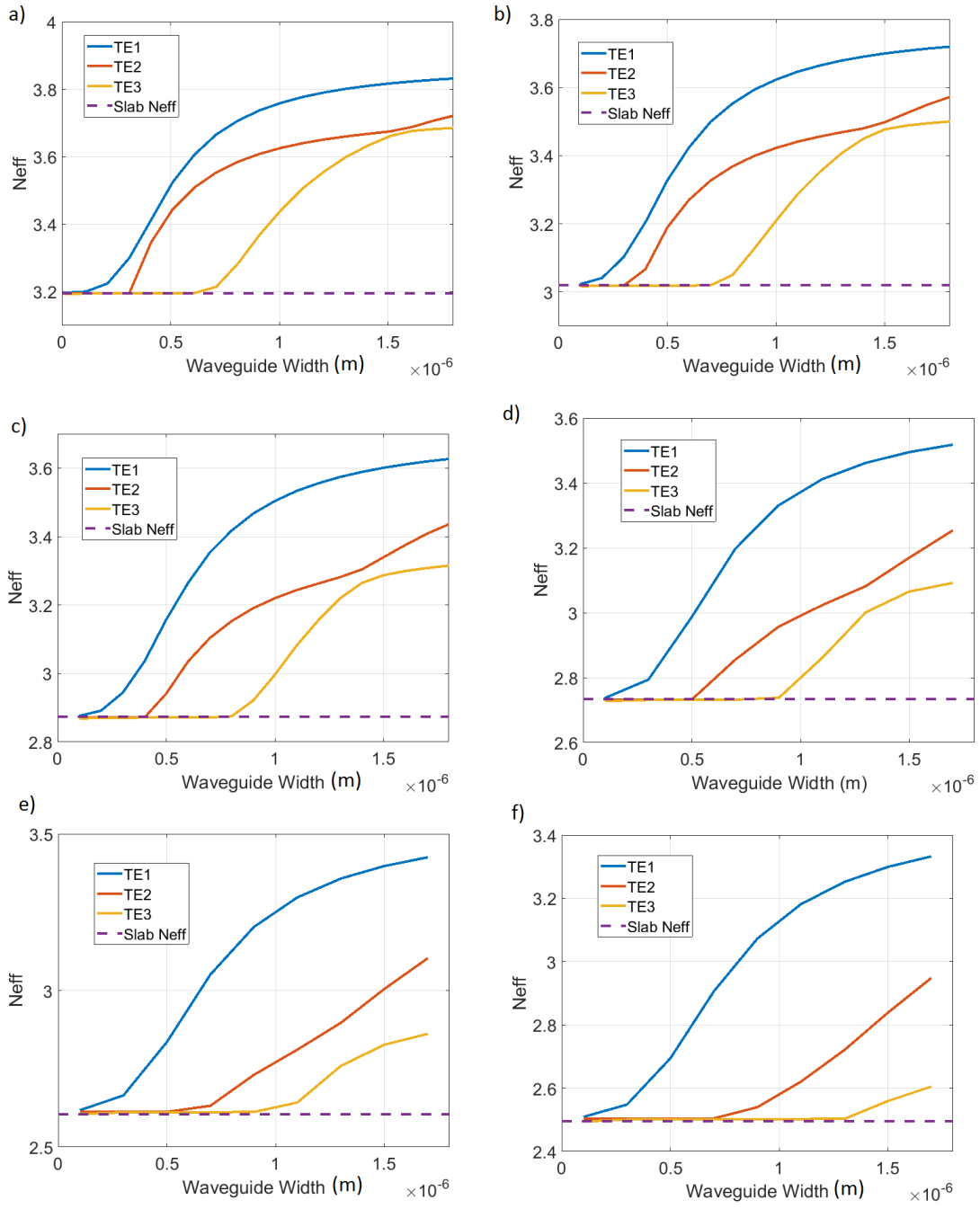

FIGURE 5.11: Graphs of waveguide width versus N_{eff} of modes present at wavelengths a) 2.0 μm b) 2.3 μm c) 2.6 μm d) 2.9 μm e) 3.2 μm f) 3.5 μm.

cascade of individual atoms begin. Each cascade can be followed but in this case it is more important to see the behaviour over many atoms.

Silvaco is a software used to simulate the process of fabrication, e.g., material deposition, annealing, etching. In this case it is used to double check the implantation. The same target material stack, implanation energy and tilt angle is used as in the TRIM simulation.

The images below show the implantation of P and BF_2, see Figure 5.12 and Figure 5.13. For the implanation of BF_2 the simulation was only performed in silvaco as TRIM can only implant elements. A layer of SiO_2 is included in the simulation since a capping layer of SiO_2 will be deposited during fabrication prior to implantation.

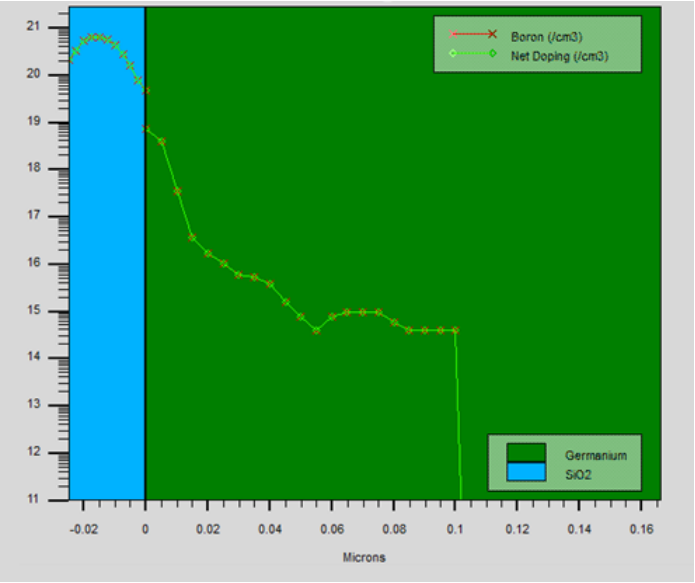

FIGURE 5.12: Screenshot of results from Silvaco for BF2 doping.

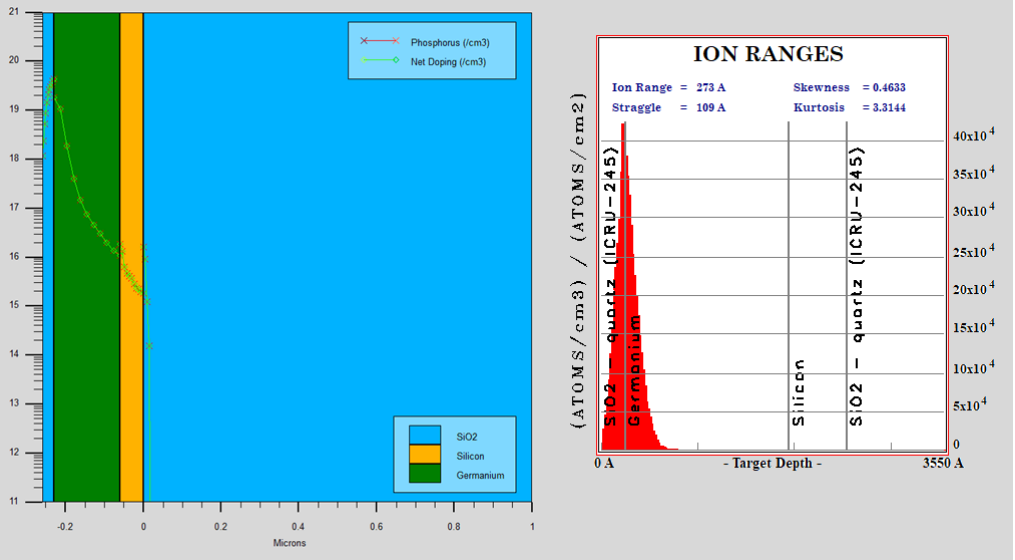

FIGURE 5.13: Screenshot from Silvaco for P doping. The silvaco simulation results are shown on the left and the TRIM results are shown on the right.

The final implantation parameters chosen from simulations are shown in Table 5.3.

5.3.2 Defect Ion Implantation Simulation

Boron and germanium were chosen as the first ions to implant to create defects. This is based off the successful results of using boron and silicon ions in defect mediated silicon

Doping implantation parameters					
Doping ion	Energy (KeV)	Fluence (ions/cm^2)	Simulated concentration (ions/cm^3)	Current (μA)	Tilt Angle
BF_2	40	1x10^{15}	1E19	10	7°
P	220	1x10^{15}	2E19	20	7°

TABLE 5.3: Parameters chosen for doping performed at the University of Surrey Ion Beam Centre.

detectors to create divacancies and self interstitial clusters (65). Boron was implanted first and chosen to implant at fluences 1x10^{10}, 1x10^{12}, 1x10^{14} ions/cm^2 which covers a wide range of fluences that were used as an implantation doses in silicon, e.g., implantation of 1x10^{13} of boron in silicon (2), 1x10^{12} of silicon in silicon(65) and both 1x10^{12} and 1x10^{13} of zinc in silicon (52).

After the implantation of boron, the successful application to the RADIATE project allowed for more ion beam implantation time. The project was aimed at developing partnership between ion beam facilities and research groups across different countries in Europe. The partnership was with ETH Zurich and allowed more ions to be chosen for investigation

Germanium ions were also chosen for self implantation but at lower doses. It was known at this point because characterisation of the photodiodes that used boron to create defects that the higher implantation dose of 1x10^{14} ions/cm^2 was detrimental to responsivity using boron ions and this also follows the doses from self-ion-implanted silicon detectors (65).

Heavy metal ions have been used to create subband photodetectors in silicon (52) (58). Heavier metal ions, gold, mercury and copper were chosen to create defects as they are known to create subband levels in germanium.

Simulations for the chosen ions where performed in TRIM and Silvaco using the same procedure as before for PIN doping. A table of the selected ions and their implantation parameters are shown in Table 5.4.

5.4 Photodiode Final Design and Chip Layout

5.4.1 Device design

While simulations allowed the majority of design decisions to be made other decisions were made as follows:

Ions, energies and fluences used to create defects		
Implant ion	Energy (MeV)	Fluence (ions/cm^3)
B	0.070	1x10^{10} , 1x10^{12} , 1x10^{14}
Ge	0.750	1x10^{10} , 1x10^{11} , 1x10^{12}
Au	2	1x10^{10} , 1x10^{11} , 1x10^{12}
Hg	2.2	1x10^{10} , 1x10^{11}, 1x10^{12}
Cu	0.650	1x10^{10}, 1x10^{11} , 1x10^{12}

TABLE 5.4: All implants are implanted with a 7 degree tilt and the ETH Zurich implants a 22 degree twist angle

- Grating coupler width - Chosen to match the diameter of mode exiting the fibres being used in experiments.
- Waveguide length - Chosen to be 4 mm for all photodiodes. While increasing the photodiode length would also increase dark current it also allows for a longer interaction length between the light and defects. Silicon defect mediated detectors used lengths such as 6 mm (65), 5 mm (67), 3 mm (91) (92) and 2.5 mm (2). A length towards the longer end of this range was chosen to maximise the chance that a signal is detected, as this fabrication run is aimed at finding defects that produce a MIR response.
- Ohmic contact material layers - Was informed by Dr Lorenzo Mastronardi who had successfully used this recipe to create active germanium devices. The first layer of Ni was deposited to form GeNi which reduces contact resistance, Ti was deposited after to avoid metal diffusion and separate the Ni from the bulk Al layer which was covered in Ti again to protect the surface (93).
- Ohmic contact pad size - By looking at the pitch of RF probes available in our labs already, the pitch between the contact pads were chosen. The width of the square pads were chosen to be larger than the probes.
- (S_m) Distance between germanium rib edge and edge of metal vias -

The final device design for a completed photodiode is shown as a cross-section in Figure 5.14 and from a top-down view in Figure 5.15.

5.4.2 Mask Design

With the simulations performed and design finalised; a digital mask layout must be drawn for use in lithography. The mask layout was drawn digitally in a software called Tanner's

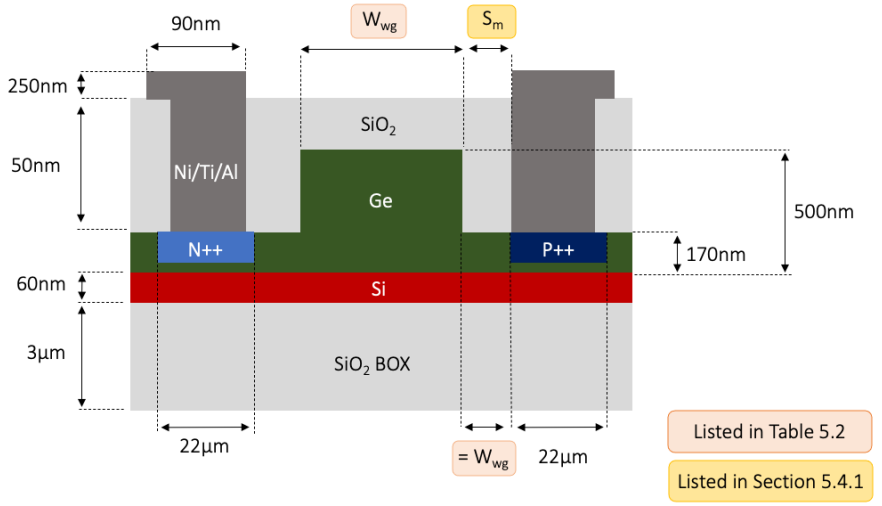

FIGURE 5.14: Diagram showing the top down preliminary design. Showing dimension choices that need to be made for grating coupler. The various values for waveguide width are listed in Table. 5.2.

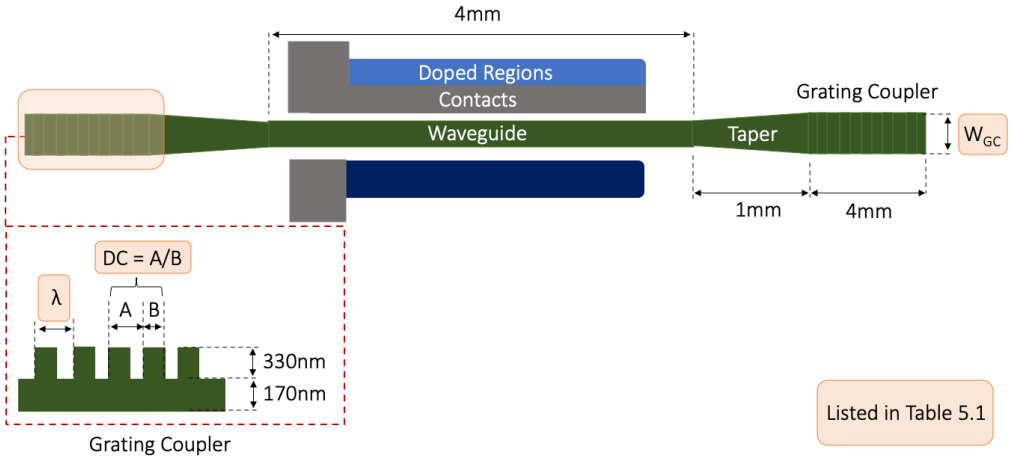

FIGURE 5.15: Diagram showing the top down preliminary design. Showing dimension choices that need to be made for the grating coupler. The various values for waveguide width are listed in Table. 5.1.

L-Edit (94). The mask was drawn using functions written in C++ that would be used to draw components like grating couplers, waveguides, tapers. The functions contained variables for parameters on the devices. i.e length of waveguide, period of grating coupler etc. A complete photodiode layout would be created by using these functions in series.

5.4.3 Chip Layout

The complete chip layout is designed to group variants of the diode logically so specific devices can be found easily. The chip separates the completed diodes and test structures onto each half of the chip, shown below in the L-edit mask layout in Figure 5.16.

The half with the completed diodes are then made up of 8 groups of detectors, these are visually distinguished on chip by an indent at each group. Each of these groups are designed to couple different wavelengths of light from 1.95 μm to 3.8μm through their optimised waveguide and grating coupler designs, the different parameters of which are described earlier in this chapter in Table 5.2 and Table 5.1. Within each of these 8 wavelength specific groups are 6 photodiodes, each of which are have been implanted along the length of the waveguide at different lengths: 0 mm, 0.85 mm, 1.70 mm, 2.55 mm, 3.2 mm and, the full length of the diode, 4 mm. These subgroups allow the spectral response and the effect of the amount of defects on the photodiode to be investigated.

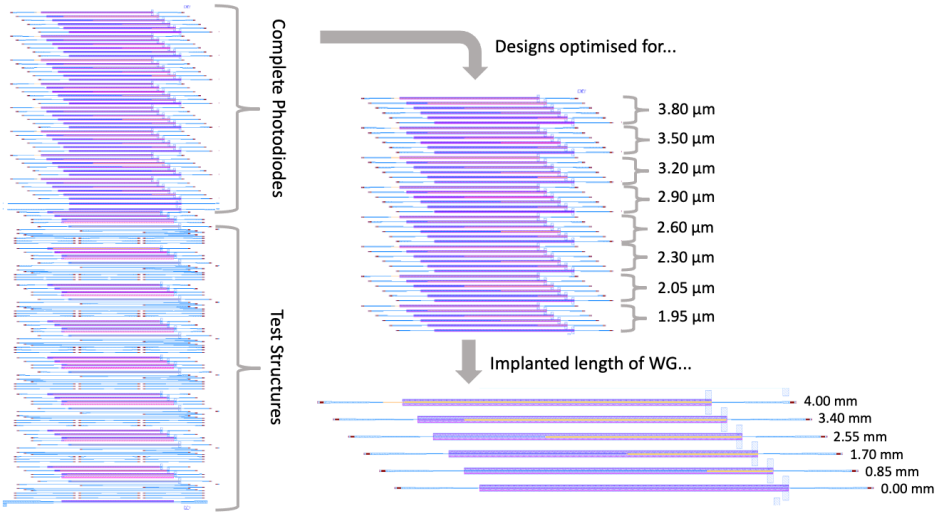

FIGURE 5.16: Completed chip layout in L-edit. Showing how the chip is divided into test structures and diodes, then divided by wavelength dependance and finally their total implanted length.

The other half of the chip containing test structures are similarly divided into 8 groups where the devices are designed to couple light from 1.95 μm to 3.8 μm, see Figure 5.17. Within each of these groups there are a number of different devices used to probe variants and help characterise the final design at that wavelength. Figure 5.17 shows what the structures in each group are designed to investigate:

Red group: This group has variations on the final photdiode design. There is a device without metal contacts and three other diodes to investigate the effect of varying the distance between the rib waveguide and doping regions. One diode with the designed distance and another two, one larger and another one smaller by 100 nm.

Green group: This group contains three straight waveguides for measuring propagation loss at the wavelength of the group. It contains a 4 mm long waveguide, a 2 mm long waveguide and a structure with no waveguide, only the grating couplers connected to each other.

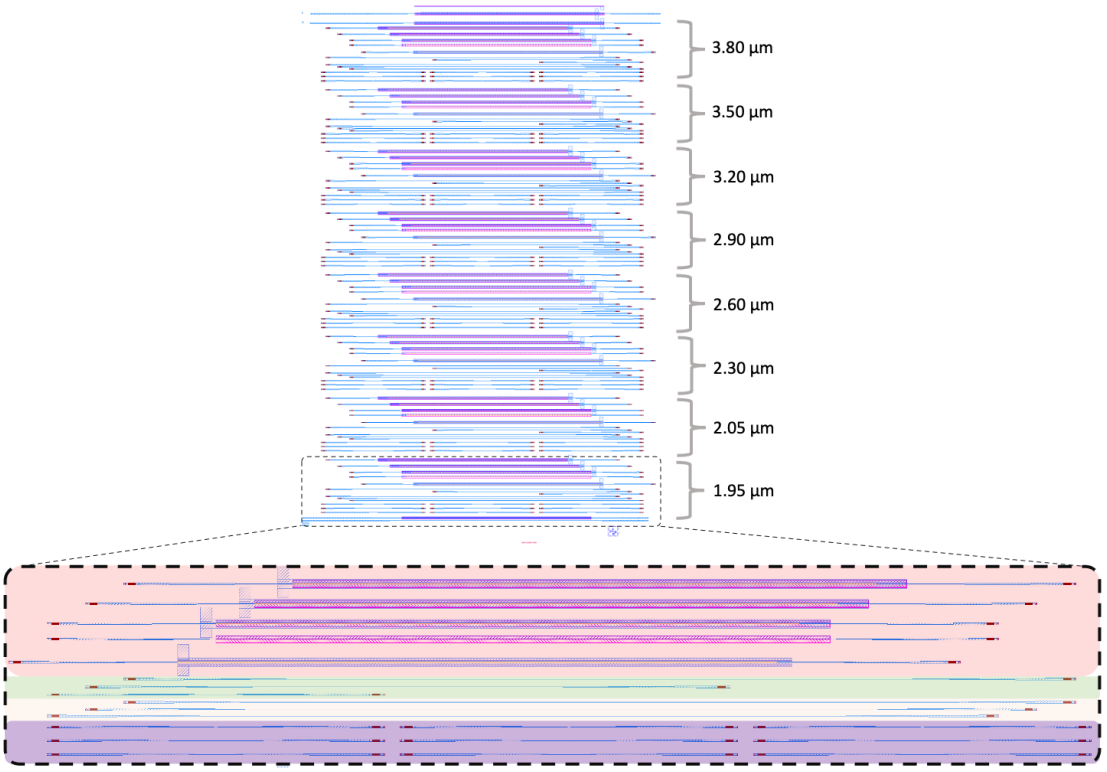

FIGURE 5.17: Image of the chip layout in L-edit of the test structures. These structures are divided into the wavelengths they can couple. The highlighted section shows the tests tructures in more detail and is explained below.

Yellow group: This group contains three 4 mm long waveguides for propagation loss measurements.

Blue group: There are 9 structures that are composed of two joint grating couplers. The central structure has the same grating coupler design as the final photodiodes of the same wavelength design and the other 8 surrounding it have variations in the pitch and duty cycle to investigate which design resulted in the most efficient transmission.

5.4.4 Wafer Layout

The final chip design described above was fabricated on a two 6 inch wafer and repeated on a 3 x 14 grid with the final step, ion implantation to create defects, differing from chip to chip, shown in Figure 5.18. This allowed the investigation of ion implantation parameters listed above in Table. 5.3 and Table 5.4.

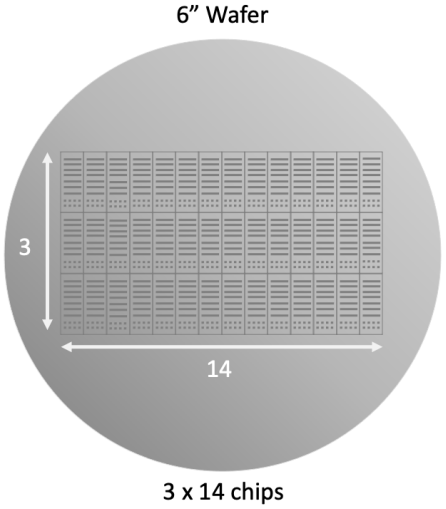

FIGURE 5.18: Illustration of one the final wafers, showing the repeated chip design that was desribed above. Having this many chips allowed for variations in ions and their dose to be investigated.

5.5 Summary

This chapter gave a description of the design process for the photodiode. This was to select dimensions for a rib waveguide PIN photodiode on a germanium on SOI platform.

The dimensions for the detectors optical guiding components, grating couplers and waveguides, were simulated using Lumerical software. Simulations were first performed to find suitable single mode waveguide conditions, later improved simulations found that the chosen waveguide dimensions were actually multimoded and suggested new single mode waveguide dimensions. The grating coupler simulations were performed after to find the most efficient design in coupling free-space light into a waveguide. The simulations performed to find grating couplers that could operate over 1.95 - 3.8 μm found designs with efficiencies of between 38 and 51 %. These simulations were performed again with improvements using the fabricated dimensions and found efficiencies of X and Y % for the grating couplers designed for operation at X and Y μm respectively.

Literature informed the choice of ions to create defects and through the use of TRIM and Silvaco, simulations were also performed to find the ion implantation paramenters for the P and N doped regions as well as for implantating ions to create defects. The remaining device parameters such as the grating coupler width, waveguide length, Ohmnic contact material layers and contact pad size were chosen through literature.

With the device parameters described the chapter then went on to describe the mask design, in terms of the layout of devices on each chip and how each chip is used to investigate the implantation of different ions to create defects and the effect of different implantation doses.

Chapter 6

Fabrication

This chapter describes the fabrication steps performed in creating the germanium photodiodes for this project. Fabrication of the devices was performed by myself, Ali Khohar who performed E-beam lithography and Wei Cao who helped performing rapid thermal annealing (RTA). Ion implantation was performed at the University of Surrey Ion Beam Centre and Zurich ETH.

6.1 Step 1: Creating the Wafers

Fabrication of the detectors was performed on two 6″ germanium on SOI wafers, allowing the creation of many devices which would allow more ion implantation parameters to investigated. Using two wafers also provides a backup in the event a wafer is irreparably damaged during fabrication. The wafers used are the same as those used in a paper by A. Osman *et al.*, involving the creation of a suspended MIR germanium waveguide (13). To create the germanium on SOI wafers, a 220 nm Si on 3 μm SiO_2 SOI wafer (manufactured by SIMGUI) (95), was firstly thinned to 60nm by wet oxidation through dry oxidation for 26 hours at 1000° C, the resulting 430 nm of formed SiO_2 was then wet etched with a 7:1 dilution of hydrofluoric acid. This silicon layer acted as a seed layer for subsequent germanium growth. The growth of 500 nm of germanium was performed using reduced pressure chemical vapor deposition (RPCVD) by semiconductor componany, IQE.

6.2 Step 2: Creating Waveguides and Grating Couplers

The waveguides and grating couplers were created in the same lithography step as they had both been designed with a 330 nm etch to reduce the number of fabrication steps. An overview of the lithography process is described in section 3.1.2. To prepare for E-beam resist spinning, the wafers were put in a 210 °C oven and left for at least 2 hours at a time

to dehydrate the wafer, this was done before each E-beam resist spinning step, including those following in this chapter. E-beam resist ZEP520 was spun on the wafers to the thickness of 500 nm. Following that, ESPACER was also spun on the wafers to an unspecified thickness that covers the surface of the wafer, ESPACER is a highly conductive compound that allows charge to dissipate during the E-beam writing stage which could result in pattern placement errors if ESPACER was not used. E-beam lithography was performed using a 'Jeol JBX 9300 E-beam writing system'. Once complete, the ESPACER was washed off with deionised water (DI) and the wafers were placed in ZEDN50 for 2 minutes 15 seconds and gentely shaken to develop the ZEP, then placed in isopropyl alcohol (IPA) for 30 seconds to clean the wafers. Once developed, the wafers were dry etched by RIE-ICP using a Plasmalab 80 plus, the process of which is described in section 3.3.1. The etching was performed in multiple stages to try etch as accurately to 170 nm slab thickness as possible although in the likely event that the desired etch depth was not reached precisely, simulations were performed to ensure there was not an order of magnitude change in coupling efficiency in the event of over or under etching by 20 nm. The depth was measured after each etch stage with ellipsometry using a Woollham M2000D Ellipsometer which gave an estimate of the etch rate. Once the wafers were etched by 330 nm and the remaining E-beam resist was removed, a cap of 25 nm thick SiO_2 was deposited by PECVD using a OPT Plasmalab System 100 liquid source PECVD, to prevent the growth of native Ge oxide. The process of PECVD is described in section 3.2.1. A cross-section of the photodetector rib waveguide region after the completion of these processes is shown in Figure 6.1.

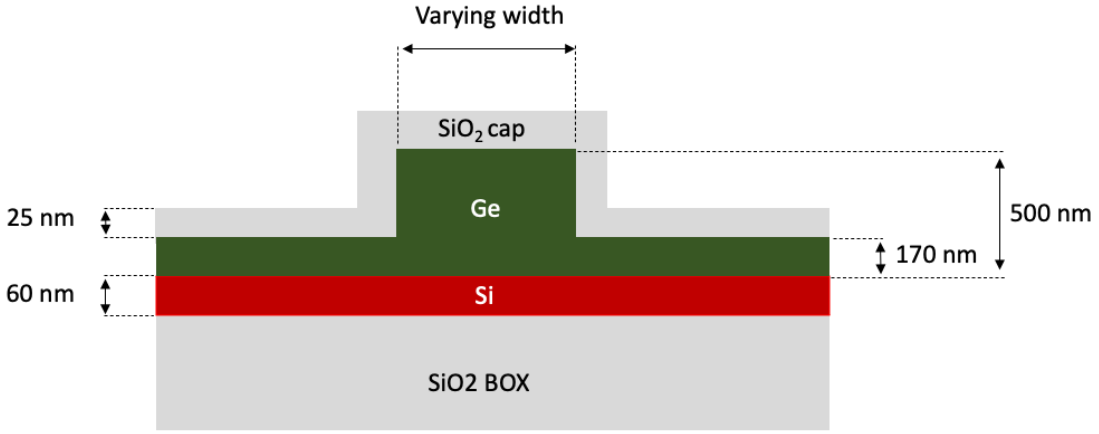

FIGURE 6.1: Diagram of the rib waveguides after the lithography and etching along with the parameters at this stage. A thin layer of SiO_2 is on top.

6.3 Step 3: P and N Doping

The next step is to add regions of P++ and N++ doping. To prepare the wafers for lithography that will pattern the wafers with doping windows; the wafers were spin coated with 600 nm of ZEP650K and ESPACER and the windows were written using the E-beam. After being irradiated the ESPACER was again washed off with DI water and the resist developed in ZEDN50 for 2.5 minutes and IPA for 1.5 minutes. This lithography step resulted in one window that will allow one side of the rib waveguide to be exposed to P++ type doping. The doping was added to the wafers using ion implantation, the process of which is described in section 3.3.3. The wafers were sent to the University of Surrey Ion Beam Centre as the University of Southampton cleanroom does not have ion implantation capabilities. The wafers were implanted with BF2 at an energy of 40 keV, a dose of 1E15 ions/cm^2, a 20 μA current and a 7° tilt to achieve a simulated concentration of 1E20 ions/cm^3 at the germanium surface. Once the P doping was completed and the wafers were sent back to Southampton, the E-beam resist was removed in an O_2 plasma.

The same process is performed again to create windows for the implantion N doping. To prepare for lithography, another 600 nm of ZEP650K and ESPACER were spun onto the wafers. The wafers were then exposed to E-beam radiation and again developed to reveal windows on the other side of the rib waveguide. The N doped regions are targeted to reach a similar concentration as the P doped region and to achieve this, the wafers were implanted with phosphorus ions at 20 keV with a dose of 1E15 ions/cm^2, at a current 10 μA and a tilt of 7 °. After this, similarly to the P doping, the E-beam resist was removed again using the plasma asher. The damaged SiO_2 was then removed via wet etch using 20:1 HF for 30 seconds and a new SiO_2 cap was deposited at a thickness of 50 nm using PECVD. RTA was performed at 600 °C for 2 minutes using a 'Jipelec Jetfirst 200 Rapid Thermal Annealer' to activate the dopants and afterwards, a second anneal was performed at 300 °C to help passivate the surface of the germanium. Another 50 nm of SiO_2 was deposited at this stage to protect the wafers from the metal deposition step that followed. The device cross-section is shown in Figure 6.2, showing the new SiO_2 cap and doped regions.

6.4 Step 4: Creating Ohmic Contacts

To create the metal vias, lithography was performed again to create windows in E-beam resist to allow the etching of germanium to create metal vias. ZEP and ESPACER was spun onto the wafers, E-beam lithography was performed and then the resist developed with ZEDN50 and IPA. To etch the metal vias SiO_2 was etched in the RIE-ICP and the ZEP was then removed in the plasma asher. When creating the Ohmic contacts, to allow the deposited metal to be easily removed from the wafers, a double layer resist of PMMA/MMA was spun onto the wafers as a E-beam resist. First 200 nm MMA was spun

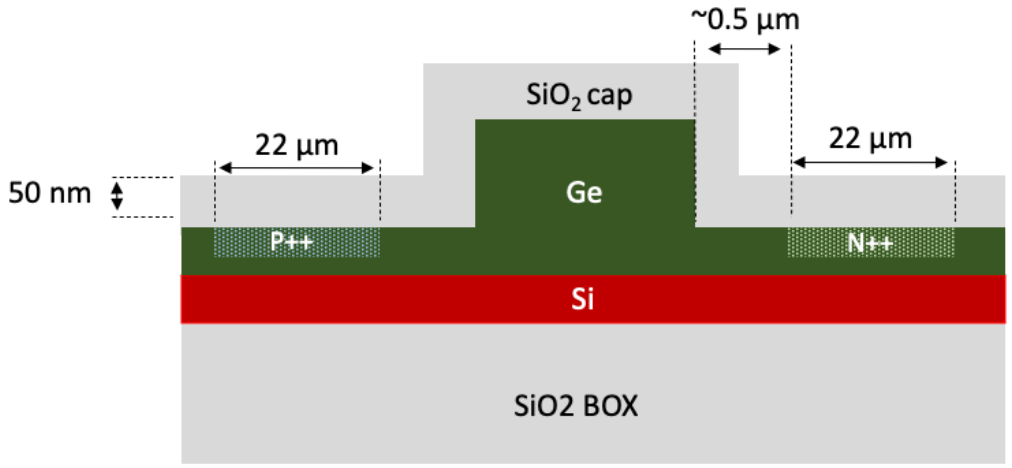

FIGURE 6.2: Cross-section of the device after P and N doping, a larger capping layer of SiO_2 is also deposited.

at a RPM of 2.5K and then baked at 150 °C for 2 minutes then 150 nm PMMA was spun at 6K after and baked at 180 °C for 2 minutes. E-beam lithography again was used and the resist developed in a 1:1 mix of IPA and MIBK (methyl isobutyl ketone). Following the development, an O_2 descum recipe was performed in the RIE-ICP and a quick 2-5 second rinse of 20:1 HF. This allows a clean contact of metal with germanium before a native oxide forms. Metal evaporation was performed using the 'Leybold Lab 700 e-gun evaporator' to deposit 30 nm thickness of Ni, 10 nm thickness of Ti, 200 nm thickness of Al and 60 nm thickness of Ti. The process of metal evaporation is described in section 3.2.2. Once removed from the evaporator the wafers were left in containers of in NMP (1-methyl-2-pyrrolidinone) for 2 days to allow PMMA/MMA to fully lift off. When most of the metal had lifted off the wafers were cleaned using IPA. A cross-section of the device at this stage is shown in Figure 6.3.

6.5 Step 5: Defect Implantation

As the chips are not designed with alignment marks on them, lithography can only be performed on the wafer scale. Thick 900 nm ZEP was spun on one of the wafers and a final E-beam lithography step was drawn to reveal the implantation windows on the diodes. To prepare multiple chips for implantation, the wafers need to be diced into separate chips, which would require a layer of S1813 to protect the wafer from saw dust.

To test covering a wafer with ZEP and S1813, they where both spun on test chips first. The temperature and time of the baking were varied between room temp and 70 °C. However all of these tests failed, with all of the tests resulting in cracked or sticky S1813. Thus, to divide the wafer, the wafer was cleaved instead of diced, sacrificing some chips as shown

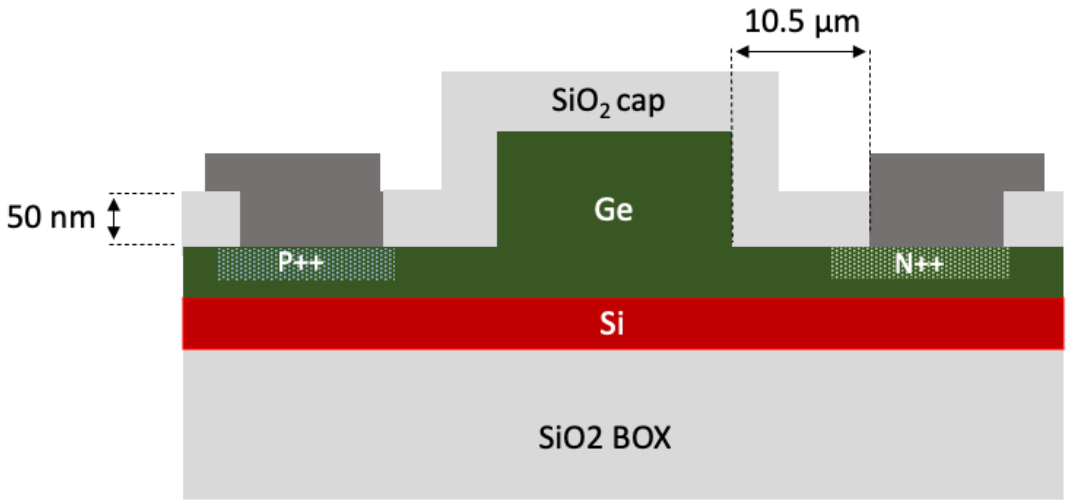

FIGURE 6.3: Cross-section of the device after the creation of metal vias and deposited metal contacts.

in Figure 6.4. The wafer was cleaved into groups of 2-3 chips. Each of the cleaved segments contained 3-4 chips, except for a small piece at the end that was left unimplanted to compare implanted chips against. The other parts were sent to the Ion Beam Centre in Surrey and implanted at a dose of $1x10^{10}$, $1x10^{12}$ or $1x10^{14}$ ions/cm^2 with boron ions at an energy of 70 keV at a current of 10 μA. Once implanted and returned the chips were placed in a anisole for 5 minutes with gentle shaking to remove the thick E-beam resist. S1813 was spun on top at 3k RPM to protect the surface of the chip from dust created during the dice, the S1813 was baked at 110 °C. The 3 implanted pieces were diced into smaller, 0.75 x 1.8 mm chips. Finally, the S1813 was removed from each individual chip and they were ready to be characterised, see Figure 6.5 for the final device cross-section.

After the completed fabrication of the boron implanted devices, more chips were cleaved from the wafer to implant with ions and doses as detailed in 5.4. The chips were coated with 900 nm of ZEP and sent to Zurich to receive implantation. Each ion and fluence combination was performed on one chip where as multiple chips were exposed to a specific dose of the boron implantation.

No chips were exposed to annealing after the final stage implantations. This would allow the chips to be characterised first and annealed after so that an investigation of the optimal annealing temperature can be found.

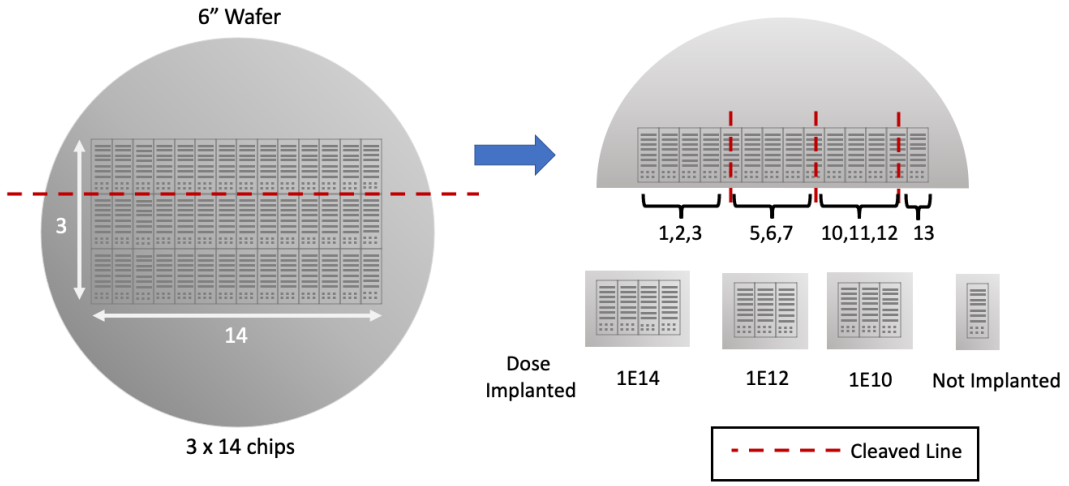

FIGURE 6.4: A diagram showing the wafer layout and the cleave line locations and the resulting chips that where exposed to each dose of boron implantation.

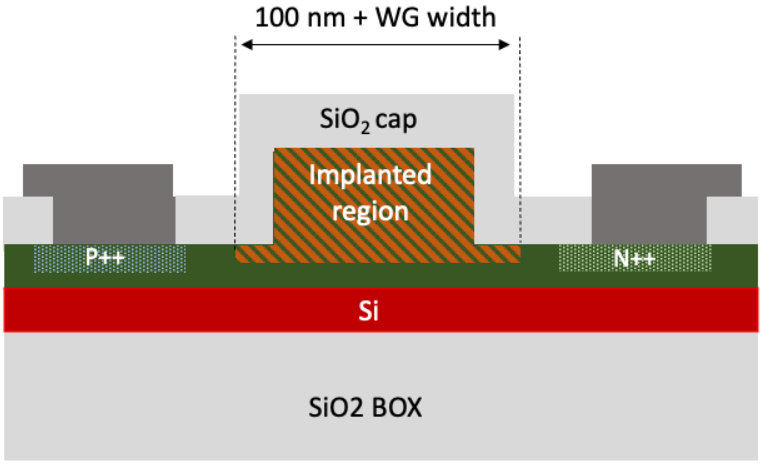

[h!]

FIGURE 6.5: Final cross-section of device, showing the area of the device implanted with chosen ions to create defects.

6.6 SEM Images

Once the fabrication was complete, scanning electron microscope (SEM) images of the detectors were captured, see Figure 6.6, Figure 6.7, Figure 6.8. These images show that the fabrication was successful.

In Figure 6.6, this SEM image shows the cross-section of a photodiode designed for 3.8 μm operation with a 1.4 μm wide waveguide. The doped regions are shown in red and blue.

From this image the thin 60 nm Si seed layer is visible.

In Figure 6.7, this SEM image shows Ohmic contact pads with a waveguide running through. The 5 μm bias etched region around the waveguide to create the rib structure is visable as well as an adjacent photodiode.

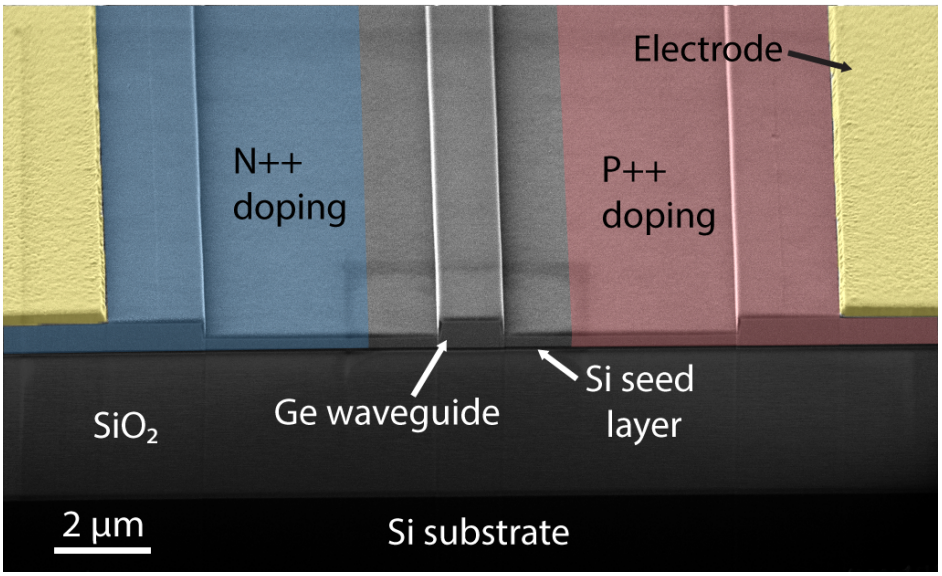

FIGURE 6.6: Image of the cross-section of a 3.8 μm photodiode.

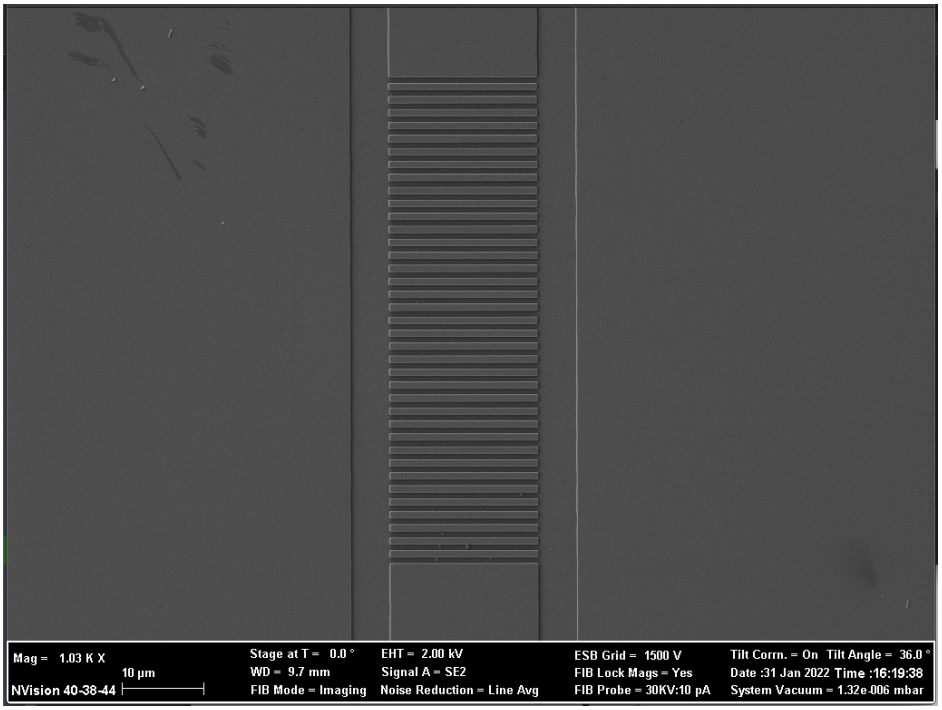

FIGURE 6.7: SEM image showing the grating coupler designed for coupling 3.8 μm light.

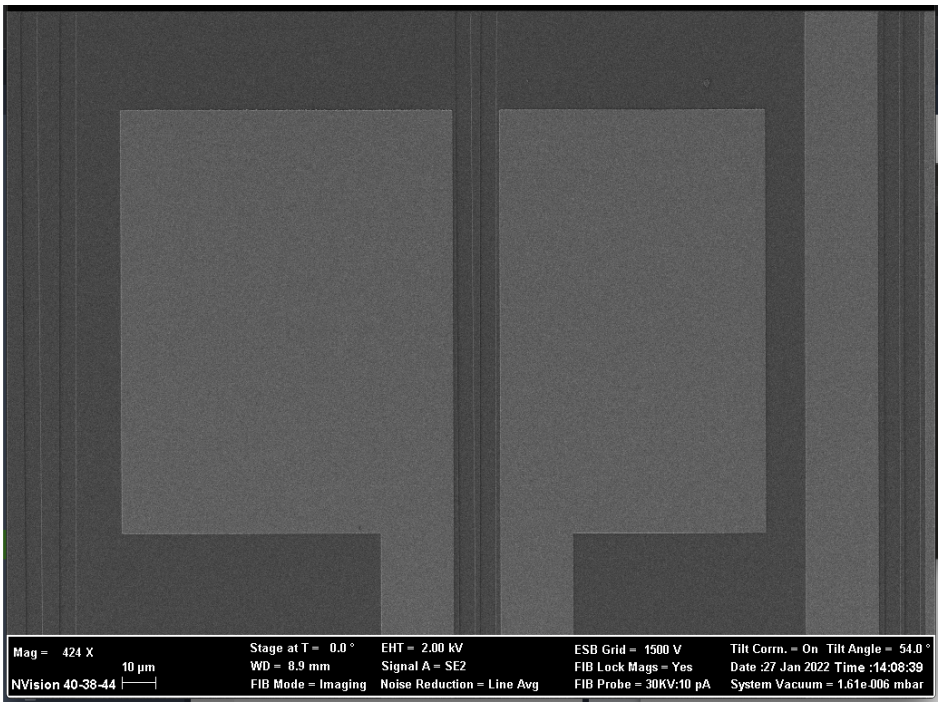

FIGURE 6.8: Image of Ohmic contact pads.

6.7 Summary

This chapter described the fabrication process in creating the final photodiodes. Two 500 nm germanium on SOI wafers were used to fabricate devices on. On each wafer, the same processes took place. The first being the E-beam lithography used to create the waveguides and grating couplers. After which, the wafers were prepared and sent to the University of Surrey Ion Beam Centre to implant dopants, boron and phosphorus to create P++ and N++ doped regions. Once returned the wafers both received annealing to activate the doping. To create Ohmnic contacts vias were etched within the SiO_2 and germanium and then through metal evaporation layers of nickle, titanium and aluminium were doposited. Finally, one of the two wafers were cleaved into subsets of chips to be implanted with ions at both the University of Surrey Ion Beam Centre and ETH Zurich to create defects within the rib waveguide.

Chapter 7

Experimental Results

This chapter presents the characterisation of photodiodes and their DC performance at 2 μm and 3.8 μm as well as their RF performance at 2 μm. All experiments were performed at room temperature. This chapter is divided into 6 sections:

- Details and specifications of experimental equipment used.
- Passive measurements at 2 μm and 3.8 μm.
- 2 μm DC measurements and experimental setup.
- 3.8 μm DC measurements and experimental setup.
- 2 μm RF measurements and experimental setup.
- An investigation of the photodetection mechanism.

7.1 Experimental Equipment Details

This section covers the details and specifications of the equipment used in the experimental setups.

7.1.1 Lasers - Light Sources

The 2 μm light source was provided by a fibre coupled Thorlabs 2 μm laser diode (FPL-2000-PM1550). The laser operates at a centre wavelength of 2 μm $\pm$ 20 nm with a rated 15 mW typical output power. The laser is driven typically at 400 mA and can be driven up to 500 mA maximum. The thermoelectric controller (TEC) is used to keep the diode at a typical specified temperature of 25 °C. To drive the diode at the specifications listed above, a Thorlabs laser driver and temperature control mount was used (CLD 1015).

The 3.8 μm light source is a quantum cascade laser (QCL) from Daylight Solutions. It is tuneable over 3.71 - 3.90 μm. In these experiments the QCL was operated in a continuous wave mode and the laser has a maximum output power of 150 mW at the peak operating wavelength of 3.8 μm.

7.1.2 Optical Power Sensors

For measuring optical power of 2 μm light, a Thorlabs Power Sensor (S148C) was used. It has a spectral range from 1200 - 2500 nm and has a responsivity of 2 mA/W at 2 μm. The optical power working range spans from 1 μW to 1 W. The response time is 1 μs and a resolution of 1 nW.

For measuring 3.8 μm light two power sensors were used a Thorlabs S401C10 thermal power sensor and a Vigo Systems HgCdTe PVI-4TE-4 photodetector. The Thorlabs power sensor covers a spectral range from 190 nm to 20 μm. The optical power working range spans from 10 μW to 1 W with a resolution of 1 μW and a response time of 1.1 s. The Vigo Systems HgCdTe PVI-4TE-4 photodetector was used in conjunction with a chopper and lock-in amplifier (to reduce bandwidth and noise floor allowing for a larger signal to noise ratio). It has a spectral range from 2.2 – 4.2 μm and a peak responsivity of 1 A/W at 4 μm.

7.1.3 Polarisation Control

The grating couplers designed for these photodiodes are polarisation dependant so to optimise the amount of light coupled into the coupler, polarisation controls to control the polarisation of incoming light are used for 2 μm and 3.8 μm light.

The grating couplers polarisation dependence can be seen from the phase matching condition of a grating coupler:

$$k_o n_{eff} = k_o n_c sin\theta + q\frac{2\pi}{\Lambda} \tag{7.1}$$

where $k_o = \frac{2\pi}{\lambda}$ and λ is the wavelength of light, n_{eff} and n_c is the effective refractive index of the grating and the refractive index of the cladding respectively, Λ is the pitch of the grating coupler, q is an integer, θ is the angle of output light that is normal to the grating coupler (96).

The n_{eff} term in this equation is different for TE and TM light and the effect of this is that for TE and TM light the resultant optimum coupling angle is different.

The polarisation control of 2 μm light, uses a Thorlabs Manual Fibre Polarization Controller filled with a 2 μm Fibre Optic Patch Cable (Thorlabs SM2000 1.7 - 2.3 μm)

looped 6 times, to allow both half and quarter wave control of the polarisation through the creation of stress induced birefringence in the fibre. Manual control of the paddles allowed the maximisation of TE light transmission through the devices and thus more optical power to the diode.

The 3.8 μm laser emits TM polarised light and to maximise the optical power into the diodes the polarisation is controlled using an Altechnanti-reflection coated cadmium thiogallate half-wave plate which was inserted in the free-space path of the beam to allow as much light to be coupled as possible.

7.1.4 Lock-In Amplifier

The lock-in amplifier (Signal Recovery SR7265 lock-in amplifier) was used to reduce noise in the measurement of 3.8 μm light. It operates over a frequency range of 1 mHz to 250 KHz. It is used in conjunction with a chopper placed in the path of the 3.8 μm free-space laser, which modulates the optical light at a frequency that can be detected by the lock-in amplifier, i.e., 444 Hz.

7.1.5 Ammeter and Voltage Source - Keithley 6487

The Keithley 6487 was used as the ammeter and voltage source for active measurements. It is able to take readings 1000 times per second. It can provide a voltage up to 10 V with a voltage resolution of 0.2 mV and can measure a current up to 20 mA with a current resolution of 10 fA. The Keithley is controlled via a python script to automate current measurements over a changing voltage.

7.1.6 RF Signal Generation

For modulating the 2 μm light a lithium niobate optical intensity modulator (Photline Technologies MX2000-LN-10) was used. It operates over wavelengths between 1900 nm and 2200 nm. It has a typical electro-optic 3dB bandwidth of 12 GHz.

To provide an electrical RF signal to the modulator a signal generator (Agilent E8257D PSG Analog Singal Generator) providing a pseudo random bit pattern was used, alongside a bit pattern generator (SHF 12104A). The signal generator can create signals with frequencies between 100 MHz and 67 GHz. The bit pattern generator can generate bit patterns from 3 - 64 Gbps

7.2 Test Structures

Test structures allow the function of individuals components of a photodiode device to be probed, which is useful for separating the loss of the grating coupler from the loss of a whole photodiode, or the propagation loss of a waveguide from loss from the doping of metal absorption in a photodiode. There are test structures designed at each wavelength on each chip alongside the photodiodes, as described in section 5.4.3. This section will describe the measurements of insertion loss and propagation loss taken using these test structures.

7.2.1 Insertion Loss

Insertion loss accounts for the optical power loss that occurs as the light is coupled from free-space into the detector i.e., the grating coupler and taper waveguide. The insertion loss associated with each photodiode is measured and accounted for when calculating responsivity later in this chapter. To find the insertion loss, a test structure comprising two grating couplers and tapers is used, see Figure 7.1.

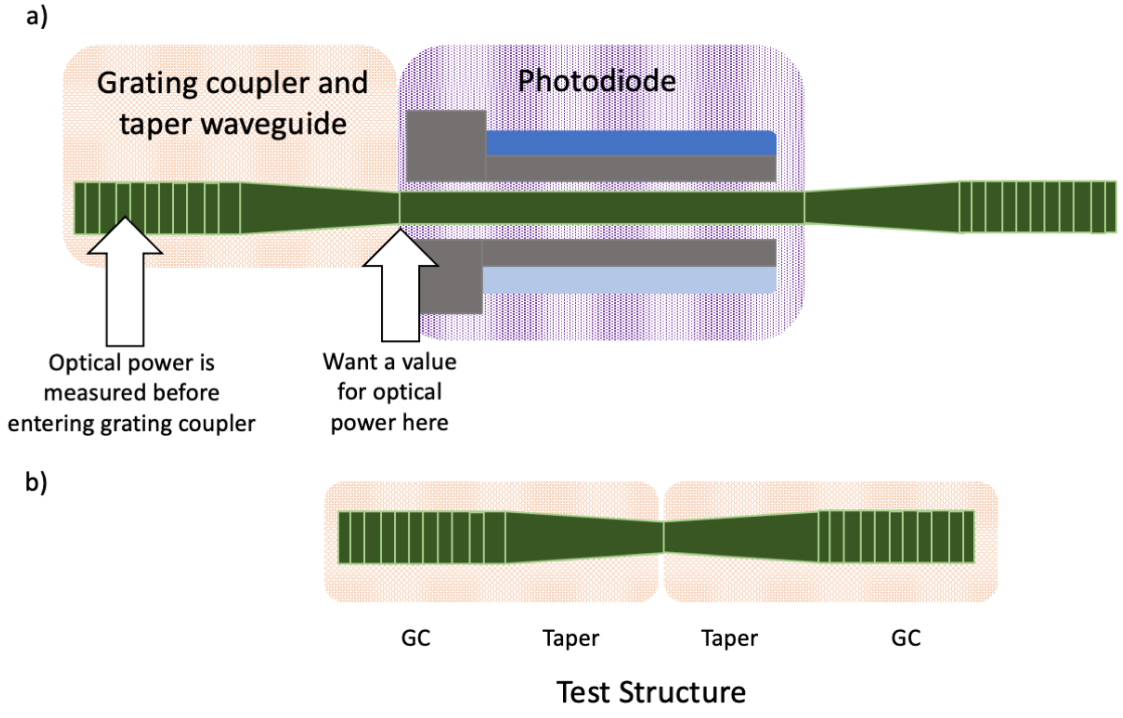

FIGURE 7.1: a) Complete photodiode is shown to visually explain the importance of insertion loss b) Diagram showing that the test structure (on bottom) used for finding insertion loss caused by a single grating coupler and taper.

To find the insertion loss, the light entering and exiting the test structure is measured and the loss of a test structure, $Loss_{TS}$, is found as,

$$Loss_{TS} = 10 \times Log_{10}(\frac{P_{in}}{P_{out}}) \tag{7.2}$$

where P_{in} is the optical power entering the structure and P_{out} is the optical power exiting the structure. The loss attributed to a single grating coupler is found by comparing power into the structure to power out and dividing by two. However because a fibre is used to guide the light from the output of the device to a MIR detector (see Figure 7.2), the loss of this fibre should be accounted for to isolate the loss to just a single grating coupler and taper. The loss of the fibre is found by measuring optical power in and out of the fibre and using Eq. (7.2). The equation then used to calculate the loss on a single GC and taper, $Loss_{GC}$, is

$$Loss_{GC} = (\frac{Loss_{TS} - Loss_{FO}}{2}) \tag{7.3}$$

where $Loss_{FO}$ is the loss of the fibre coupling light between the grating coupler and MIR detector.

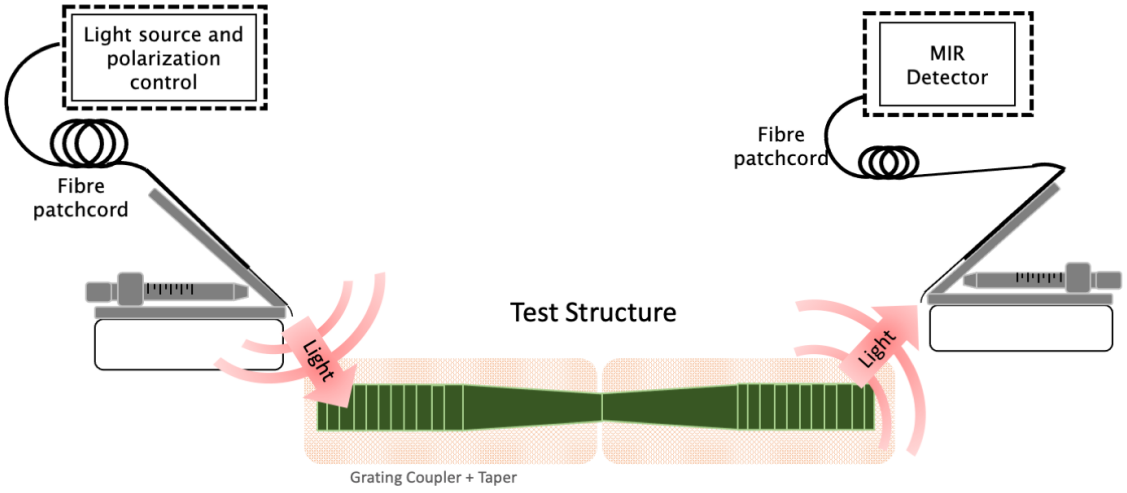

FIGURE 7.2: Diagram showing the test setup for insertion loss. The light source, polarisation control and MIR detector are changed to create a 2 μm and 3.8 μm system.

The 2 μm and 3.8 μm light is coupled through the structure and transmission is maximised by carefully aligning the fibres. Polarisation control is also optimised to allow the maximum possible power through the structure. The power entering and exiting the fibre between the MIR detector and test structure is also measured to account for its loss in the system. The insertion loss is measured and calculated on each chip and for each wavelength used, as variations may occur over the different chips.

7.2.2 Insertion Loss Results

A table of insertion losses are calculated and shown below in Table 5.1.

	1.95 μm		2.05 μm		3.8 μm	
	Loss (dB)	Angle (°)	Loss (dB)	Angle (°)	Loss (dB)	Angle (°)
Chip 10	10.004	16.0	9.14	3.2	18.00	16.0
Chip 12	10.8	16.0	11.3	3.3	9.41	16.0
Chip 2	-	-	20.6	3.2	-	-
Chip 34	10.80	16.0	16.8	3.2	-	-
Chip 56	10.32	18.6	8.85	4.0	-	-
Chip 7	9.84	18.6	8.55	4.0	-	-

TABLE 7.1: Losses calculated on a single GC + tapers for different chips, wavelengths and grating couplers.

For the grating couplers designed for 1.95 μm, the angle with the highest transmission was around 17 degrees and the grating coupler loss was generally around 10 dB. The variation in loss was likely down to angle chosen, alignment inaccuracies, fabrication errors, equipment errors (the angleometer used had an error of $\pm$ 1 °. For chip 2 there are no test structures at 1.95 μm, this is because when the wafers were cleaved, the bottom of some chips were also cleaved off due to the cleaving line not being perfectly horizontal. For the responsivity of the devices in chip 2 the loss was assumed to be 10 dB as the angle used was at 16 °.

For the grating couplers designed for 2.05 μm, the optimum angle was at around 3 degrees and a slightly lower loss compared to the 1.95 and 3.8 μm grating couplers.

Finally the 3.80 μm optimised couplers, were used at fibre angle 16 degrees. The wavelength dependence of the grating coupler loss between 3760 and 3880 nm was also found. The peak efficiency centred around 3.82 μm. Fluctuations in this graph are caused by fibre vibrations changing the power entering the structure, see Figure 7.3.

7.2.3 Propagation Loss

The propagation loss of the waveguides was measured using a cut back method, by calculating the relative loss through 3 waveguides of different lengths. The 3 lengths of waveguides are 0, 2 and 4 mm. The 2 and 4 mm long waveguides are normalised to the 0 mm one by substracting the power through the 0 mm waveguide from the 2 and 4 mm long waveguide transmission. By doing this, only the transmissions of the waveguides are

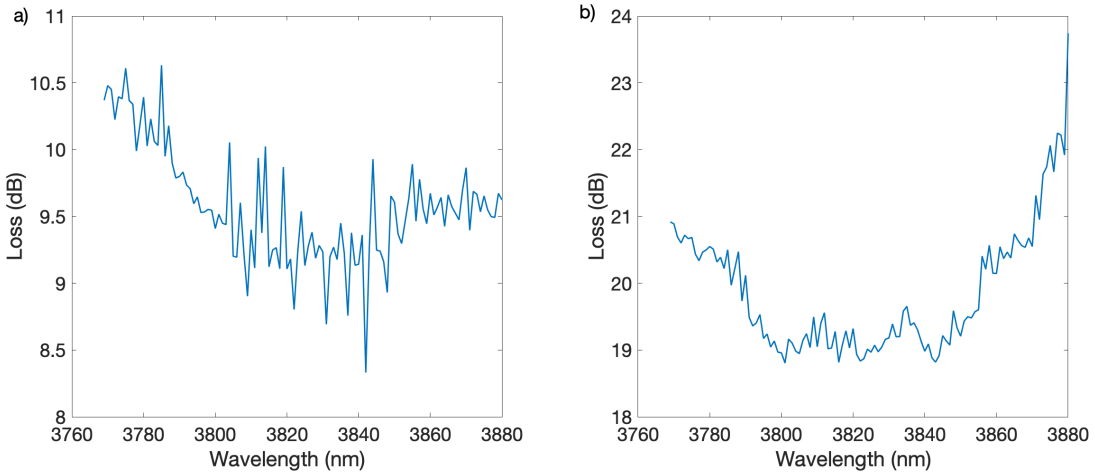

FIGURE 7.3: Loss of grating coupler and taper combined versus wavelength of light from a) chip 12 b) chip 10.

required for calculating loss. The propagation loss is then found as a line of best fit through a scatter graph of the normalised loss (dB) versus the waveguide length (cm), giving a value of propagation loss in dB/cm.

At 2 μm the light is guided through the 700 nm wide rib waveguides and the tranmission is measured using a Thorlabs S148C Photodiode Power Sensor. The normalised transmission through the waveguides is plotted versus length and propagation loss is calculated using a line of best fit (Figure 7.4) giving a value of 12.4 dB/cm for the propagation loss and $\pm$ 3 dB/cm being within the 95% confidence interval.

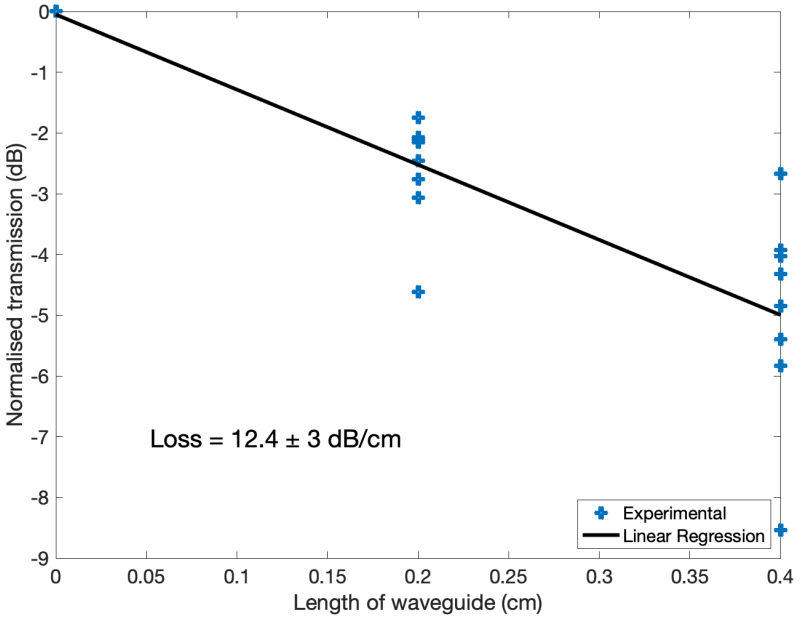

FIGURE 7.4: Graph showing propagation loss at 2 μm.

At 3.8 μm the light is guided through the 1400 nm wide rib waveguides. The transmission is measured using a Vigo Systems HgCdTe PVI-4TE-4 photodetector, chopper and lock-in amplifier. The normalised transmission through the waveguides is plotted versus length, and propagation loss is calculated using a line of best fit, (Figure 7.5) giving a value of 17.0 dB/cm for the propagation loss, with a 95 % confidence interval of $\pm$ 2.4 dB/cm.

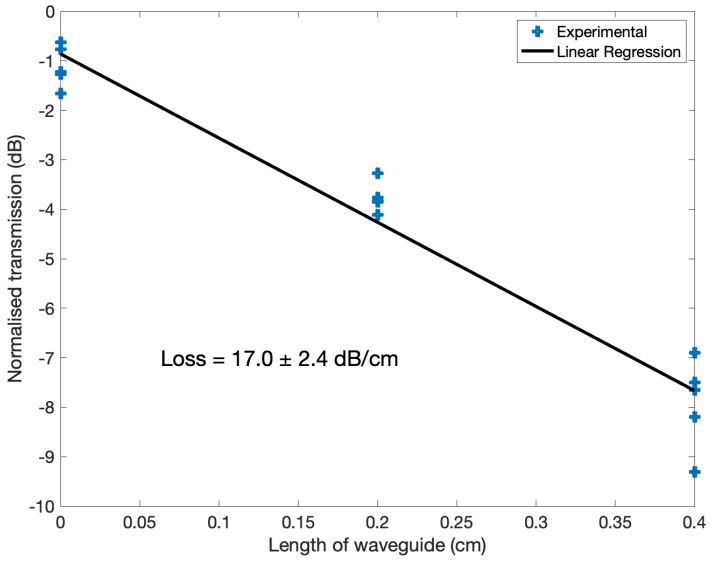

FIGURE 7.5: Graph showing propagation loss at 3.8 μm.

7.3 Responsivity

The first active measurement performed was of the responsivity at 2 μm light just above germanium bandgap. Afterwards the responsivity of the diodes at 3.8 μm was found. A list of the parameters investigated using chips of different implantation doses and diodes of various lengths implanted with defects are listed below.

- Effect of implantation fluence on responsivity.
- Effect of implanted length of detector on responsivity.
- Reproduciblity of measurement and values.
- The measurement of responsivity using different grating coupler designs to couple same wavelength, to verify reproduciblity.

7.3.1 Experimental Setup for DC Characterisation at 2 μm

A diagram of the experimental setup used for DC characterisation is shown below, see Figure 7.6.

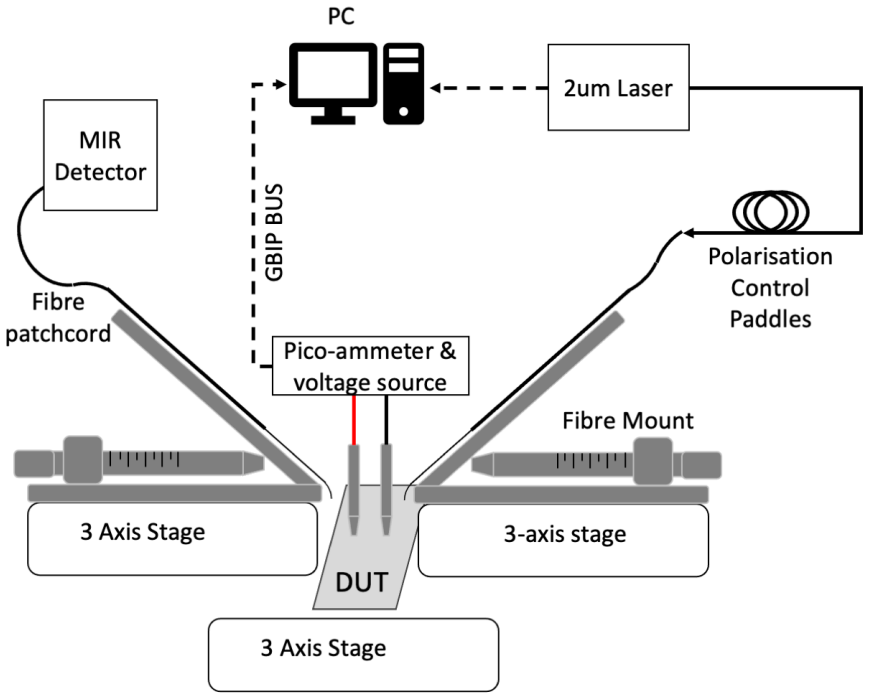

FIGURE 7.6: Diagram of 2 μm setup. Solid black lines show fibre connections and dotted line shows electrical connections.

The device under test (DUT) is viewed using a camera with magnification and a monitor. The DUT is positioned under the camera using a 3-axis stage to control its position. The 2 μm light source is a Thorlabs FPL-2000-PM1550 laser diode that is coupled into single-mode Thorlabs SM2000 patch cable. This fibre is looped and placed within a Thorlabs manual polarisation, to control polarisation of light entering the photodiode. After, the light is coupled into polarisation maintaining fibre (P3-2000PM-FC-2 fibres). The ends of this fibre are striped and cleaved and placed in an angle controled mount. The mount is on a 3 axis stage allowing the fibre to be carefully positioned above the device's grating couplers to a micrometer scale accuracy. To couple light out from the chip another polarisation maintaining fibre (P3-2000PM-FC-2) is cleaved, mounted and placed on a stage as the previous fibre. For optical power measurements, this output fibre is used to couple light into a MIR photodiode (Thorlabs S148C Photodiode Power Sensor). For the electrical measurements, a ground and source DC probe are placed in 3-axis stages and are connected to a Picoammeter/Voltage source (Keithley 6487 Picoammeter/Voltage source) to allow for the measurement of current and supply of voltage to provide a reverse bias. The picoammeter is connected to computer via GPIB cable which allows python scripts to automate voltage sweeps and current measurements.

7.3.1.1 Results at 2 μm

First, the responsivity for varying photodiode implantation length was measured. This was initially done to find which length of boron implanted photodiode resulted in the best responsivity. This was repeated over three different implantation doses and the photodiode had no reverse bias applied. To perform the measurement 2 μm light was coupled into the photodiode and both the photocurrent with light on and off were measured with the light off value being subtracted from the laser light on to find the net photocurrent (A). The optical power of light entering the devices is measured using the Thorlabs S148C power sensor placed directly under the cleaved fibre outputting light. To account for the insertion loss it is measured using the same fibre angle, directly before or after the active measurement for the insertion loss to most accurately match the photodiode. This loss is applied to the optical power to give a value for the power entering the photodiode, as described in section 7.2.1. The responsivity in A/W is found by dividing the net photocurrent by the optical power entering the photodiode. The responsivity for detectors of different implanted lengths over 3 different implantation doses is shown below in Figure 7.7.

The three graphs show the responsivity versus implanted length of the photodiode for three boron implantation doses, $1x10^{14}$, $1x10^{12}$ and $1x10^{10}$ ions/cm^2 in a), b) and c) respectively. The 4 curves on each graph distinguish between the grating coupler design used and from which chip the detector is from. By comparing graphs a) b) and c) it can be seen that the $1x10^{14}$ ions/cm^2 implantated devices has the lowest response and $1x10^{12}$ and $1x10^{14}$ had a similar response with $1x10^{12}$ ions/cm^2 being slightly lowest. In graphs a) and b) there is a slight downward trend as the implanted length increases.

From Figure 7.7 it can be seen that unimplanted detectors have the largest responsivity of up to 0.17 A/W. These results were taken with no reverse bias applied. Knowing that the unimplanted devices are the most responsive the next measurement was to measure IV curves of the unimplanted photodiodes to learn about their behaviour over different reverse bias voltages. The measurement process is the same as before however instead of operating at 0 V, the Keithley ammeter/voltage source is scripted to sweep the voltage from 0 to 10 V over 100 points and measure the current at each of those points. The IV curve is measured with light on and off. The insertion loss is accounted for when plotting the responsivity. The graph below in Figure 7.8 a) show graphs of responsivity versus reverse bias voltage of two unimplanted photodetectors and Figure 7.8 b) shows the photocurrent of both detectors when illuminated and dark. The successful high responsivity of these devices prompted further investigation into the spectral response and the responsivity at 3.8 μm was measured next.

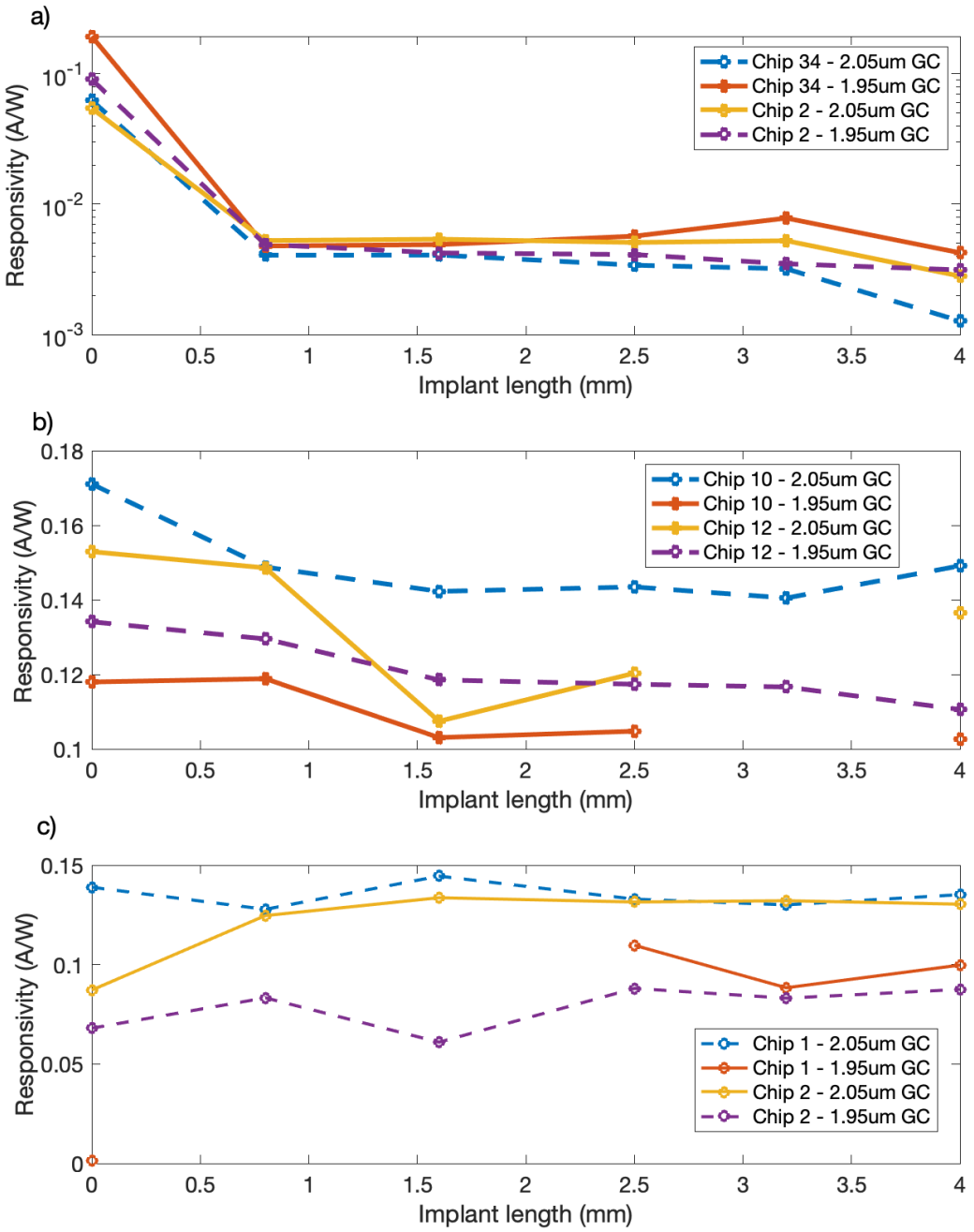

FIGURE 7.7: Graphs of responsivity versus the defect implanted length of 4 mm long photodiode at a) 1x10^{14} b) 1x10^{12} and c) 1x10^{10} ions/cm^2. Within each of these graphs the curves depict which chip and GC (grating coupler) design was used.

7.3.2 Experimental Setup for DC Characterisation at 3.8 μm

The experimental setup for DC characterisation at 3.8 μm is shown in Figure 7.9. As a 3.8 μm light source it uses a Daylight Solutions QCL laser with a tuneable wavelength between 3.71 to 3.90 μm. A chopper is placed in the free-space path of the laser output allowing the light to be modulated so that it can be recognised by the lock-in amplifier and an Altechna anti-reflection coated cadmium thiogallate half-wave plate for rotating the

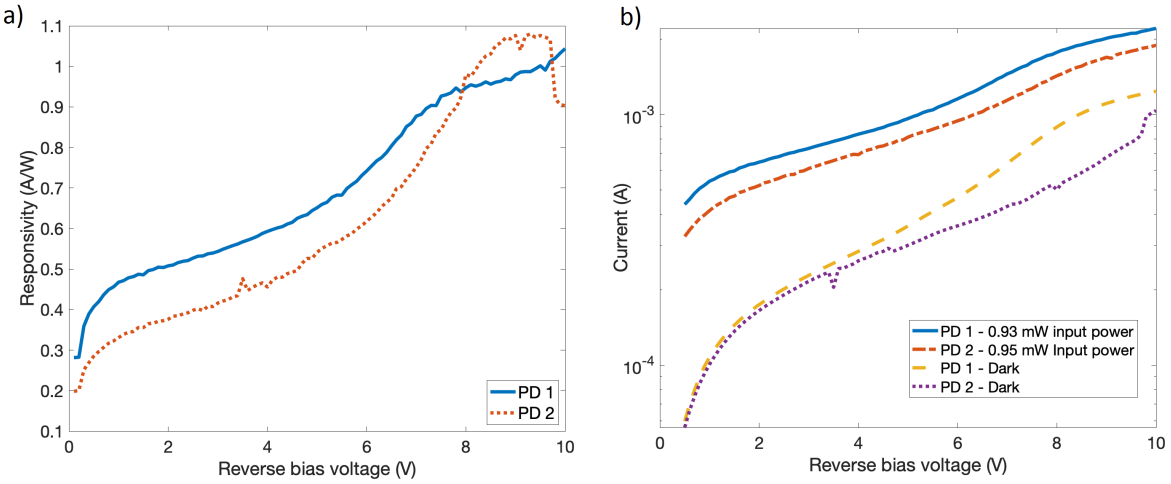

FIGURE 7.8: a) shows the responsivity plotted against reverse bias voltage for two photodiodes from two different chips b) shows the illuminated and dark current curves used when calculating the responsivities plotted in a).

polarisation is also placed in the free-space beam. Mirrors are used to direct the beam through the chopper and half wave plate while aligning it to the collimator to maximise coupling from free-space into patchcord fibres. The free-space beam from this laser is finally collimated into single mode Thorlabs InF3 fibre using a ZnSe lens.

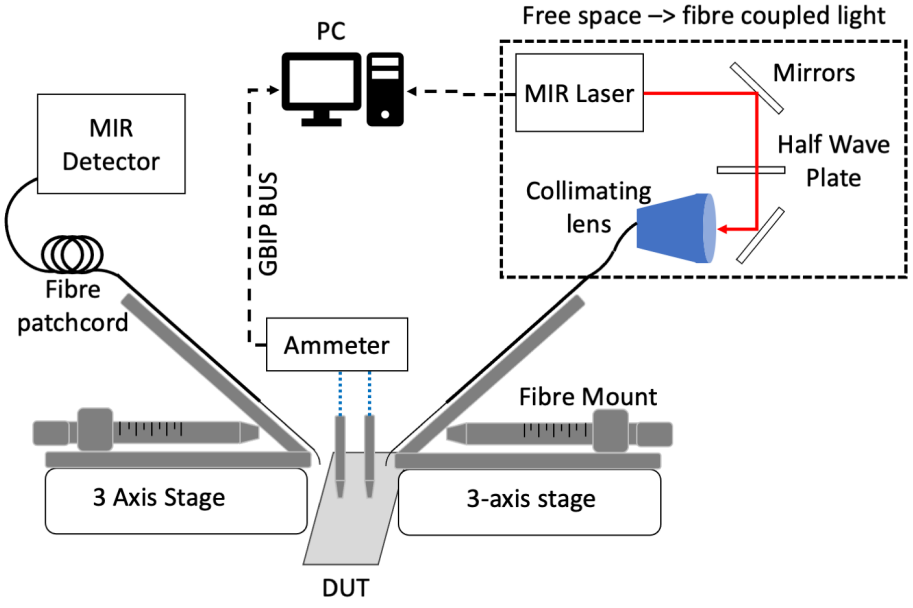

FIGURE 7.9: Diagram of setup used for measuring responsivity at 3.8 μm.

Similarly to the 2 μm setup, InF3 fibres are cleaved, mounted and placed apon on a 3 axis stage where their position and angle relative the chip can be changed. Another cleaved fibre mounted on stage is used to couple and guide light from the chip to an external MIR detector. Two MIR detectors were used for measuring the optical power of 3.8 μm light,

one being a Thorlabs S401C10 thermal power sensor, which could directly measure the optical power and is used for measuring the power entering the photodiode, and the second is a Vigo Systems HgCdTe (MCT) PVI-4TE-4 photodetector, which was used for free-space alignment.

7.3.3 Results at 3.8 μm

The process of measuring the IV curves at 3.8 μm is the same as those for 2 μm, light is coupled into the photodiode and the optical power into the device is measured. The insertion loss is calculated using this optical power and the photogenerated current, which is calculated using the illuminated and dark IV curves. The results of the responsivity of an unimplanted detector at 3.8 μm are shown in Figure 7.10, where a) show IV curves of two unimplanted photodetectors and Figure 7.10 b) shows the photocurrent of both detectors when illuminated at 1.1 mW and when dark.

The dark current is very high compared to the photocurrent (i.e. 0.372 A at -7 V), higher than when measured at 2 μm. The grating coupler insertion loss was measured to be 9.4 dB. Despite the high dark current a responsivity of 0.1 A/W is calculated from these curves at -7 V reverse bias.

7.4 RF Characterisation at 2 μm

To investigate the viability of the detectors for telecommunication applications the speed of the detectors were measured. There are two types of bandwidth measurements performed, both at 2 μm as these were the only available modulators possessed. The first measurement was the electro-optic bandwidth curve and the other was looking at eye pattern of that same detector at a high speed. Both of these experiments were performed on unimplanted devices.

7.4.1 Experimental Setup for measuring Electro-optic Bandwidth

The setup used for measuring electro-optic bandwidth can be best thought of as the optical setup and electrical setup and a diagram of the setup is shown in Figure 7.11.

The optical setup consists of a 2 μm light laser diode, Thorlabs FPL-2000-PM1550, driven by a laser diode CLD 1015. The light is then coupled into a 2 μm optical modulator (MX2000-LN-10) after which coupled into a polarisation control paddles created using looped single mode 2 μm fibres (Thorlabs SM2000 fibre). To direct the light onto the chip, the fibre is cleaved and placed in a fibre mount apon a 3 axis stage, allowing it to be moved to a micron scale precision above the grating coupler.

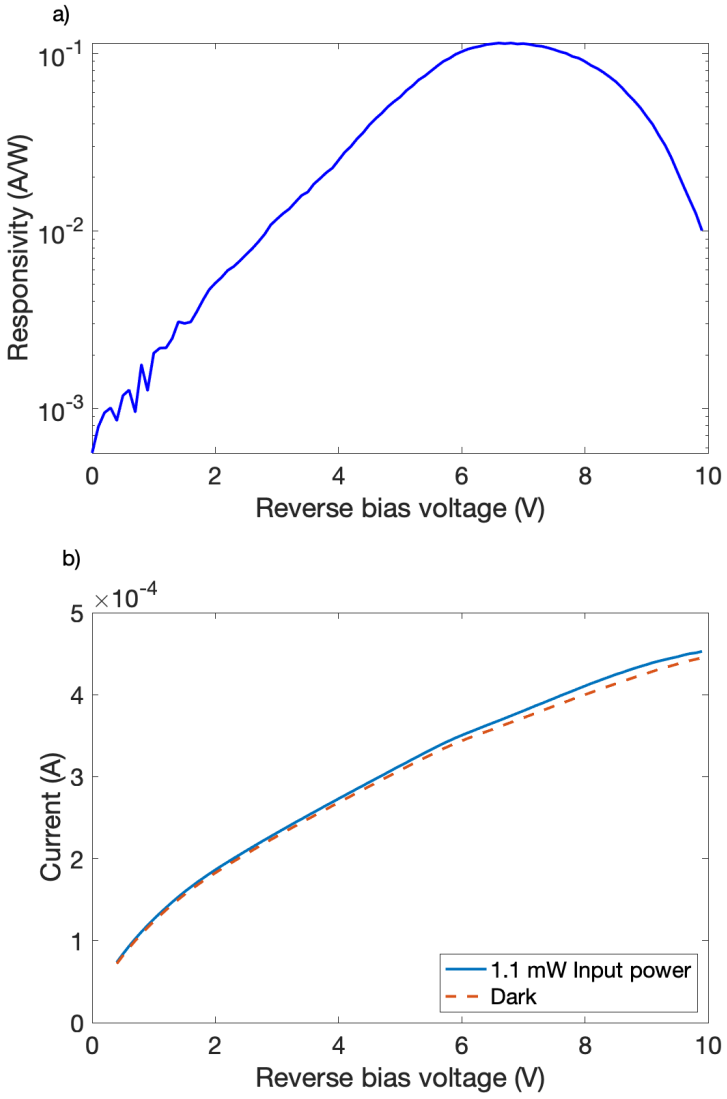

FIGURE 7.10: a) Graph of responsivity versus reverse bias voltage for a photodiode at 3.8 μm b) Plots the illuminated and dark curve used when calculating the responsivity in a).

The electrical setup revolves around the use of the VNA (Agilent N5225A). The VNA signal out port is connected a 40 GHz electrical cable to the modulator to provide the modulated electrical signal. The next part of the electrical setup is measuring the modulated photocurrent from the photodiode and feeding this into the VNA. An RF probe (40A-GS-125-DP picoprobe) is connected to the photodiode contacts. A bias tee (Dual bias tee - Picosecond Labs) is connected directly to the probe and to separate the DC and RF components. The DC connection on the tee is connected to a picoammetre and voltage source, where a reverse bias can be provided to the photodiode. The RF connection of the tee is connected to two amplifiers in series, with each amplifier connected to its own voltage supply, before being reconnected to the VNA, see Figure 7.11.

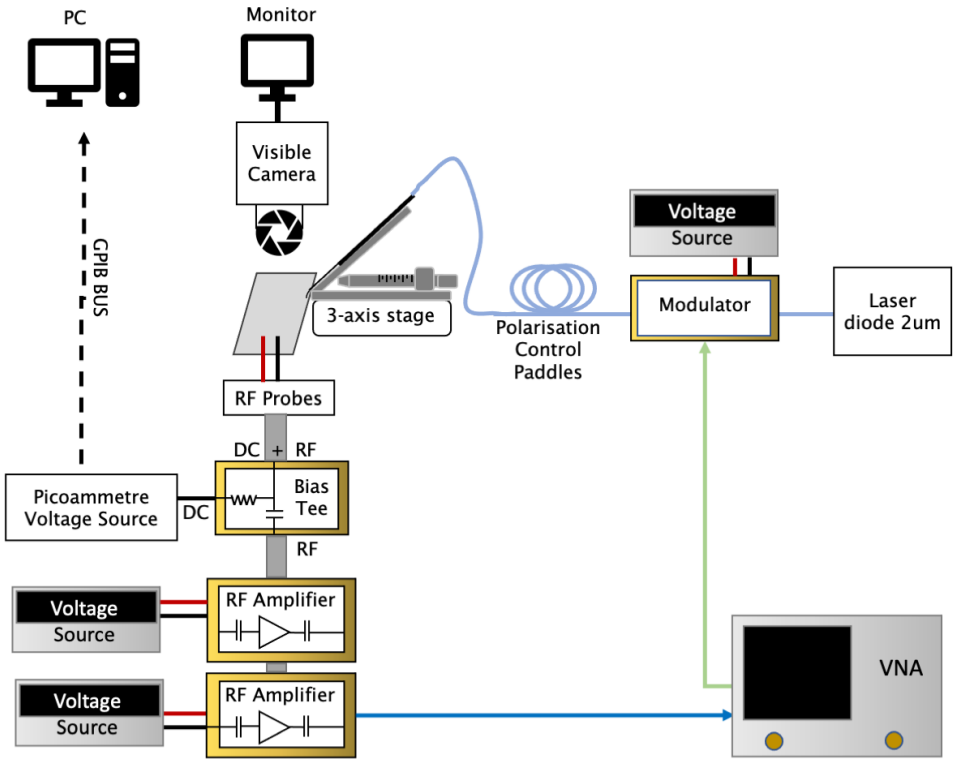

FIGURE 7.11: Diagram of setup used for measuring electro-optic Bandwidth.

7.4.1.1 Electro-optic Bandwidth Results

This graph shows the electro-optic Bandwidth (EO) response for the an illuminated and non-illuminated photodiode, using 0 and 2 amplifiers. Because of the nature of the 2 μm modulator the electrical response of it couldn't be calibrated and accounted for, the measured bandwidth is shown in Figure 7.12.

While there are large differences between the illuminated and dark curves even at high frequencies, the 3 dB bandwidths of both curves are fairly low, less than 1 GHz. There are also large spikes which could possibly be attributed to reflections from impedance not being matched between connections.

7.4.2 Eye Pattern

Due to the limits of the last measurements, an eye pattern of the unimplanted diode was measured. Improving on the last experiment by calibrating where possible and focusing on the less noisy, higher frequencies.

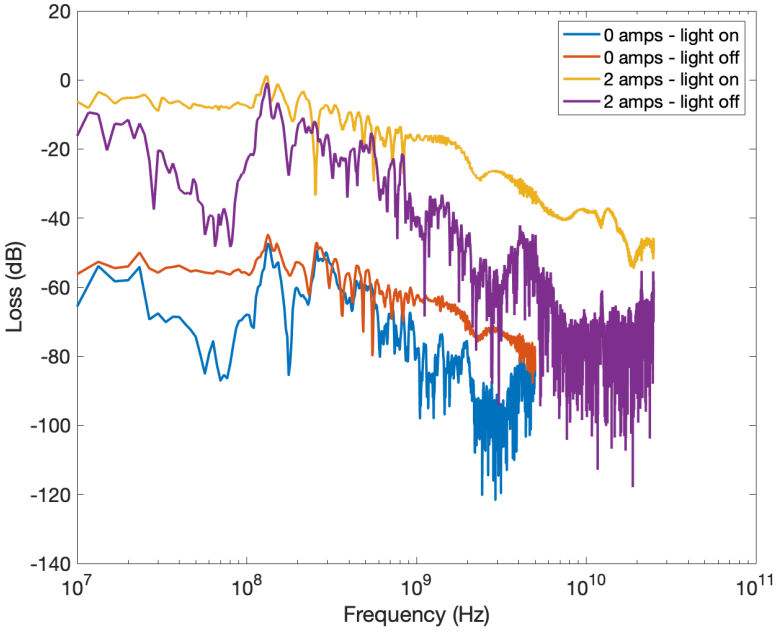

FIGURE 7.12: EO Bandwidth measured on VNA using 0 and 2 RF amplifiers with the modulated light turned on and off.

7.4.2.1 Experimental Setup for Measuring Eye Pattern

The setup used for measuring the eye pattern is almost the same as the setup used for measuring the bandwidth, see Figure 7.13 for a quick overview.

The optical setup consists of a 2 μm light laser diode, Thorlabs FPL-2000-PM1550, driven by a laser diode CLD 1015. The light is then coupled into a 2 μm optical modulator (MX2000-LN-10) after which coupled into a polarisation control paddles created using single mode 2 μm fibres (Thorlabs SM2000 fibre). To direct the light onto the chip the fibre is cleaved and placed in a fibre mount apon a 3 axis stage, allowing it to be moved to a micron precision scale above the grating coupler.

The electrical setup uses a signal generator (Agilent E8257D PSG Analog Singal Generator) and bit pattern generator(SHF 12104A) to provide the RF signal to the modulator. To read the modulated photocurrent from the detector. An RF probe (40A-GS-125-DP picoprobe) is used to connect to the detector. A bias tee (Dual bias tee - Picosecond Labs) is connected directly to the probe. The DC connection on the tee is connected to a picoammetre and voltage source, where a reverse bias can be provided to the photodiode. A Keysight DCA-X 86100D (digital communications analyzer) is used to read and display the RF signal from the device, it is provided a trigger from the bit pattern generator.

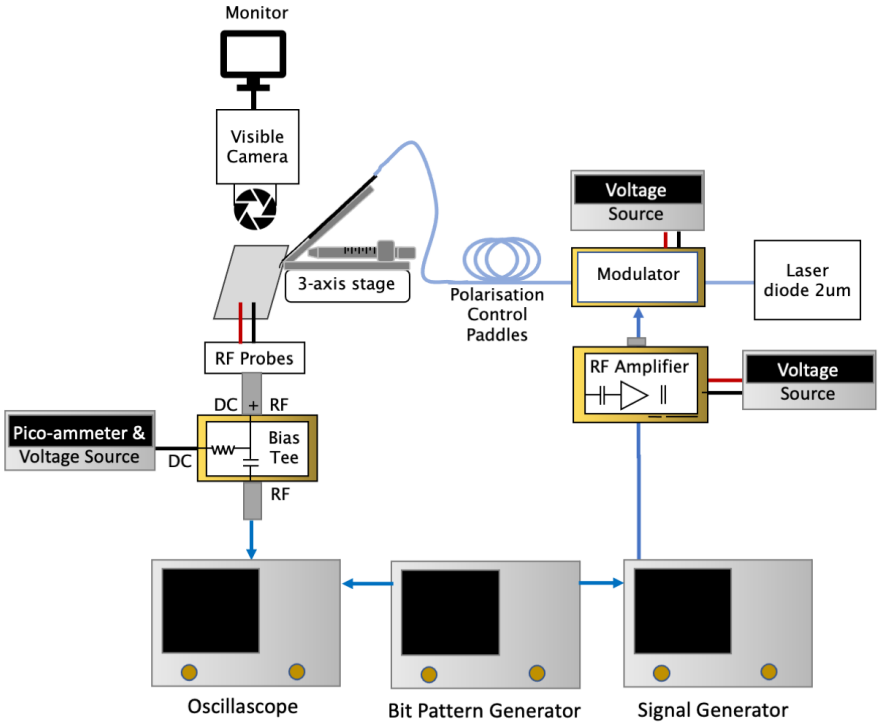

FIGURE 7.13: Experimental setup used to find the eye pattern diagram of the device.

7.4.2.2 Eye Pattern Results

To investigate the highest possible symbol rates of the photodiodes, 5 tap linear feedforward equalization was adopted on the DCA and the resulting open eye diagram is shown in Figure 7.14. The signal to noise ratio of the measured eye is 4.8 with an amplitude of 2.8 mV. This eye pattern included calibrations accounting for the 6 dB attenuator, RF cable and bias Tee.

Attempts to measure an open eye patterns above 12.5 Gbits/s at both 15 and 20 Gbits/s proved unsuccessful, both of these values returned closed eyes.

7.5 Photodetection Mechanism Investigation

As seen in graphs in Figure 7.7 from the DC responsivity at 2 μm, it is apparent that the added defects caused by boron implantation are not enhancing the responsivity but hindering it instead. This leaves the actual photodetection mechanism unclear as germanium does not inherently absorb light above 2 μm. To deduce what the photodetection mechanism could be, experiments are performed to investigate possibilities, including, two photon absorption, germanium strain and finally by comparing the measurements to literature.

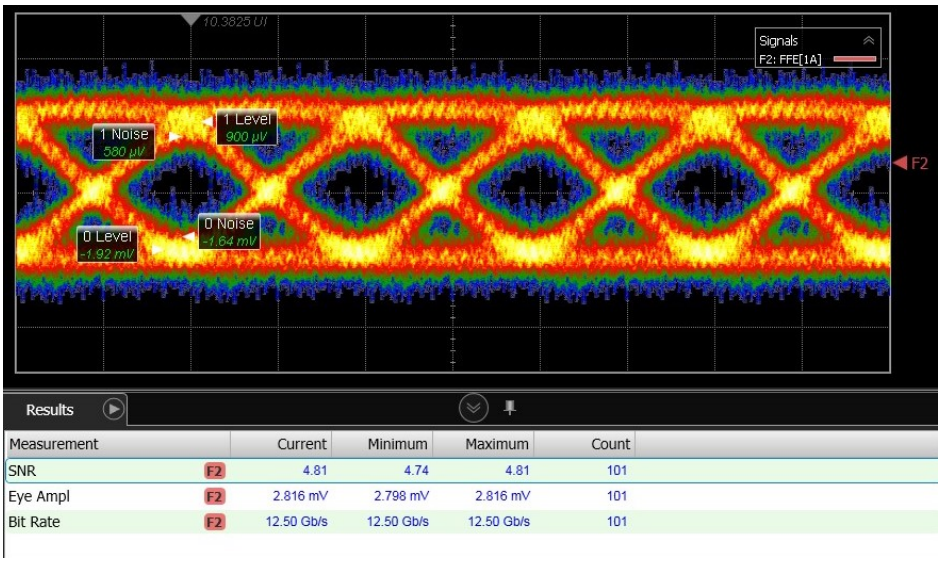

FIGURE 7.14: Open eye diagram from a unimplanted photodiode using modulated 2 μm light.

7.5.1 Two Photon Absorption

Two photon absorption is a non-linear process where electron excitation energy is provided from two photons simultaneously, and so is more likely with more light intensity, which is why the probability of two photon absorption scales with the intensity of light squared. Two photon absorption could possibly allow absorption in an otherwise transparent material, as long as the wavelength is less than 2 times the band edge wavelength.

Therefore the linearity of the relationship between the photocurrent and optical power is investigated within the unimplanted devices at both 2 μm and 3.8 μm, using the same DC setup in sections 7.3.1 and 7.3.2. The optical power entering the device is swept and at each interval the current is measured, no reverse bias is applied. The photocurrent measured is plotted against optical power and a line of best fit is plotted to investigate linearity, see Figure 7.15. In Figure 7.15 an approximately linear relationship can be seen for both 2 μm and 3.8 μm light, indicating that two photon absorption is unlikely to be the cause of absorption within the photodetectors.

7.5.2 Metal and Doping Absorption Loss

A paper by Zhao *et al.* demonstrated a 5 mm long photodiode with a 0.25 A/W responsivity using a 5V reverse bias at 1960 nm. They suggest that the enhanced responsivity is from defect mediated absorption caused by PIN formation. They deduced this by investigating the optical loss caused by PIN structure by comparing it to the loss of the waveguide and found a loss of 3.8 dB/mm and 1.6 dB/mm respectively (97).

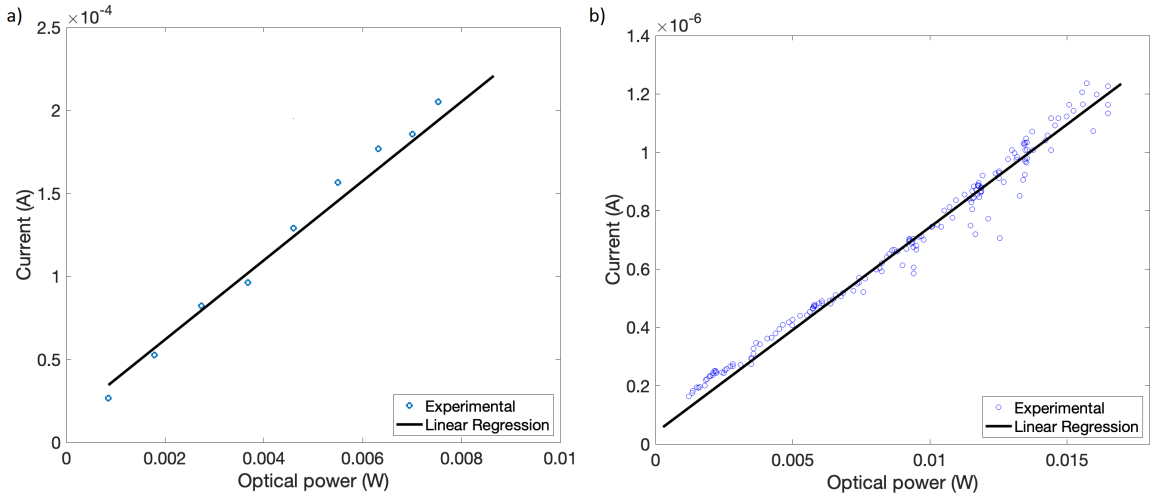

FIGURE 7.15: A photocurrent versus optical power of light entering graph for a) - 2 μm light b) - 3.8 μm light.

A similar comparison was performed using the photodiodes and waveguides from this project. The transmission of 3.8 μm light through waveguides, waveguides including doping and complete photodiodes (with doping and metal contacts) were performed to investigate the individual contribution of loss from metal contacts and doped regions. This was repeated over 3 sets of loss structures to gather an average value of loss over each of the devices. Compared to the waveguides, waveguides with doping had a 0.1 dB smaller loss and the photodiodes had a 0.7 dB higher loss. This indicates an insignificant additional loss was provided by the doping and metal contacts of the photodiode.

7.5.3 Effect of strain on Bandgap

In unstrained intrinsic crystalline Ge, the responsivity beyond 2μm in a detector would be very low as the absorption coefficient at 2.0 μm wavelength is smaller than 0.1 cm^{-1}, and at 3.8 μm wavelength this is even smaller as at this wavelength the energy is far smaller than germaniums indirect bandgap (98). However, it is known that tensile strain within germanium can increase the responsivity of detectors beyond the band edge, by shifting the germanium band edge to longer wavelengths (99).

To investigate the possibility of strain being the source of photodetection, the strain in the photodiodes is measured. To do this, the Raman spectra from the photodiode chip and a pure germanium wafer (to act as an unstrained reference) were measured using an inVia Renishaw Raman Microscope system. On both the germanium wafer and detector chip, 40 measurements of the spectrum where taken at various points across the surface. The values of the measured Ge-Ge peaks in both the germanium wafer and chip were plotted on a histrogram and a Lorentzian function is plotted against them to find a peak position, see Figure 7.16.

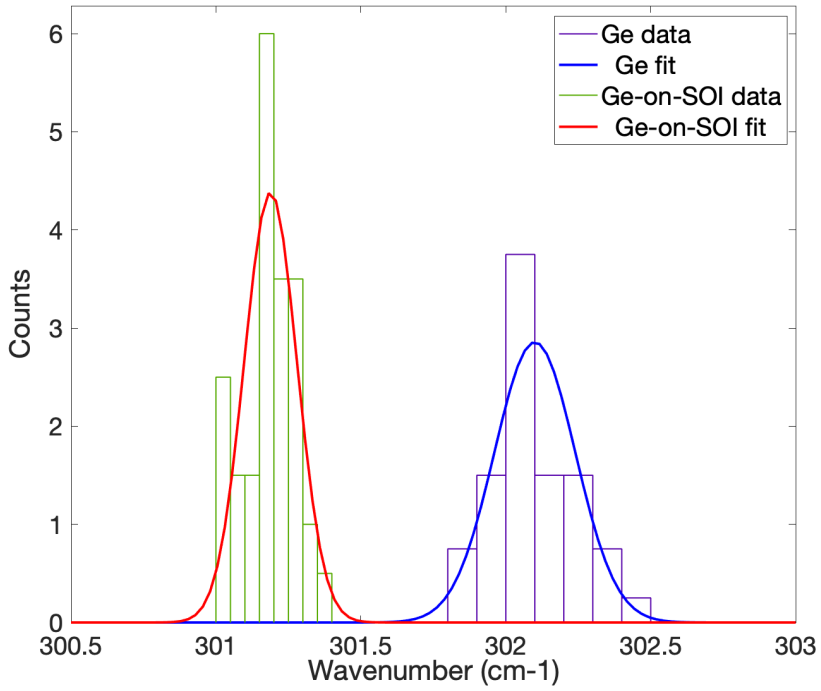

FIGURE 7.16: Graph showing a histogram of Ge-Ge peaks measured on a pure germanium wafer and this project's Ge-on-SOI chip.

The peak positions are 302.10 cm^{-1} with a standard deviation of 0.14 cm^{-1} for the pure germanium and 301.19 cm^{-1} with a standard deviation of 0.09 cm^{-1} for the photodiode chip, resulting in a shift of -0.91 cm^{-1} and in turn a tensile strain of 0.22 %. This was calculated using the linear relationship,

$$\Delta\epsilon = \frac{\Delta\omega}{b}, \tag{7.4}$$

where ϵ is the strain, ω is the wavenumber and b is the strain shift coefficient, which is assumed as 407 cm^{-1} from a paper by R. Anthony *et al.* where the strain is similarly calculated for a germanium waveguide integrated detector.

With the value of $\Delta\epsilon$ found, the change of the bandgap energy was found by using a theoretical model of biaxial strain versus bandgap energy from Y. Niquet *et al.* (100). The change in bandgap energy was then calculated to be -0.037 eV when averaged over three crystal orientations. By applying this shift in the bandgap to an absorption spectrum of germanium, an optical loss at 2 μm is found to be 11 dB/cm; this is a similar value to the propagation loss measured in the waveguides measured at 2 μm of 12.4 dB/cm. From this, the majority of the detection at 2 μm could be explained by induced strain. However, it is unlikely to be the cause of absorption at 3.8 μm because a band edge shift of -0.037 eV would be far too small to produce sufficient absorption at this wavelength.

The defects may have been created during wafer growth. This assumption is made based from TEM images gathered from devices from other members of our group (101). The TEM images looked at the germanium/silicon boundary of a Ge-on-Si samples with 3 m thick Ge layer on Si substrate which was fabricated using the same method described in section 6.1. In the images they found that there was a high density of threading dislocations in germanium in the first 100 nm from the boundary. However, more investigation will be required to fully determine the cause of photodetection.

7.6 Summary and Discussion

In this chapter the results of characterising the fabricated photodiodes that were implanted with boron to create defects were presented. These results lead into an investigation of the photodetection mechanism at 2 and 3.8 μm.

To accurately calculate the responsivity of the detectors, the insertion loss caused by the grating coupler and a taper was measured before each responsivity measurement. The insertion loss measured was 8.8 and 10.8 dB for PD 1 and 2 respectively when measuring the 2μm IV curves and 9.4 dB for the photodiode measured at 3.8 μm. Waveguide test structures of varying length were measured to find the propagation loss, resulting in a measured loss of 12.4 $\pm$ 3 dB/cm within the 2 μm waveguides and 17.0 $\pm$ 2.4 dB/cm in the 3.8 μm waveguides.

The characterisation of detectors began by looking at the responsivity with no reverse bias at 2μm, specifically, finding the effect of responsivity with a changing length of the waveguide that was implanted with different doses of boron at 1x10^{10} ions/cm^2, 1x10^{12} ions/cm^2 and 1x10^{14} ions/cm^2. It was found that by implanting 1x10^{10} ions/cm^2 of boron there was an insignificant change in responsivity when fully implanted compared to an unimplanted device. When implanting at a dose of 1x10^{12} ions/cm^2 there was an approximate change of 0.02 A/W between an unimplanted detector and a fully implanted detector. Finally, using an implant dose of 1x10^{14} ions/cm^2 resulted in a change of responsivity of an order of magnitude from unimplanted to the full length being implanted.

By performing this measurement it was found that introducing boron didn't add defects that enchanced the photoresponse but did show that the unimplanted photodiode presented an unexpectedly large response. The performance of the detectors without boron implants where investigated further by gathering IV curves. Using unimplanted photodiodes the reverse bias was swept from 0 to 10 V collecting the photoresponse at each point and a maximum responsivity of 1.04 was found at -10 V in PD1 and 1.08 A/W at -9.3 V in PD2. An IV curve was measured again at 3.8 μm from a reverse bias of 0 -10 V and resulted in a maximum responsivity of 0.1 A/W at a bias of -7 V.

To investigate the usefulness of the photodiodes for telecommunication applications the electroptic bandwidth was measured at 2 μm. A measurement of the bandwidth over 0 - 50 GHz resulted in reflections caused by the impedance between the photodiode and probe not being matched. So instead an eye pattern diagram was measured using a psuedorandom bit pattern of increasing data rates until the eye closed. An open eye diagram was captured at 12.5 Gbps.

The chapter concludes with a section of the investigation into photodetection mechanism as the generated photoresponse in the detector was shown not to be caused from the implanted boron ions. The investigation involved measuring the linearity of the device's response with changing optical power to look for two photon absorption, any additional optical loss caused by the addition of metal contacts and pn doping to investigate if the mechanism was caused by processes in the PN junction formation, and measuring the device strain to see if that shifted the bandgap of germanium. The devices were found to have a linear response ruling out two photon absorption as the cause of the photoresponse. It was also found that there was an insignificant change in optical loss with the addition of metal contacts and doping being added. Finally, the device strain was measured and found to be 0.22 % which may be responsible for the majority of absorption at 2 μm but does not explain the response at 3.8 μm which may have been caused by defects at the silicon/germanium boundary.

Chapter 8

Conclusions and Future Work

8.1 Conclusion

This thesis covered the design, fabrication and characterisation of MIR waveguide integrated photodiodes using a germanium on SOI platform.

To create high volume, inexpensive devices capable of performing sensing and freespace telecommunications, the field of silicon photonics aims to create MIR photonic integrated circuits (PIC). Using a silicon substrate allows the use of existing foundries and mature fabrication methods to create high volumes of devices. Within a self contained lab on chip or transceiver, a detector is required. To minimise the cost of the devices, a detector that can be monolithically integrated is required. Current monolithic detectors capable of MIR detection include defect mediated silicon detectors and photodiodes made of germanium/tin although both lack responsivity in the 3-4 μm region where absorption spectra of chemicals and low loss atmospheric windows reside for sensing and free-space telecommunication applications respectively. Introducing defects into the silicon bandgap can extend the spectral response from 1.1 μm to 2.5 μm (2). As germanium has a smaller bandgap i.e., a longer cut off wavelength than silicon, the same principle could be used to extended the response of germanium further. The project of this thesis became to investigate the possibility of a defect mediated germanium photodiode.

To design these photodiodes, research of silicon defect mediated detector designs were explored; from this, a rib waveguide was used as a base design as defects can be localised to the waveguide where guided light will overlap with added defects. Grating couplers were chosen to input light into the detector for alignment ease. Therefore, multiple photodiodes were designed allowing coupling, guiding and detection of 7 wavelengths between 2 and 3.8 μm. Simulations were performed to find parameters of a waveguide that will guide a single mode for each of the 7 wavelengths and also to find parameters of grating couplers that allowed for maximally efficient grating couplers. To create defects

within the photodiode, boron, germanium, mercury, copper and gold ions were implanted at high energies into the rib waveguide and the ions chosen for investigation were implanted at 3 doses, to investigate the effect of dose on responsivity.

The detectors were fabricated in the University of Southampton cleanroom. The first step was to etch the waveguides and grating couplers by 330 nm. Then to implant the N and P dopants the wafers were sent to Surrey Ion Beam Centre and implanted with phosphorus and BF2 to create a concentration of 1E19 and 2E19 ions/cm^3 near the boundary Ohmic contact and germanium. Next the Ohmic contacts were deposited in a layered stack of 30 nm of Ni, 10 nm of Ti, 200 nm of Al and 60 nm of Ti. Finally the wafer is diced into chips and sent to Surrey Ion Beam Centre again to be implanted with boron ions at fluences of 1x10^{10}, 1x10^{12} and 1x10^{14} ions/cm^2 and also to Zurich ETH to be implanted with Ge, Au, Hg and Cu at fluences of 1x10^{10}, 1E11 and 1x10^{12} ions/cm^2.

When characterising the effect of the detectors implanted with boron it was found that the detectors without added defects exhibited the largest response and a responsivity larger than intrinsic germanium. Further measurements where taken to discover the extent and repeatability of this finding. IV curves where the reverse bias of the detectors where swept from 0V to -10V found a responsivity of 1.08 A/W at 2 μm using a 1 0V reverse bias and 0.1 A/W at 3.8 μm using a 7 V reverse bias. These results are superior to other monolithic waveguide integrated defect mediated detectors and waveguide integrated Ge/Sn detectors in terms of responsivty and the spectral range. The waveguides created to guide 2 and 3.8 μm had losses of (12.4$\pm$3) dB/cm and (17$\pm$2.4) dB/cm respectively. The grating couplers designed for use at 2 μm has an insertion loss of 8.8 dB and 10.8 dB, and at 3.8 μm a loss of 9.4 dB.

The RF response was also measured to quantify it's suitability for telecommunications applications. The electro-optic bandwidth was measured and this suggested that the devices were responsive up to 25 GHz but the devices were not impedance matched. This resulted in parasitic reflections which obscured the true electro-optic bandwidth so the 3 dB bandwidth could not be obtained but did provide a proof of principle. To investigate the data rate possible the devices where provided with a signal modulated with a 12.5 Gbps pseudorandom bit sequence using 2 μm light and an open eyediagram was obtained.

Finally an investigation into the photoabsorption mechanism was performed to deduce the cause of absorption above the bandgap of instrinsic germanium. It ruled out two photon absorption as a linear relationship between the photocurrent and optical power of light was found. It ruled out that the defects were created during the addition of metal and doping regions as a negligible difference in loss of 0.1 dB and 0.7 dB after adding metal and doping respectively. The strain was also measured and resulted in a 0.22 % tensile strain by comparing this againgst biaxial strain versus bandgap energy graphs a bandgap shift of -0.037 eV is assumed. This shift would result in a 11 dB/cm loss at 2 in the devices and is comparible to the 12.4 dB/cm loss found at 2 μm in the waveguides measured in

this thesis, therefore strain may account for most of the absorption at 2 μm but can not at 3.8 μm.

8.2 Future Work

Currently these detectors are suitable as power monitors in photonic integrated circuits because of their high responsivity at 2 and 3.8 μm which outperforms other monolithic waveguide integrated photodetectors. To use these detectors for other applications, such as sensing and free-space telecommunications, the repeatability of fabrication, which would involve identifying how the photoactive defects are introduced, and how to integrate it into a complete circuit should be considered.

To identify which defects are responsible for absorption, deep level transient spectroscopy (DSTL) could be performed to learn more about whether defects are responsible for absorption at 3.8 μm and give information about the energy level of the defects present which would help deduce the defect source. Also by measuring the response of the devices above 2 μm the indirect band gap edge may be visible and used to confirm that strain is the main absorption mechanism at that wavelength range. If enough information about the absorption mechanism is learned, a simulation model of the devices could be created and used to optimise the device structure.

For sensing applications, PIC are already being made that could allow chemical sensing that are being made using silicon on insulator rib waveguides (102). Therefore, it would be useful to investigate the possibility of incorporating this projects germanium photodiodes into silicon circuitry which could be used in conjunction with silicon on insulator waveguides which are transparent up to 4 μm. A silicon circuit could be designed with windows for the growth of germanium. Proof of this functioning would be especially powerful, as the waveguides in this thesis have high loss due to absorption.

An important characteristic in sensing is the NEP, a characteristic which describes the signal power needed to provide a signal to noise ratio of 1 over a 1 Hz bandwidth. Therefore a device with a lower NEP is able to measure smaller changed in spectra. Therefore the NEP of these devices would need to be measured and optimised through design changes. To lower the NEP of the device, the dark current should be reduced and the responsivity increased. The dark current can be reduced by removing defects in the device that do not contribute to the photocurrent and are a source of trap assisted recombination. This can be done by investigating the effect of annealing on dark current and responsivity. To decrease the dark current, the length of the devices can be reduced. Although there is a trade off in this length, as a shorter device has less length for interaction between the light and defects but a shorter device would also reduce the dark current. An investigation could include fabricating devices with a range of lengths to find the optimal length. Also, the device should be improved to increase responsivity so a

shorter length of photodiode can be used. To improve the responsivity the mode overlap with defects should be maximised, the distance of the Ohmic contacts from the rib waveguide should be optimised and an avalanche mode design should be investigated. By investigating the responsivity of the other devices implanted with Ge, Au, Hg and Cu it may be found that another defect results in a larger responsivity because of more efficient absorption. Another parameter that should be investigated when designing these devices for sensing is the spectral range of the detector. Methane has spectral absorption features at 3.3 μm and at 4.2 μm there are carbon dioxide features. So at these wavelengths the responsivity and NEP should be measured. There are devices on the chip that can be cleaved to allow light to be butt coupled in at 4.2 μm and there are existing devices with grating couplers at 3.3 μm.

When considering the devices for telecommunications applications the bandwidth measurement should be repeated and optimised. During this project the electro-optic bandwidth was measured, however, due to parasitic reflections the 3 dB bandwidth could not be measured. To improve the measured bandwidth Ohmic contacts should be designed to 50 Ohms impedance so that it can be easily impedance matched with bandwidth read out circuits. The Ohmic contacts could also be designed to try lower resistance which would increase the bandwidth of the device. Another factor that impacts the bandwidth of the devices is the distance between the rib waveguide and doped region. There is a tradeoff between bandwidth speed and signal loss. A short distance would decrease the drift distance increasing speed but more light would overlap with the doped region causing free-carrier absorption.

These photodiodes prove promising as detector solutions to sensing and telecommunications and provide a high responsivity detector that could be monolithically integrated into PIC using a silicon substrate, where limited solutions exist, this can be seen in Table. 8.1. The fabrication of these devices require no extra steps to that of a non defect mediated germanium photodiode and to integrate onto silicon would only require the growth of germanium which keeps cost lower when fabricating the detectors on a mass scale. Where other detectors which aim to act as responsive MIR detectors like graphene and III-V semiconductors require extra fabrication steps like bump bonding in the case of III-V and manual exfoliation for graphene which is a slow, low yield method.

TABLE 8.1: Integrated MIR Sub-band Photodetectors

Type of Implant	Responsivity	Bias	Spectral Range	Band-width	Year	Ref
Si^+ in Si	up to 10 A/W	up to -20 V	1.1-1.75 μm	35 GHz	2009	(55)
B^+ in Si	0.3 A/W	-30 V	2 - 2.5 μm	15 GHz	2015	(49)
Si^+ in Si	9.9 mA/W	-5 V	2.2 - 2.35 μm	1.7 GHz	2014	(56)
Se^+ in Si	25 mA/W	-3 V	0.9 - 1.6 μm	N/A	2011	(57)
Au^- in Si	EQE 10^{-4}	-5 V	2.2 μm	N/A	2014	(58)
Zn^+ in Si	87 mA/W	-20 V	2.2 - 2.4 μm	N/A	2014	(52)
Au^- in Ge	0.25 mA/W	0 V	2 - 3 μm	N/A	2020	(53)
Defects in Ge	**1 A/W**	**-10 V**	**2 - 3.8 μm**	**12.5 Gb/s**	**2022**	**This Work**

References

[1] M. S. Yazici, B. Dong, D. Hasan, F. Sun, and C. Lee, "Integration of MEMS IR detectors with MIR waveguides for sensing applications," *Optics Express*, vol. 28, no. 8, pp. 11524–11537, 2020.

[2] J. J. Ackert, D. J. Thomson, L. Shen, A. C. Peacock, P. E. Jessop, G. T. Reed, G. Z. Mashanovich, and A. P. Knights, "High-speed detection at two micrometres with monolithic silicon photodiodes," *Nature Photonics*, vol. 9, no. 6, pp. 393–396, 2015.

[3] M. W. Geis, S. J. Spector, M. E. Grein, J. U. Yoon, D. M. Lennon, and T. M. Lyszczarz, "Silicon waveguide infrared photodiodes with >35 GHz bandwidth and phototransistors with 50 AW-1 response," *Optics Express*, vol. 17, no. 7, p. 5193, 2009.

[4] D. A. B. Miller, "Device requirements for optical interconnects to silicon chips," *Proceedings of the IEEE*, vol. 97, no. 7, pp. 1166–1185, 2009.

[5] V. Singh, P. T. Lin, N. Patel, H. Lin, L. Li, Y. Zou, F. Deng, C. Ni, J. Hu, J. Giammarco, A. P. Soliani, B. Zdyrko, I. Luzinov, S. Novak, J. Novak, P. Wachtel, S. Danto, J. D. Musgraves, K. Richardson, L. C. Kimerling, and A. M. Agarwal, "Mid-infrared materials and devices on a Si platform for optical sensing," *Science and technology of advanced materials*, vol. 15, p. 14603, Jan 2014.

[6] "Intel® Silicon Photonics: How does it work?." https://www.intel.co.uk/content/www/uk/en/architecture-and-technology/silicon-photonics/silicon-photonics-overview.html, accessed 8-03-2022.

[7] D. Popa and F. Udrea, "Towards integrated mid-infrared gas sensors," *Sensors*, vol. 19, no. 9, 2019.

[8] "Cisco Annual Internet Report - Cisco AIR Infographic (2018 - 2023)." https://www.cisco.com/c/en/us/solutions/executive-perspectives/annual-internet-report/infographic-c82-741491.html, accessed 8-03-2022.

[9] H. Manor and S. Arnon, "Performance of an optical wireless communication system as a function of wavelength," *Applied Optics*, vol. 42, no. 21, pp. 4285–4294, 2003.

[10] A. Daniels, "Spectral Atmospheric Transmittance," in *Field Guide to Infrared Optics, Materials, and Radiometry*, pp. 98–99, SPIE.

[11] L. Huang, B. Dong, X. Guo, Y. Chang, N. Chen, X. Huang, W. Liao, C. Zhu, H. Wang, C. Lee, and K.-W. Ang, "Waveguide-Integrated Black Phosphorus Photodetector for Mid-Infrared Applications," *ACS Nano*, vol. 13, pp. 913–921, Jan 2019.

[12] M. Muneeb, A. Vasiliev, A. Ruocco, A. Malik, H. Chen, M. Nedeljkovic, J. S. Penades, L. Cerutti, J. B. Rodriguez, G. Z. Mashanovich, M. K. Smit, E. Tourni, and G. Roelkens, "III-V-on-silicon integrated micro - spectrometer for the 3μm wavelength range," *Optics Express*, vol. 24, no. 9, pp. 9465–9472, 2016.

[13] A. Osman, M. Nedeljkovic, J. Soler Penades, Y. Wu, Z. Qu, A. Z. Khokhar, K. Debnath, and G. Z. Mashanovich, "Suspended low-loss germanium waveguides for the longwave infrared," *Optics Letters*, vol. 43, no. 24, pp. 5997–6000, 2018.

[14] G. Rieke, *Detection of Light: From the Ultraviolet to the Submillimeter*, pp. 18–19. Cambridge University Press, 2 ed., 2002.

[15] G. Rieke, *Detection of Light: From the Ultraviolet to the Submillimeter*, pp. 48–50. Cambridge University Press, 2 ed., 2002.

[16] A. Biswas, K.-S. Kim, and Y. H. Jeong, "Metal–insulator transitions and non-fermi liquid behaviors in 5d perovskite iridates," *Perovskite Materials - Synthesis, Characterisation, Properties, and Applications*, Feb 2016.

[17] "Hyperphysics Fermi Level." `http://hyperphysics.phy-astr.gsu.edu/hbase/Solids/Fermi.html`, accessed 8-03-2022.

[18] G. Rieke, *Detection of Light: From the Ultraviolet to the Submillimeter*, p. 21–24. Cambridge University Press, 2 ed., 2002.

[19] C. Littlejohns, *Silicon-Germanium for Photonic Applications*. PhD thesis, The University of Southampton, 2015.

[20] M. Casalino, G. Coppola, R. M. De La Rue, and D. F. Logan, "State-of-the-art all-silicon sub-bandgap photodetectors at telecom and datacom wavelengths," *Laser and Photonics Reviews*, vol. 10, no. 6, pp. 895–921, 2016.

[21] J. F. R. Archilla, S. M. M. Coelho, F. D. Auret, C. Nyamhere, V. I. Dubinko, and V. Hizhnyakov pp. 343–362, Springer International Publishing, 2015.

[22] G. Rieke, *Detection of Light: From the Ultraviolet to the Submillimeter*, pp. 43–47. Cambridge University Press, 2 ed., 2002.

[23] W. H. Press, "Flicker noises in astronomy and elsewhere.," *Comments on Astrophysics*, vol. 7, pp. 103–119, Jan. 1978.

[24] F. Hooge, "1/f noise sources," *IEEE Transactions on Electron Devices*, vol. 41, no. 11, pp. 1926–1935, 1994.

[25] A. S. Pratiyush, S. Krishnamoorthy, R. Muralidharan, S. Rajan, and D. N. Nath, "16 - Advances in Ga2O3 solar-blind UV photodetectors," in *Metal Oxides* (S. Pearton, F. Ren, and M. B. T. G. O. Mastro, eds.), pp. 369–399, Elsevier, 2019.

[26] "Spectral Response." https://www.pveducation.org/pvcdrom/solar-cell-operation/spectral-response, accessed 8-03-2022.

[27] Y. Dong, W. Wang, S. Xu, D. Lei, X. Gong, X. Guo, H. Wang, S.-Y. Lee, W.-K. Loke, S.-F. Yoon, and Y.-C. Yeo, "Two-micron-wavelength germanium-tin photodiodes with low dark current and gigahertz bandwidth," *Optics Express*, vol. 25, no. 14, p. 15818, 2017.

[28] G. Rieke, *Detection of Light: From the Ultraviolet to the Submillimeter*, pp. 41–43. Cambridge University Press, 2 ed., 2002.

[29] C. Littlejohns, *Silicon-Germanium for Photonic Applications*. PhD thesis, The University of Southampton, 2015.

[30] "Ti precision labs - signal conditioning: What is an eye diagram?." https://training.ti.com/what-is-an-eye-diagram, accessed 8-03-2022.

[31] "Eye diagram basics: Reading and applying eye diagrams." https://www.edn.com/eye-diagram-basics-reading-and-applying-eye-diagrams, accessed 19-09-2022.

[32] J. L. Tang Yi-RanAU - Zhang, Li-JiangAU - Fu, Xing-ChangAU - Xue, Xiao-MeiAU - Qian, GuangAU - Zhao, NingAU - Zhang, TongTI - Flexible Thermo-Optic Variable Attenuator based on Long-Range Surface Plasmon-Polariton Waveguides, "Flexible Thermo-Optic Variable Attenuator based on Long-Range Surface Plasmon-Polariton Waveguides," 2018.

[33] *Optical Lithography*, ch. 9, pp. 103–113. John Wiley Sons, Ltd, 2010.

[34] *Thin-Film Materials and Processes*, ch. 5, pp. 47–67. John Wiley Sons, Ltd, 2010.

[35] A. Bashir, T. Iqbal, A. Tehseen, M. Tahir, and M. Ijaz, *Surfaces and Interfaces*. Jan 2020.

[36] "JETFIRST BENCH-TOP RTP FURNACE." https://ecmlabsolutions.com/products/rtp-furnace-jetfirst/, accessed 19-09-2022.

[37] *Ion Implantation*, ch. 15, pp. 173–180. John Wiley Sons, Ltd, 2010.

[38] "Intel® Silicon Photonics: How does it work?." https://www.mksinst.com/n/ion-implantation, accessed 27-03-2022.

[39] X. Wang, A. C. Covian, L. Je, S. Fu, H. Li, J. Piao, and J. Liu, "GeSn on insulators (GeSnOI) toward mid-infrared integrated photonics," *Frontiers in Physics*, vol. 7, no. SEP, 2019.

[40] W. Dou, M. Benamara, A. Mosleh, J. Margetis, P. Grant, Y. Zhou, S. Al-Kabi, W. Du, J. Tolle, B. Li, M. Mortazavi, and S.-Q. Yu, "Investigation of GeSn Strain Relaxation and Spontaneous Composition Gradient for Low-Defect and High-Sn Alloy Growth," *Scientific Reports*, vol. 8, no. 1, p. 5640, 2018.

[41] J. Margetis, S. Al-Kabi, W. Du, W. Dou, Y. Zhou, T. Pham, P. Grant, S. Ghetmiri, A. Mosleh, B. Li, J. Liu, G. Sun, R. Soref, J. Tolle, M. Mortazavi, and S.-Q. Yu, "Si-Based GeSn Lasers with Wavelength Coverage of 2–3 μm and Operating Temperatures up to 180 K," *ACS Photonics*, vol. 5, pp. 827–833, Mar 2018.

[42] S. Xu, W. Wang, Y.-C. Huang, Y. Dong, S. Masudy-Panah, H. Wang, X. Gong, and Y.-C. Yeo, "High-speed photo detection at two-micron-wavelength: technology enablement by GeSn/Ge multiple-quantum-well photodiode on 300 mm Si substrate," *Optics Express*, vol. 27, no. 4, pp. 5798–5813, 2019.

[43] A. Gassenq, F. Gencarelli, J. Van Campenhout, Y. Shimura, R. Loo, G. Narcy, B. Vincent, and G. Roelkens, "GeSn/Ge heterostructure short-wave infrared photodetectors on silicon," *Optics Express*, vol. 20, no. 25, p. 27297, 2012.

[44] T. N. Pham, W. Du, B. R. Conley, J. Margetis, G. Sun, R. A. Soref, J. Tolle, B. Li, and S.-Q. Yu, "Si-based Ge0.9Sn0.1 photodetector with peak responsivity of 2.85 A/W and longwave cutoff at 2.4 μm," *Electronics Letters*, vol. 51, pp. 854–856, May 2015.

[45] Y. Dong, W. Wang, S. Y. Lee, D. Lei, X. Gong, W. K. Loke, S. Yoon, G. Liang, and Y. Yeo, "Avalanche photodiode featuring Germanium-tin multiple quantum wells on silicon: Extending photodetection to wavelengths of 2 and beyond," in *2015 IEEE International Electron Devices Meeting (IEDM)*, pp. 30.5.1–30.5.4, 2015.

[46] Y. Dong, W. Wang, S. Xu, D. Lei, X. Gong, X. Guo, H. Wang, S.-Y. Lee, W.-K. Loke, S.-F. Yoon, and Y.-C. Yeo, "Two-micron-wavelength germanium-tin photodiodes with low dark current and gigahertz bandwidth," *Optics Express*, vol. 25, no. 14, pp. 15818–15827, 2017.

[47] H. Tran, C. G. Littlejohns, D. J. Thomson, T. Pham, A. Ghetmiri, A. Mosleh, J. Margetis, J. Tolle, G. Z. Mashanovich, W. Du, B. Li, M. Mortazavi, and S. Q. Yu, "Study of GeSn Mid-infrared Photodetectors for High Frequency Applications," *Frontiers in Materials*, vol. 6, no. November, pp. 1–7, 2019.

[48] M. W. Geis, S. J. Spector, M. E. Grein, J. U. Yoon, D. M. Lennon, and T. M. Lyszczarz, "Silicon waveguide infrared photodiodes with >35 GHz bandwidth and phototransistors with 50 AW-1 response," *Optics Express*, vol. 17, no. 7, pp. 5193–5204, 2009.

[49] "High-speed detection at two micrometres with monolithic silicon photodiodes," *Nature Photonics*, vol. 9, no. 6, pp. 393–396, 2015.

[50] Y. Berencén, S. Prucnal, F. Liu, I. Skorupa, R. Hübner, L. Rebohle, S. Zhou, H. Schneider, M. Helm, and W. Skorupa, "Room-temperature short-wavelength infrared Si photodetector," *Scientific Reports*, vol. 7, no. March, p. 43688, 2017.

[51] Y. Berencén, S. Prucnal, F. Liu, I. Skorupa, R. Hübner, L. Rebohle, S. Zhou, H. Schneider, M. Helm, and W. Skorupa, "Room-temperature short-wavelength infrared Si photodetector," *Scientific Reports*, vol. 7, p. 43688, Mar 2017.

[52] R. R. Grote, B. Souhan, N. Ophir, J. B. Driscoll, K. Bergman, H. Bahkru, W. M. J. Green, and R. M. Osgood, "Extrinsic photodiodes for integrated mid-infrared silicon photonics," *Optica*, vol. 1, pp. 264–267, Oct 2014.

[53] H. H. Gandhi, D. Pastor, T. T. Tran, S. Kalchmair, L. A. Smilie, J. P. Mailoa, R. Milazzo, E. Napolitani, M. Loncar, J. S. Williams, M. J. Aziz, and E. Mazur, "Gold-Hyperdoped Germanium with Room-Temperature Sub-Band-Gap Optoelectronic Response," *Physical Review Applied*, vol. 14, no. 6, p. 1, 2020.

[54] Z. Zhao, C. Ho, Q. Li, K. Toprasertpong, S. Takagi, and M. Takenaka, "Monolithic Germanium PIN Waveguide Photodetector Operating at 2 μm Wavelengths," p. W4G.3, 2020.

[55] M. W. Geis, S. J. Spector, M. E. Grein, J. U. Yoon, D. M. Lennon, and T. M. Lyszczarz, "Silicon waveguide infrared photodiodes with 35 ghz bandwidth and phototransistors with 50 aw-1 response," *Opt. Express*, vol. 17, pp. 5193–5204, Mar 2009.

[56] B. Souhan, R. R. Grote, C. P. Chen, H.-C. Huang, J. B. Driscoll, M. Lu, A. Stein, H. Bakhru, K. Bergman, W. M. J. Green, and R. M. Osgood, "Si + implanted si-wire waveguide photodetectors for the mid-infrared," *Opt. Express*, vol. 22, pp. 27415–27424, Nov 2014.

[57] X. Mao, P. Han, L. Gao, Y. Mi, S. Hu, Y. Fan, C. Zhao, and Q. Wang, "Selenium-doped silicon-on-insulator waveguide photodetector with enhanced sensitivity at 1550 nm," *IEEE Photonics Technology Letters*, vol. 23, no. 20, pp. 1517–1519, 2011.

[58] J. P. Mailoa, A. J. Akey, C. B. Simmons, D. Hutchinson, J. Mathews, J. T. Sullivan, D. Recht, M. T. Winkler, J. S. Williams, J. M. Warrender, P. D. Persans, M. J. Aziz, and T. Buonassisi, "Room-temperature sub-band gap optoelectronic response of hyperdoped silicon," *Nature Communications*, vol. 5, pp. 1–8, 2014.

[59] D. F. Logan, P. E. Jessop, and A. P. Knights, "Modeling defect enhanced detection at 1550 nm in integrated silicon waveguide photodetectors," *Journal of Lightwave Technology*, vol. 27, no. 7, pp. 930–937, 2009.

[60] H. Y. Fan and A. K. Ramdas, "Infrared absorption and photoconductivity in irradiated silicon," *Journal of Applied Physics*, vol. 30, no. 8, pp. 1127–1134, 1959.

[61] P. G. Kik, A. Polman, S. Libertino, and S. Coffa, "Design and Performance of an Erbium-Doped Silicon Waveguide Detector Operating at 1.5 um," *Journal of Lightwave Technology*, vol. 20, no. 5, p. 834, 2002.

[62] N. Hamelin, P. G. Kik, J. F. Suyver, K. Kikoin, A. Polman, A. Schönecker, and F. W. Saris, "Energy backtransfer and infrared photoresponse in erbium-doped silicon p–n diodes," *Journal of Applied Physics*, vol. 88, pp. 5381–5387, Oct 2000.

[63] A. Knights, A. House, R. MacNaughton, and F. Hopper, "Optical Power Monitoring Function Compatible with Single Chip Integration on Silicon-on-Insulator," in *Optical Fiber Communication Conference*, Technical Digest, (Atlanta, Georgia), p. FJ3, Optical Society of America, 2003.

[64] J. D. B. Bradley, P. E. Jessop, and A. P. Knights, "Silicon waveguide-integrated optical power monitor with enhanced sensitivity at 1550nm," *Applied Physics Letters*, vol. 86, p. 241103, Jun 2005.

[65] A. P. Knights, J. D. B. Bradley, S. H. Gou, and P. E. Jessop, "Silicon-on-insulator waveguide photodetector with self-ion-implantation-engineered-enhanced infrared response," *Journal of Vacuum Science & Technology A*, vol. 24, no. 3, pp. 783–786, 2006.

[66] B. Souhan, C. P. Chen, R. R. Grote, J. B. Driscoll, N. Ophir, K. Bergman, and R. M. Osgood, "Error-Free Operation of an All-Silicon Waveguide Photodiode at 1.9 μm," *IEEE Photonics Technology Letters*, vol. 25, no. 21, pp. 2031–2034, 2013.

[67] D. J. Thomson, L. Shen, J. J. Ackert, E. Huante-Ceron, A. P. Knights, M. Nedeljkovic, A. C. Peacock, and G. Z. Mashanovich, "Optical detection and modulation at 2µm-25µm in silicon," *Optics Express*, vol. 22, no. 9, p. 10825, 2014.

[68] A. Ren, L. Yuan, H. Xu, J. Wu, and Z. Wang, "Recent progress of III–V quantum dot infrared photodetectors on silicon," *Journal of Materials Chemistry C*, vol. 7, no. 46, pp. 14441–14453, 2019.

[69] S. Keyvaninia, M. Muneeb, S. Stanković, P. J. Van Veldhoven, D. Van Thourhout, and G. Roelkens, "Ultra-thin DVS-BCB adhesive bonding of III-V wafers, dies and multiple dies to a patterned silicon-on-insulator substrate," *Optical Materials Express*, vol. 3, no. 1, pp. 35–46, 2013.

[70] J. Hillbrand, L. Matthieu Krüger, S. Dal Cin, H. Knötig, J. Heidrich, A. Maxwell Andrews, G. Strasser, U. Keller, and B. Schwarz, "High-speed quantum cascade detector characterized with a mid-infrared femtosecond oscillator," *Optics Express*, vol. 29, no. 4, pp. 5774–5781, 2021.

[71] R. Wang, M. Muneeb, S. Sprengel, G. Boehm, A. Malik, R. Baets, M.-C. Amann, and G. Roelkens, "III-V-on-silicon 2-3.8μm-wavelength-range wavelength demultiplexers with heterogeneously integrated InP-based type-II photodetectors," *Optics Express*, vol. 24, no. 8, pp. 8480–8490, 2016.

[72] A. Gassenq, N. Hattasan, L. Cerutti, J. B. Rodriguez, E. Tournié, and G. Roelkens, "Study of evanescently-coupled and grating-assisted GaInAsSb photodiodes integrated on a silicon photonic chip," *Optics Express*, vol. 20, no. 11, pp. 11665–11672, 2012.

[73] J. Michel, J. Liu, and L. C. Kimerling, "High-performance Ge-on-Si photodetectors," *Nature Photonics*, vol. 4, p. 527, Jul 2010.

[74] J. Wang and S. Lee, "Ge-photodetectors for Si-based optoelectronic integration," *Sensors (Basel, Switzerland)*, vol. 11, no. 1, pp. 696–718, 2011.

[75] D. Marris-Morini, V. Vakarin, J. M. Ramirez, Q. Liu, A. Ballabio, J. Frigerio, M. Montesinos, C. Alonso-Ramos, X. Le Roux, S. Serna, D. Benedikovic, D. Chrastina, L. Vivien, and G. Isella, "Germanium-based integrated photonics from near- to mid-infrared applications," *Nanophotonics*, vol. 7, no. 11, pp. 1781–1793, 2018.

[76] L. Vivien, J. Osmond, J.-M. Fédéli, D. Marris-Morini, P. Crozat, J.-F. Damlencourt, E. Cassan, Y. Lecunff, and S. Laval, "42 GHz p.i.n Germanium photodetector integrated in a silicon-on-insulator waveguide," *Optics Express*, vol. 17, no. 8, pp. 6252–6257, 2009.

[77] H. Li, S. Zhang, Z. Zhang, S. Zuo, S. Zhang, Y. Sun, D. Zhao, and Z. Zhang, "Silicon Waveguide Integrated with Germanium Photodetector for a Photonic-Integrated FBG Interrogator," 2020.

[78] Z. Han, V. Singh, D. Kita, C. Monmeyran, P. Becla, P. Su, J. Li, X. Huang, L. C. Kimerling, J. Hu, K. Richardson, D. T. H. Tan, and A. Agarwal, "On-chip chalcogenide glass waveguide-integrated mid-infrared PbTe detectors," *Applied Physics Letters*, vol. 109, p. 71111, Aug 2016.

[79] P. Su, Z. Han, D. Kita, P. Becla, H. Lin, S. Deckoff-Jones, K. Richardson, L. C. Kimerling, J. Hu, and A. Agarwal, "Monolithic on-chip mid-IR methane gas sensor with waveguide-integrated detector," *Applied Physics Letters*, vol. 114, p. 51103, Feb 2019.

[80] Y. Wu, Z. Qu, A. Osman, W. Cao, A. Z. Khokhar, J. Soler Penades, O. L. Muskens, G. Z. Mashanovich, and M. Nedeljkovic, "Mid-Infrared Nanometallic Antenna Assisted Silicon Waveguide Based Bolometers," *ACS Photonics*, vol. 6, pp. 3253–3260, Dec 2019.

[81] M. Buscema, D. J. Groenendijk, S. I. Blanter, G. A. Steele, H. S. J. van der Zant, and A. Castellanos-Gomez, "Fast and Broadband Photoresponse of Few-Layer Black Phosphorus Field-Effect Transistors," *Nano Letters*, vol. 14, pp. 3347–3352, Jun 2014.

[82] Z. Qu, *SOI Waveguide Integrated Graphene Mid-Infrared Detector*. PhD thesis, 2019.

[83] H. Li, Y. Anugrah, S. J. Koester, and M. Li, "Optical absorption in graphene integrated on silicon waveguides," *Applied Physics Letters*, vol. 101, p. 111110, Sep 2012.

[84] X. Wang, Z. Cheng, K. Xu, H. K. Tsang, and J.-B. Xu, "High-responsivity graphene/silicon-heterostructure waveguide photodetectors," *Nature Photonics*, vol. 7, no. 11, pp. 888–891, 2013.

[85] Z. Qu, M. Nedeljkovic, Y. Wu, J. S. Penades, A. Z. Khokhar, W. Cao, A. M. Osman, Y. Qi, N. K. Aspiotis, K. A. Morgan, C. C. Huang, and G. Z. Mashanovich, "Waveguide integrated graphene mid-infrared photodetector," in *Proc.SPIE*, vol. 10537, Feb 2018.

[86] Y. Ma, B. Dong, J. Wei, Y. Chang, W. Liu, and C. Lee, "Slow-light-enhanced waveguide-integrated black phosphorus mid-infrared photodetector," in *2020 IEEE 33rd International Conference on Micro Electro Mechanical Systems (MEMS)*, pp. 153–156, 2020.

[87] J. M. Ramirez, H. Elfaiki, T. Verolet, C. Besancon, A. Gallet, D. Néel, K. Hassan, S. Olivier, C. Jany, S. Malhouitre, K. Gradkowski, P. E. Morrissey, P. O'Brien, C. Caillaud, N. Vaissière, J. Decobert, S. Lei, R. Enright, A. Shen, and M. Achouche, "III-V-on-Silicon Integration: From Hybrid Devices to Heterogeneous Photonic Integrated Circuits," *IEEE Journal of Selected Topics in Quantum Electronics*, vol. 26, no. 2, pp. 1–13, 2020.

[88] "Lumerical FDTD." https://www.lumerical.com/products/fdtd/, accessed 8-03-2022.

[89] "James Ziegler - SRIM & TRIM." http://www.srim.org/, accessed 8-03-2022.

[90] "Silvaco." https://silvaco.com/, accessed 8-03-2022.

[91] B. Souhan, R. R. Grote, C. P. Chen, H.-C. Huang, J. B. Driscoll, M. Lu, A. Stein, H. Bakhru, K. Bergman, W. M. J. Green, and R. M. Osgood, "Si+-implanted Si-wire waveguide photodetectors for the mid-infrared," *Optics Express*, vol. 22, no. 22, p. 27415, 2014.

[92] R. R. Grote, K. Padmaraju, B. Souhan, J. B. Driscoll, K. Bergman, and R. M. Osgood, "10 Gb/s error-free operation of all-silicon ion-implanted-waveguide photodiodes at 1.55 μm," *IEEE Photonics Technology Letters*, vol. 25, no. 1, pp. 67–70, 2013.

[93] L. Mastronardi, *GeSi Franz-Keldysh modulator for silicon photonic integrated circuits*. PhD thesis, University of Southampton, October 2019.

[94] "L-EDIT IC: EDA Solutions." https://www.eda-solutions.com/products/tanner-l-edit-ic-layout/, accessed 8-03-2022.

[95] http://www.simgui.com.cn/en/, accessed 27-03-2022.

[96] X. Chen and H. K. Tsang, "Polarization-independent grating couplers for silicon-on-insulator nanophotonic waveguides," *Optics Letters*, vol. 36, no. 6, pp. 796–798, 2011.

[97] Z. Zhao, C. Ho, Q. Li, K. Toprasertpong, S. Takagi, and M. Takenaka, "Monolithic germanium pin waveguide photodetector operating at 2 μm wavelengths," in *Optical Fiber Communication Conference (OFC) 2020*, p. W4G.3, Optical Society of America, 2020.

[98] W. C. Dash and R. Newman, "Intrinsic optical absorption in single-crystal germanium and silicon at 77°k and 300°k," *Phys. Rev.*, vol. 99, pp. 1151–1155, Aug 1955.

[99] R. Anthony, D. E. Hagan, D. Genuth-Okon, L. Martinez Maestro, I. F. Crowe, M. P. Halsall, and A. P. Knights, "Extended wavelength responsivity of a germanium photodetector integrated with a silicon waveguide exploiting the indirect transition," *IEEE Journal of Selected Topics in Quantum Electronics*, vol. 26, no. 2, pp. 1–7, 2020.

[100] Y. Ishikawa, K. Wada, D. D. Cannon, J. Liu, H.-C. Luan, and L. C. Kimerling, "Strain-induced band gap shrinkage in ge grown on si substrate," *Applied Physics Letters*, vol. 82, no. 13, pp. 2044–2046, 2003.

[101] M. Nedeljkovic, J. S. Penadés, C. J. Mitchell, A. Z. Khokhar, S. Stanković, T. D. Bucio, C. G. Littlejohns, F. Y. Gardes, and G. Z. Mashanovich, "Surface-grating-coupled low-loss ge-on-si rib waveguides and multimode interferometers," *IEEE Photonics Technology Letters*, vol. 27, no. 10, pp. 1040–1043, 2015.

[102] Y. Qi, Z. Zheng, M. Banakar, Y. Wu, A. Gangnaik, D. J. Rowe, V. Mittal, J. Butement, J. S. Wilkinson, G. Z. Mashanovich, and M. Nedeljkovic, "Integrated switching circuit for low-noise self-referenced mid-infrared absorption sensing using silicon waveguides," *IEEE Photonics Journal*, vol. 13, no. 6, pp. 1–10, 2021.